Chair of Astronautics
Prof. Prof. h.c. Dr. Dr. h.c.
Ulrich Walter

Master's Thesis

Analysis of an In-Situ Material Production Concept for Potential Thermal Applications in a Lunar Mission

RT-MA 2020-22

Author:
Francisco Javier Guerrero González

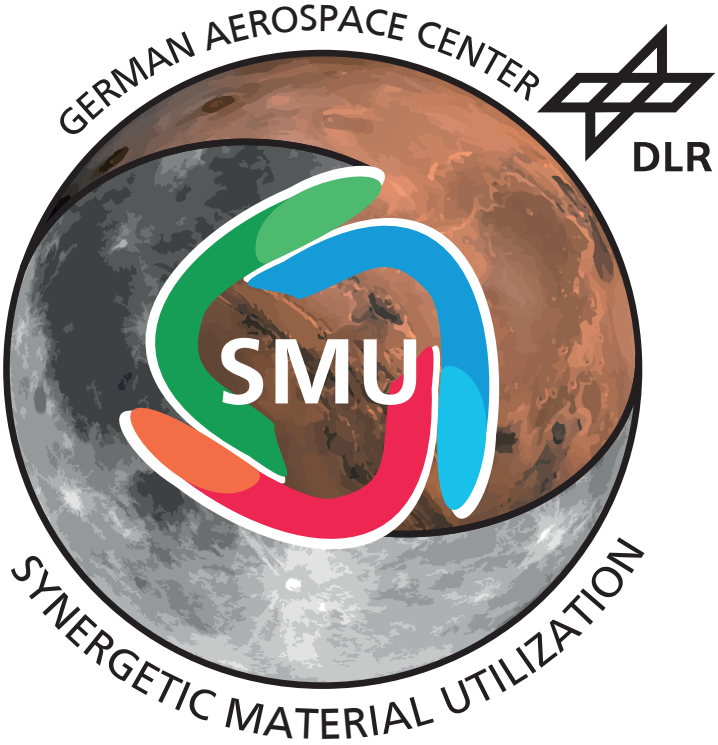

Supervisors: M.Sc. Daniel Kaschubek[1]
M.Sc. Laura Grill[1]
Dr.-Ing. Paul Zabel[2]

[1]Chair of Astronautics, Technical University of Munich
[2]Institute of Space Systems, German Aerospace Center

Acknowledgements

First and foremost, I would like to thank the Technical University of Munich and, in particular, the Chair of Astronautics for helping me to find in space exploration a passion that I thought was unattainable. Their high-performance environment and quality lectures have allowed me to enter the field of in-situ resource utilization, in which I have ended up writing this Master's thesis.

As this thesis comes to an end, I would also like to acknowledge those people who accompanied me throughout its development. I am truly grateful to Paul Zabel for opening the doors of his newly founded research group on Synergetic Material Utilization. From the very first phone call, he was keen on finding a research topic that we were both passionate about. My stay at the German Aerospace Center in Bremen has been an incredible and enriching experience.

I would also like to thank my supervisors at the Chair of Astronautics, Daniel Kaschubek and Laura Grill, for their profound insight into the fields of space exploration and in-situ resource utilization. Their advice and recommendations have been an invaluable asset guiding me in the right direction.

I am grateful to the entire Synergetic Material Utilization group for engaging in absorbing and enlightening discussions on beneficiation, water processing, or metal refining. These discussions were instrumental in filling the gaps in my knowledge and allowed me to develop my work in the best possible way.

And finally, to my parents and friends, for their unconditional support during these last two years at the Technical University of Munich.

Zusammenfassung

Die Verwendung von lokalen Ressourcen, auch In-Situ Ressourcennutzung (ISRU) genannt, wird seit langem als möglicher Weg zur Verringerung der Kosten von Missionen zum Mond und Mars vorgeschlagen. Die Gewinnung von Sauerstoff aus Mondregolith hat sich als das vielversprechendste ISRU-Verfahren erwiesen. Sauerstoff könnte für Lebenserhaltung und Treibstoffproduktion verwendet werden. Sauerstoff ist jedoch nicht die einzige Ressource, die aus dem Mondboden extrahiert werden kann. Mondregolith enthält auch Metalle und Halbmetalle, die für den Aufbau einer Weltrauminfrastruktur und einer nachhaltigen menschlichen Präsenz auf dem Mond verwendet werden könnten. Bevor ISRU-Prozesse als machbare Alternative zum Transport aller materiellen Ressourcen von der Erde in Betracht gezogen werden, müssen die Masse und die Leistung der benötigten Systeme gründlich untersucht werden.

Zu diesem Zweck wird eine Referenzmission auf der Mondoberfläche am Südpol als Fallstudie definiert. Die Mondbasis besteht aus einem Umweltkontroll- und Lebenserhaltungssystem (ECLSS) für sechs Besatzungsmitglieder und einer ISRU-Anlage. Die ISRU-Anlage muss 15 t/Jahr O_2 und genügend metallische Nebenprodukte produzieren, um einen Radiator herzustellen. Der herzustellende Radiator soll die von der Mondbasis erzeugte Wärmeleistung ableiten können.

Es werden analytische Berechnungsmodelle für die gesamte ISRU-Prozesskette entwickelt, einschließlich der einzelnen Produktionsstufen: Abbau, Aufbereitung, Sauerstoffextraktion, Metallverarbeitung und Produktherstellung. Der Schwerpunkt liegt auf der Sauerstoffextraktion und der Metallverarbeitung. Bei der Sauerstoffextraktion werden Wasserstoffreduktion, Schmelzregolith-Elektrolyse (MRE) und Salzschmelzelektrolyse (MSE) betrachtet. Bei der Metallverarbeitungs werden Carbonylierung, Schmelzraffination und Vakuumdestillation analysiert. Die Modelle geben den Masse-, Volumen-, Energie- und Kühlungsbedarf auf der Grundlage vorangegangener Arbeiten, analytischer Berechnungen, extrapolierter Daten aus der experimentellen Forschung und Analogien zwischen Erd- und Weltraumkomponenten an.

Neben Sauerstoff werden fünf raffinierte metallische Nebenprodukte hinsichtlich ihrer mechanischen und thermischen Eigenschaften charakterisiert: Carbonyl- und schmelzraffiniertes Eisen, Ferrosiliziumlegierungen, Hochlandmetallmischungen und destilliertes Aluminium. Thermo-fluiddynamische Simulationen liefern die Masse pro abgeleiteter Wärmeeinheit für verschiedene Radiatormaterialien, Designs und Positionen.

Eine multikriterielle Analyse (MCA) wird durchgeführt, um acht ISRU-Konzepte zu bewerten. Die MCA beinhaltet eine äquivalente Systemmassenanalyse (ESM) und eine qualitativ Bewertung der Vielseitigkeit der ISRU-Prozesskette. Die Vielseitigkeitskriterien bewerten die Vor- und Nachteile der ISRU-Konzepte, die in einer ESM-Analyse nicht quantitativ erfasst werden können.

Das beste Konzept besteht aus einem MRE-Reaktor, der 15 Tonnen Sauerstoff und 6,7 Tonnen Ferrosiliziumlegierungen pro Jahr produziert. 800 t/a Hochlandregolith werden abgebaut und aufbereitet, um eine Konzentration von 20 Gew.% an FeO-reichen Mineralien zu erreichen. Die Fe-Si-Legierungen werden stranggepresst, um Drahtvormaterial zu produzieren. Mit drahtbasierten additiven Fertigungsverfahren wird ein Radiator hergestellt, der 34,2 kW Wärmeleistung abgibt. Die gesamte ISRU-Prozesskette wiegt 1100 kg bei 2,8 m^3 und verbraucht 61 kW elektrische Leistung und gibt 1,4 kW Wärmeleistung ab. Die MRE-Elektroden (237 kg/a) müssen regelmäßig von der Erde gebracht werden.

Abstract

In-Situ Resource Utilization (ISRU) has long been suggested as a possible path to reduce the cost of missions to the Moon and Mars. Extracting oxygen from lunar regolith has been established as the most promising ISRU process. Oxygen could be used for life support and in-situ propellant production. However, oxygen is not the only resource that can be extracted from lunar soils. Lunar regolith also contains abundant metals and metalloids that could be processed to build space infrastructure and enable a sustainable human presence on the Moon. Before ISRU processes are considered as a feasible alternative to transporting all material resources from Earth, the mass and performance of the required systems must be rigorously investigated.

To this end, a lunar surface reference mission is defined at the South Pole as a case study. The Moonbase is composed of an Environmental Control and Life Support Systems (ECLSS) for six crew members and an ISRU facility. The ISRU facility must produce 15 t/y of O_2 and enough metallic byproducts to manufacture a radiator that rejects the heat generated by the Moonbase.

Analytical sizing models are developed for the entire ISRU process chain, including the individual production stages: excavation, beneficiation, oxygen extraction, metal processing, and manufacturing. Focus is given to the oxygen extraction and metal processing. The oxygen extraction stage analyzes hydrogen reduction, molten regolith electrolysis (MRE), and molten salt electrolysis (MSE). The metal processing stage investigates carbonylation, melt-refining, and vacuum distillation. The models return their mass, volume, power, and cooling requirements based on previously published works, analytical calculations, data extrapolated from experimental research, and analogies drawn between terrestrial and space components.

Besides oxygen, five refined metallic byproducts are characterized in terms of their mechanical and thermal properties: carbonyl and melt-refined irons, ferrosilicon alloys, highlands metallic mixtures, and distilled aluminum. Thermo-fluid dynamic simulations return the mass per unit of heat rejected for different radiator materials, designs, and positions.

A multi-criteria analysis (MCA) evaluates eight production concepts. The MCA comprises an Equivalent System Mass (ESM) analysis and a qualitative evaluation of the ISRU process chain versatility. The versatility criteria evaluate the advantages and disadvantages of the production concepts that cannot be quantitatively included in an ESM analysis.

The most suitable concept consists of an MRE reactor that produces 15 tons of oxygen and 6.7 tons of ferrosilicon alloys per year. 800 t/y of highlands regolith are excavated and beneficiated to reach a concentration of 20 wt.% of FeO-rich minerals. Fe-Si alloys are extruded to produce wire feedstock. Wire-based additive manufacturing techniques manufacture a radiator that rejects 34.2 kW of heat. The entire ISRU process chain requires 1100 kg and 2.8 m^3, consuming 61 kW of electric power and rejecting 1.4 kW of heat. The MRE electrodes (237 kg/y) must be regularly brought from Earth.

Contents

List of Figures

List of Tables

Symbols and Formulas

Roman Symbols

Symbol	Unit	Description
A	m^2	area
C_p	J/(kg·K)	specific heat at constant pressure
D	m	diameter
d	m	thickness
F	(A·s)/mol	Faraday constant
f	-	safety factor
H	m	height
h	W/(m^2·K)	convective heat transfer coefficient
I	A	current
k	W/(m·K)	thermal conductivity
L	m	length
L_{vap}	J/kg	enthalpy of vaporization
M	kg	mass
M_W	g/mol	molecular weight
$\dot{m}$	kg/s	mass flow
N	kg/y	O_2 production rate
Nu	-	Nusselt number
n_{batch}	1/y	number of batches in a year
P	W	power
p	Pa	pressure
p_i	Pa	partial pressure of species i
$\dot{Q}$	W	heat flow rate
R	m/s	cyclone project constant
$\bar{R}$	J/(kg·K)	specific gas constant
S	MPa	allowable stress
T	K	temperature
t	s	time
U	V	voltage
V	m^3	volume
$\dot{V}$	m^3/s	volumetric flow
w	kg/kg	weight fraction

Greek Symbols

Symbol	Unit	Description
α	-	absorptance
ΔG	J/mol	Gibbs free energy
ΔH_f	J/mol	enthalpy of formation
ϵ	-	emittance
ϵ_{eff}	-	effective emittance
η	-	efficiency
Γ	-	score
γ	-	weight factor
γ_V	kg/m^3	volume ESM factor
γ_P	kg/kW	power ESM factor
γ_Q	kg/kW	cooling ESM factor
λ_{CaCl_2}	kg/kg	electrolyte ratio
λ_{O_2}	kg/kg	oxygen yield
μ_{mol}	mol/mol	mole ratio
ρ	kg/m^3	density
σ	kg/(s^3·K^4)	Stefan-Boltzmann constant
τ	-	duty cycle

Acronyms

3D Three-dimensional

AM Additive Manufacturing

ASME American Society of Mechanical Engineers

ATC Active Thermal Control

BPA Brine Processor Assembly

CAD Computer-Aided Design

CCAA Common Cabin Air Assembly

CDRA Carbon Dioxide Removal Assembly

CFD Computational Fluid Dynamics

CHX Condensing Heat Exchanger

CM Crew Member

CNC Computer Numerical Control

CSOEC CO_2 Solid Oxide Electrolysis Cell

CVD Chemical Vapor Deposition

DED Direct Energy Deposition

DLR Deutsches zentrum für Luft- und Raumfahrt

DLRE Diviner Lunar Radiometer Experiment

EBAM Electron Beam Additive Manufacturing

ECLSS Environmental Control and Life Support System

ESA European Space Agency

ESM Equivalent System Mass

EVA Extravehicular Activity

FDM Fused Deposition Modeling

FFC Fray-Farthing-Chen

GDR Gridded Data Record

GEO Geosynchronous Equatorial Orbit

HEPA High-Efficiency Particulate Air

HX Heat Exchanger

IITRI Illinois Institute of Technology Research Institute

IMR Induced Magnetic Roll

ISECG International Space Exploration Coordination Group

ISRU In-Situ Resource Utilization

ISS International Space Station

LEO Low Earth Orbit

LiSTOT Life Support Trade-Off Tool

LLO Low Lunar Orbit

LOLA Lunar Orbiter Laser Altimeter

LRO Lunar Reconnaissance Orbiter

LRT Lehrstuhl für Raumfahrttechnik

MCA Multi-Criteria Analysis

MIT Massachusetts Institute of Technology

MIVM Molecular Interaction Volume Model

MLI Multi-Layer Insulation

MRE Molten Regolith Electrolysis

MSE Molten Salt Electrolysis

NASA National Aeronautics and Space Administration

POL Peak Of Light

PROSPECT Package for Resource Observation and in-Situ Prospecting for Exploration, Commercial exploitation and Transportation

PSR Permanently Shaded Region

PTC Passive Thermal Control

R&D Research and Development

RASSOR Regolith Advanced Surface Systems Operations Robot

RFCS Regenerative Fuel Cell System

SCRA Sabatier CO_2 Reprocessing Assembly

SFWE Static Feed Water Electrolyzer

SLM Selective Laser Melting

SLS Selective Laser Sintering

SMU Synergetic Material Utilization

TCS Thermal Control System

TRL Technology Readiness Level

TUM Technische Universität München

UPA Urine Processor Assembly

US United States

V-HAB Virtual Habitat

WPA Water Processor Assembly

YSZ Yttria-Stabilized Zirconia

1 Introduction

Since the end of the Apollo program in 1972, mankind has been dreaming of setting foot on the Moon again. The progress in space science and technology made during the last decade might make this dream come true in the near future. The US Artemis program launched in 2017 initially aimed to return humans to the Moon by 2024 [1]. Moreover, multiple international space agencies have developed their own Moonbase concepts, e.g., ESA's Moon Village [2, 3], to allow a continuous and sustainable human presence on the lunar surface.

However, one of the most significant barriers to a continuous and sustainable human presence on the lunar surface is the cost of transporting all the necessary material resources from Earth [4]. Due to Earth's gravity well, a small increase in payload mass results in a dramatic increase in the total launch mass. Launch masses and, therefore, costs have limited space exploration since its conception. The dependency on terrestrial resources must be minimized to enable an affordable exploration of the Moon.

In-Situ Resource Utilization (ISRU) is "the collection, processing, storing and use of materials encountered in the course of human or robotic space exploration that replace materials that would otherwise be brought from Earth" [5]. The most studied ISRU processing technique is the extraction of oxygen from lunar soils [6]. Oxygen could be used for life support and in-situ propellant production, since it is a major mass component of many bipropellant rockets. Although current cost estimates have proven that lunar-derived propellants might not be economical for cislunar space activities in the near future, the development of an ISRU O_2 production facility on the Moon might be beneficial to lunar missions and to lay the foundations for future deep-space exploration [7].

Nevertheless, oxygen is not the only resource that could be extracted from lunar soils. Lunar regolith also contains abundant metals and metalloids that could be potentially processed to build lunar infrastructure [8]. A closed-loop ISRU approach shall consist in maximizing the utilization of local resources, while adopting extensive recycling loops, similar to those already implemented in Environmental Control and Life Support Systems (ECLSS), for the materials transported from Earth [4].

This Master's thesis has been written under the umbrella of the German Aerospace Center's (DLR) newly founded research group on Synergetic Material Utilization (SMU). SMU combines ISRU and ECLSS engineering approaches to reduce the required material supply from Earth. Since both fields utilize similar resources, technologies, and processes, each field could potentially benefit from the outputs provided by the other field. Consequently, there is a high potential for synergies between ISRU and ECLSS. Among these synergies are a common water infrastructure, in-situ propellant generation, and the production of materials by exploiting ISRU and ECLSS byproducts.

1.1 Problem Statement

Before in-situ resource utilization is considered as a feasible alternative to transporting all material resources from Earth, the mass and performance of the necessary ISRU subsystems must be rigorously investigated. Following a holistic and multidisciplinary approach is essential when modeling ISRU concepts. The models cannot exclusively analyze and compare the oxygen extraction techniques. They must include the influence of the excavation, beneficiation, storage, or power subsystems to truly understand their benefits and drawbacks.

In the late eighties, the first parametric analyses of lunar oxygen facilities were published [9, 10]. These analyses focused on hydrogen reduction techniques to extract oxygen from lunar regolith. Eagle Engineering, Inc. [11] included, among other subsystems, an excavator, magnetic beneficiation, a water electrolysis cell, oxygen liquefaction and storage, and a thermal control subsystem. Analytical models were developed to predict the mass and power of each subsystem. This study has served as the foundation for later ISRU analyses that have studied the benefits of extracting oxygen from lunar regolith or water ice deposits [12].

During the first decade of the twenty-first century, studies assessing the feasibility of producing O_2 from water ice instead of from lunar regolith were also carried out [13]. Moreover, Steffen et al. [14, 15] began a new generation of ISRU system modeling that took a bottom-up approach. Improved kinetics models for the H_2 reduction were incorporated into the ISRU system framework, and carbothermal reduction was also included in the analyses [16]. More recently an integrated molten regolith electrolysis model has been developed by Schreiner [17, 18].

Monchieri et al. [19] performed a trade-off analysis of several ISRU processes by applying qualitative evaluation criteria. Although from this analysis, preferential O_2 extraction processes could be identified, no quantitative discussion of the overall ISRU facility mass and power was provided. Fereres et al. [20] also carried out a qualitative comparison between hydrogen reduction, carbothermal reduction, and molten salt electrolysis. However, this analysis focused on a small payload proof of concept and not on a large-scale ISRU facility.

Although integrated sizing models have been developed for individual ISRU O_2 extraction techniques, a unified holistic study that quantitatively compares the mass and power requirements of these ISRU techniques under an identical set of assumptions is still missing in the literature. The work developed in this thesis aims to fill this knowledge gap.

Moreover, the possibility of extracting metals from lunar regolith has been largely overlooked when analyzing the feasibility of the ISRU processes. Metal processing has the potential of further minimizing the dependency on terrestrial resources compared to only producing oxygen from lunar regolith. Although Hepp et al. [21] surveyed several lunar metal extraction techniques, the processing and refinement of those metals were neglected in the analysis. The work developed in this thesis also aims to quantify the mass and power requirements of different metal refining processes.

A case study is defined to narrow the scope of the thesis and to obtain a set of unified assumptions for the comparison of ISRU concepts. The case study goal is to determine which in-situ production concept is capable of yielding O_2 and useful byproducts while requiring the minimal amount of material resources brought to the Moon. Lunar metals and metalloids are byproducts of several oxygen extraction techniques and could be processed to build multiple infrastructure components. In this case study, the scope is limited to materials that could be used to manufacture a heat rejection radiator on-site. Radiators are a reasonably heavy piece of infrastructure required in any space mission. Being able to manufacture radiators on-site would easily facilitate the scalability of a long-term Moonbase. Therefore, this work also aims to identify which ISRU material concepts with potential thermal applications could be processed and refined after the O_2 extraction from regolith. Furthermore, it is desirable to quantify the possible heat rejection rate of an ISRU-manufactured radiator.

1.2 Methodology

To reach the goals described in Section 1.1, a sequential methodology is followed. A long-term lunar surface reference mission is first defined. The location of the reference mission is based on the regions of interest proposed by the international space agencies and space exploration research community. The reference mission definition includes the crew size, the Moonbase infrastructure, and the necessary oxygen production rate. Analogies to the International Space Station, which is the largest crewed habitat ever developed for long-term missions, are made. The thermal control system requirements are also determined, in particular for the radiator location and design.

Once the oxygen production rate and radiator design are defined, the indigenous resources capable of yielding O_2 and materials to manufacture a radiator on-site are investigated. Lunar environment conditions that might affect the processing of these resources must also be known. The information is gathered from extensive lunar manuscripts that analyzed the samples returned by the Apollo and Luna missions. They are complemented by published reports of the latest remote-sensing lunar observations.

The necessary stages to process the indigenous resources are identified. An overall ISRU process chain is defined. For each stage of the ISRU process chain, several processing techniques are discussed. The mass, volume, power, and cooling requirements of these techniques are modeled to understand the necessary equipment that must be transported to the lunar surface. ISRU processing techniques require supplementary power generation plants and heat rejection systems that impose mass penalties to the payload that must be initially launched from Earth.

Analytical models have been obtained from the literature, when available, to calculate the mass, volume, power, and cooling requirements. If possible, these models have been updated with the most recent findings. If a model was not readily available in the literature, it has been self-developed. The models developed in this thesis are based on previously published works, analytical calculations, data extrapolated from experimental research, and analogies drawn between terrestrial and space components.

Besides oxygen, the materials obtained from the ISRU process chain are characterized. Quantitative estimates of the mechanical and thermal properties, in particular yield strength and thermal conductivity, are provided when available. Experimental studies and analytical models are used to provided these values. If no quantitative estimates are found, the material properties are discussed qualitatively.

An algorithm is developed to deliver the feasible combinations of ISRU processes. The algorithm considers the constraints between the upstream and downstream stages, the material production rates, and the requirements of the radiator geometrical design.

Once the in-situ production concepts are defined and the materials characterized, three-dimensional thermo-fluid dynamic simulations are performed with Ansys™ to quantify the heat rejected to the environment and the amount of material that must be coproduced to manufacture the radiator on-site.

Finally, a multi-criteria analysis is carried out to evaluate the selected production concepts. The mass, volume, power, and cooling requirements for each ISRU process chain stage are scaled from the reference values obtained by the analytical models. The production concepts must produce the necessary oxygen rate and manufacture a radiator capable of rejecting the total heat generated by the Moonbase. An Equivalent System Mass (ESM) analysis that estimates the mass that must be initially brought from Earth is combined with a qualitative weighted evaluation of the ISRU process chain versatility. The analysis returns the most suitable in-situ material production concept. The ISRU process chain versatility aims to evaluate the advantages and disadvantages of the in-situ material production concepts that cannot be quantitatively included in an ESM analysis.

1.3 Outline

This thesis is organized into nine chapters. After introducing the objectives and methodology in Chapter 1, a lunar surface reference mission that uses ISRU techniques to produce oxygen and metals to manufacture a radiator is defined in Chapter 2. Two possible radiator designs are proposed in this chapter.

In Chapter 3, the most relevant lunar resources are summarized, focusing on the composition and properties of regolith, since it is the preferred feedstock for the in-situ material production concepts studied in this work.

Chapter 4 presents the overall architecture of an ISRU process chain focused on oxygen and metal extraction from lunar regolith. The most relevant ISRU technologies for each process chain stage are discussed. The mass, volume, power, and cooling requirements of each technology are quantified for the excavation, beneficiation, oxygen extraction, and metal processing stages. For the manufacturing stage, a qualitative analysis is conducted.

In Chapter 5, the byproducts yielded by the ISRU processes described in Chapter 4 are characterized with respect to their mechanical and thermal properties.

The single ISRU processes discussed in Chapter 4 are combined together to result

in entire in-situ material production concepts. Chapter 6 presents a systematic approach to select the possible combinations of processes. These combinations are also described in this chapter.

Chapter 7 corresponds to the three-dimensional thermal simulations conducted on the radiator designs described in Chapter 2. Iterating over the ISRU materials characterized in Chapter 5, these simulations quantify the heat rejected to the environment and help to understand which design would perform better.

In Chapter 8, a multi-criteria analysis is carried out to evaluate the in-situ material production concepts defined in Chapter 6. The multi-criteria analysis combines an ESM study with a qualitative weighted evaluation of the ISRU process chain versatility. A single in-situ material production concept is selected as the most suitable ISRU process chain to simultaneously produce oxygen for life support or propellant production, and metals to manufacture a radiator on-site.

Chapter 9 concludes the thesis. The main results are summarized and discussed. Additionally, the future lines of work are presented.

2 Reference Mission

The current Global Exploration Roadmap [22] suggests human lunar exploration as the next logical step towards the future exploration of the Solar System. The last report published by the International Space Exploration Coordination Group (ISECG) identified three main driving objectives for the development of lunar surface activities: performing lunar science and evaluating sustained human surface exploration, enabling the commercialization of cislunar space, and allowing the preparation for human Mars exploration [23].

This chapter defines a lunar surface reference mission in agreement with the objectives in order to provide context for the works performed in this thesis and to allow quantitative assessments of the ideas here presented.

2.1 Mission Location

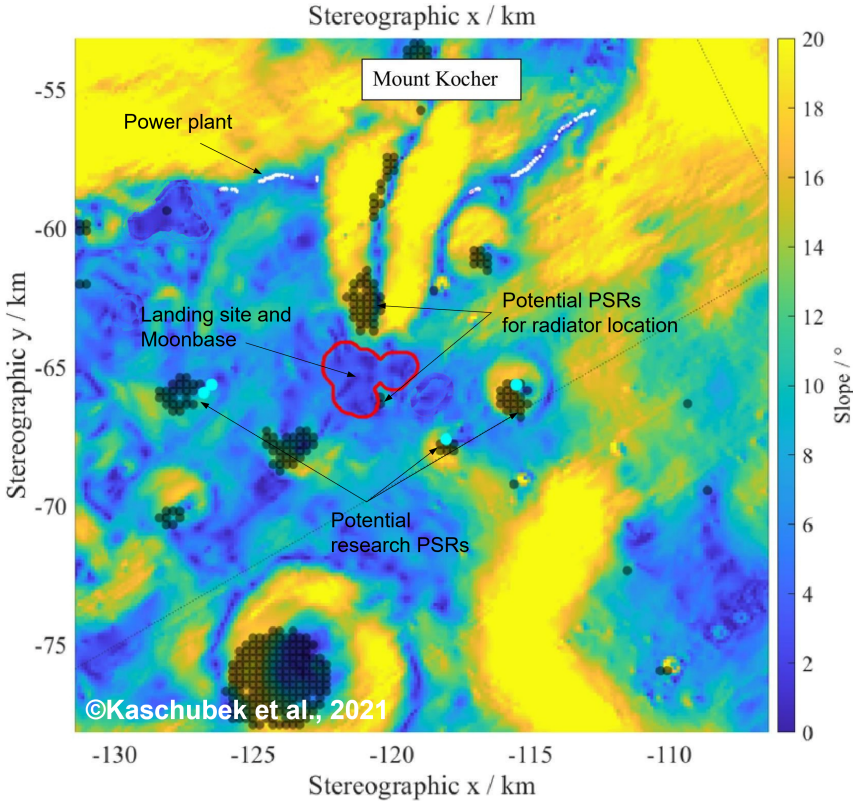

Fig. 2–1: Mount Kocher location. Black points indicate PSRs, white points POLs, and cyan points water ice spots. Adapted from [24].

Different regions of interest are under discussion as potential landing sites for the first human lunar surface mission of the twenty-first century. The focus is currently on the lunar South Pole due to the increasing evidence of near-surface volatile presence and potentially large amounts of lunar ice deposits in its Permanently Shaded Regions

(PSRs) [25, 26]. For these reasons, the selected reference mission targets the lunar South Pole. Its exact location is based on the analysis carried out by Kaschubek et al. [24].

The criteria to choose a region that would host a Moonbase are a terrain slope lower than 5° and accessible PSRs and Peaks Of Light (POLs) less than 10 km away from the base. From the landing sites proposed in [24], Mount Kocher is selected as the location of the lunar surface reference mission. Mount Kocher (85.5° S, 118.2° W) is located on a higher plane close to crater Kocher and has near-access to multiple middle-size PSRs. Some of the PSRs, which include spots of suspected water ice [27], could be potential research sites. Other PSRs might hold specific habitat infrastructure, such as parts of the Thermal Control System (TCS). Figure 2–1 displays the potential location of the landing site and the crewed Moonbase. The solar power plant shall be located in the vicinity of a POL region, where solar energy is accessible more than 75% of the year. The maintenance of the power plant would be shifted to the shadow phases. The PSRs, where water ice might be found, or where a TCS radiator might be placed to maximize the heat exchange with the environment, are also marked in Figure 2–1.

2.2 Base Infrastructure

ESA's Moon Village concept intends to count on scalable and flexible base infrastructure. For the initial exploration stages of the lunar surface, hardware is expected to be delivered by multiple landers before the crew arrives. This initial crew would consist of between four and six crew members (CMs). [3]

For the lunar surface reference mission of this thesis, a crew size of six CMs is selected. Following the concept proposed by Kaschubek et al. [24], the crewed lunar base is composed of an ISS-based Environmental Control and Life Support System (ECLSS) and an In-Situ Resource Utilization (ISRU) facility that allows a near closed-loop operation, except for food and miscellaneous parts. Both systems might be complemented by shared infrastructures that include a set of fluid tanks and a Regenerative Fuel Cell System (RFCS) as energy storage and power supply during shadow phases. Figure 2–2 displays a schematic representation of the described base infrastructure, highlighting the mass flows between subsystems. Two options are considered for the architecture of the Moonbase depending on the ISRU oxygen extraction process used (see Section 4.4).

Figure 2–2a presents a potential infrastructure including a H_2 reduction reactor as discussed in [24]. In this case, a CO_2 Solid Oxide Electrolysis Cell (CSOEC) is optionally included to generate carbon monoxide. Section 4.5.1 describes how CO can be used as part of one of the processes to produce refined iron from reduced ilmenite.

Figure 2–2b presents a potential infrastructure when Molten Regolith Electrolysis (MRE) or Molten Salt Electrolysis (MSE) are chosen as ISRU oxygen extraction processes. All these processes are discussed in Chapter 4 together with the entire ISRU production chain that allows the further utilization of regolith byproducts.

The Sabatier CO_2 Reprocessing Assembly (SCRA) combined with the O_2 extraction

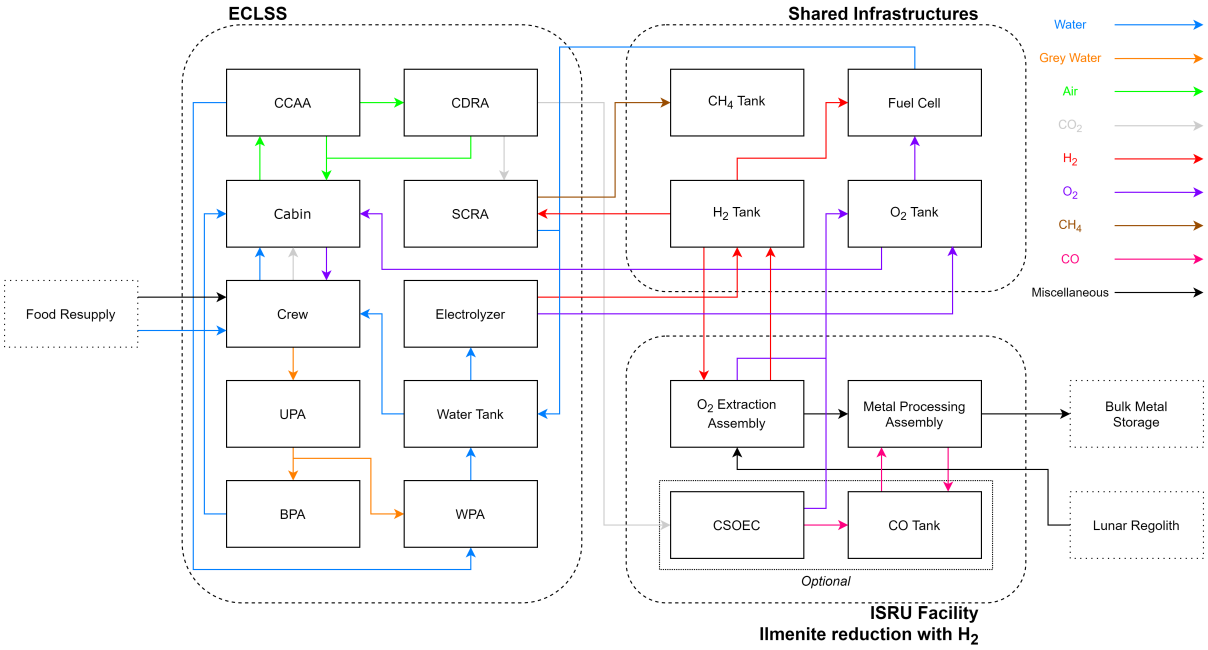

(a) ISRU facility: Ilmenite reduction with hydrogen.

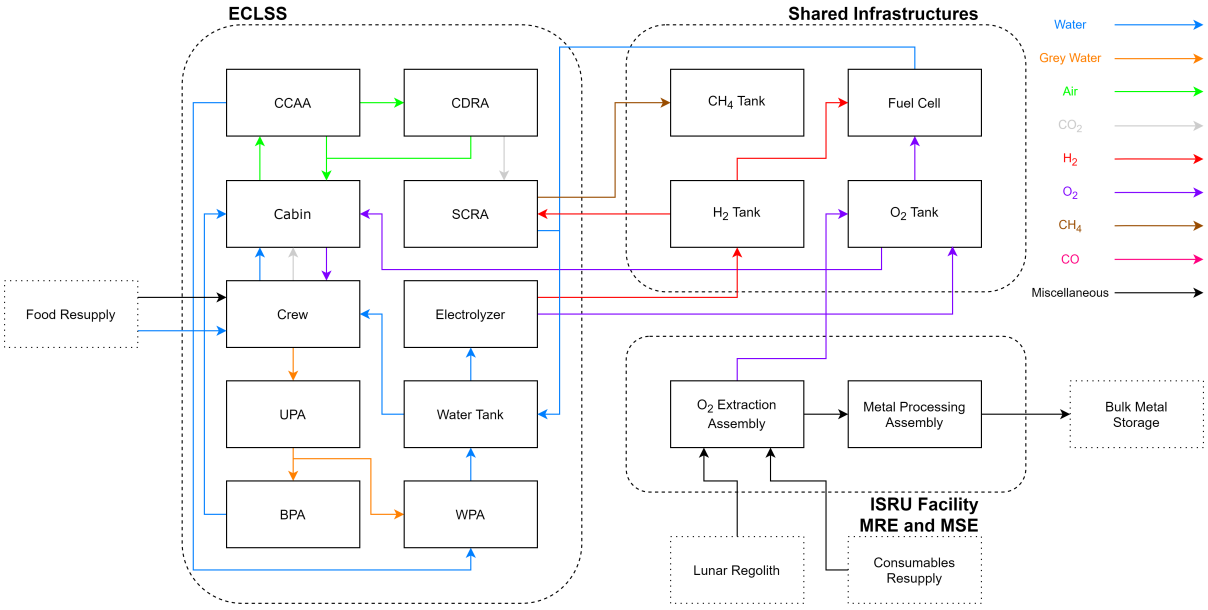

(b) ISRU facility: Molten regolith electrolysis and molten salt electrolysis.

Fig. 2–2: Schematic representation of the base infrastructure.

assembly can generate methane and additional oxygen as fuel for resupply missions. Rough estimations state that the oxygen needs for a potential lunar surface mission would be in the order of 0.5 t/y of O_2 for each CM. It would include the resupply needs of the ISS-based ECLSS and EVAs. The fuel demand of a lunar ascent module launch from the surface to Low Lunar Orbit (LLO) also requires 3.5 t of O_2. [28]

The amount of oxygen usable as fuel is constrained by the CH_4 available. Therefore, the limiting factor is the amount of carbon dioxide generated by the crew. Theoretically, the oxygen-to-methane mass ratio for rocket fuel is 4:1. Kaschubek et al. [24] report an ideal methane production of 830 kg/y for the base infrastructure discussed in Figure 2–2a. However, when detailed simulations are performed, taking into account the imperfections of the SCRA, this amount is reduced to 460 kg/y.

The O_2 extraction assembly in this thesis is dimensioned for an annual oxygen production of 15 t. This production rate could account for the 3 t/y of O_2 necessary for six CMs and for a rocket fuel production that allows three lunar ascents from the surface to LLO within a year. 10.5 t of O_2 and 2.63 t of CH_4 are required for three lunar ascents. Therefore, 2.17 t of CH_4 must be resupplied from Earth to have the appropriate rocket fuel ratio.

To dimension the metal processing assembly, it is assumed that the total amount of metallic byproducts generated during the extraction of O_2 are processed to produce refined metals.

2.3 Thermal Control System

A Moonbase thermal control system is required to remove the heat generated by the ECLSS and the ISRU facility. Thermal control techniques can be sorted into Passive Thermal Control (PTC) and Active Thermal Control (ATC) [29]. PTC techniques, such as heat pipes, are usually included in unmanned spacecraft, where reliability plays a vital role, and the amount of rejected heat is low. However, ATC techniques are generally more efficient [29].

Mechanically pumped fluid loops are ATC devices that transfer large amounts of thermal energy between two points through forced liquid convection. Mechanically pumped fluid loops are traditionally developed for crewed missions, where the amount of rejected heat is high, and the system can be maintained by the astronauts. [30]

A pumped fluid loop TCS similar to the one installed in the ISS is considered in this thesis. Figure 2–3 is a schematic representation of the thermal control system. An internal fluid loop, which is placed inside the crewed habitat, exchanges heat by means of a heat exchanger with an external fluid loop. The external working fluid flows through a radiator, where heat is released to the environment. The internal working fluid is water, and the external working fluid is liquid ammonia. A unified Moonbase pumped loop could be used as a thermal bus, where the TCS can simultaneously reject and supply heat at multiple locations through an optimized fluid piping layout. This design would reduce the thermal energy that must be supplied to the ISRU facility by, for instance, recycling the heat generated in the ECLSS or sharing the heat generated across subsequent ISRU processes.

Liquid ammonia is used in the ISS TCS as working fluid due to its high thermal capacity and wide range of operating temperatures [31]. The working fluid must not freeze on a single-phase loop, particularly at the radiator interface with the environment. The freezing point of NH_3 is 195 K, higher than the lunar surface temperature at certain locations

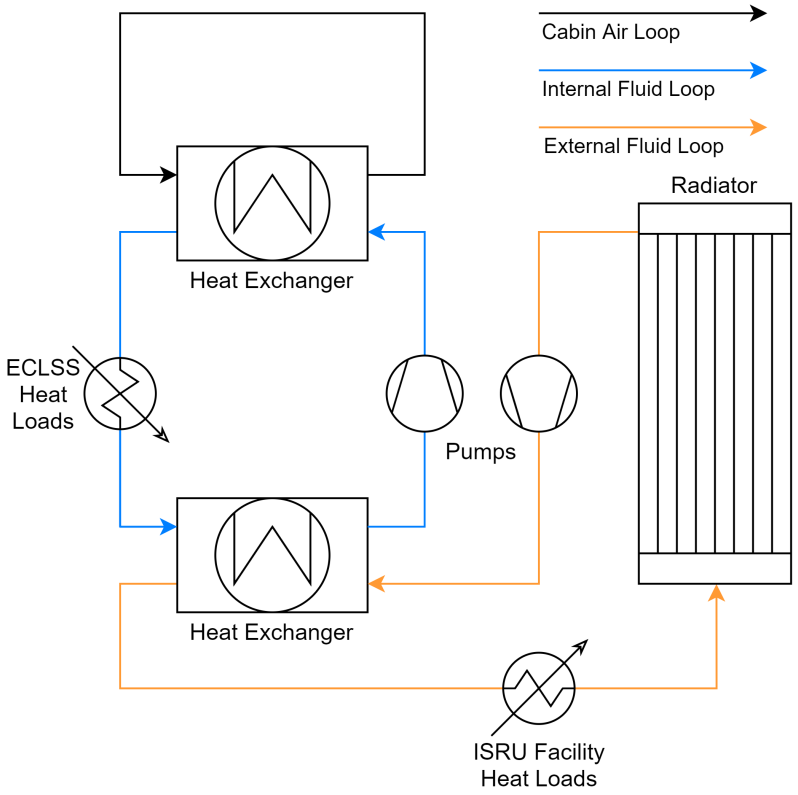

Fig. 2–3: Schematic representation of the thermal control system.

(see Figure 2–5). Specific radiator designs can avoid the freezing problem when the system operates at partial load [32, 33]. If these designs cannot totally prevent the working fluid from freezing, active heating shall be applied. Another possibility would be to replace NH_3 with other working fluid, such as Freon, which has a lower freezing point and thermal capacity [29], or develop specific coolant mixtures for extremely low temperatures [34].

The liquid-vapor phase change in the ammonia loop must also be prevented. The pumping unit is in charge of maintaining the operating pressure above the vapor pressure of NH_3. The nominal operating pressure of the ISS TCS ammonia loop is 21 bar [31]. Although the thermal properties and specific weight of NH_3 are superior to those of H_2O, liquid water is used as working fluid for the internal crewed loop due to ammonia toxicity if leakage occurs.

The radiator represented in Figure 2–3 rejects heat to the lunar surface and to outer space. Most of the thermal energy is rejected via radiative heat transfer. However, if the radiator is in direct contact with the lunar surface, conductive heat transfer would also occur.

From Figure 2–4, several parameters that determine the amount of radiative heat rejected from the radiator surface can be observed. The emittance (ε) and absorptance (α), which are optical properties of the radiator outer surface, are discussed in Section 2.3.2. Maximizing the radiator surface increases the amount of rejected heat. The

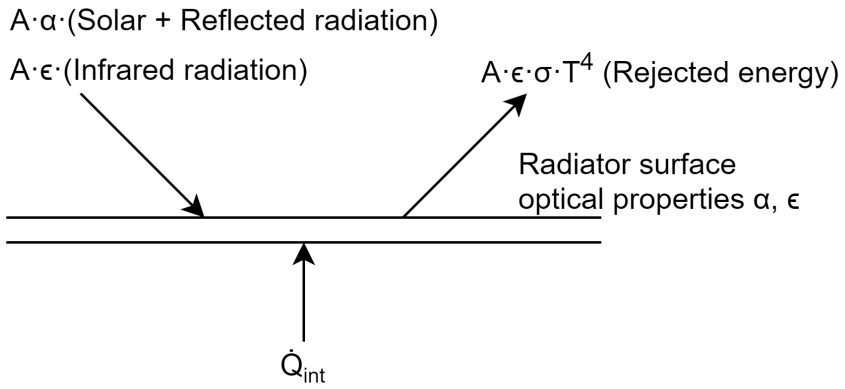

Fig. 2–4: Radiator energy balance [30]. Only radiative heat transfer is represented.

mass and volume associated to an increase of the radiator surface are usually limiting factors when the radiator must be brought from Earth. However, if the radiator is manufactured on-site, its mass and volume would not be design driving factors.

The position of the radiator on the lunar surface also influences its performance. On the equatorial lunar regions, the solar incidence angle is predominantly perpendicular to the lunar surface. Therefore, a vertical positioning is preferable due to the reduced solar radiation absorbed by the radiator [35, 36]. However, the solar incidence angle in the South Pole is almost parallel to the lunar surface. Thus, a horizontal radiator positioning would be more advantageous in this location. Moreover, a horizontal radiator positioning would also reduce the structural stresses withstood by the radiator due to its own weight, enabling the use of lower-quality materials that would be produced more easily on-site. A side of the horizontal radiator would completely face the lunar surface, exchanging heat with it rather than with outer space. This heat could be transferred via radiation if the radiator is raised above the lunar surface, or via conduction if the radiator is directly placed in contact with the surface.

The temperature difference between the radiator and the lunar surface also plays a vital role in the amount of heat rejected to the environment. As already discussed in Section 2.1, a permanently shaded region would be an ideal location for a TCS radiator. PSRs do not receive direct solar radiation, presenting cryogenic surface temperatures and reducing the amount of thermal energy absorbed by the radiator. Figure 2–5 displays the maximum and minimum surface temperatures of the Mount Kocher location represented in Figure 2–1. The potential PSRs that could host a TCS radiator present maximum and minimum surface temperatures of 120 K and 40 K, respectively. The maximum temperatures are reached during the summer lunar season and the minimum temperatures during the winter lunar season. The TCS radiator must be able to reliably operate throughout the entire temperature range.

Although other near PSRs have lower temperatures during the summer season, which would increase the heat rejection to the environment, they are potential locations of water ice deposits. Placing a radiator in these regions would potentially vaporize the deposits. Therefore, these PSRs have not been considered TCS radiator holders.

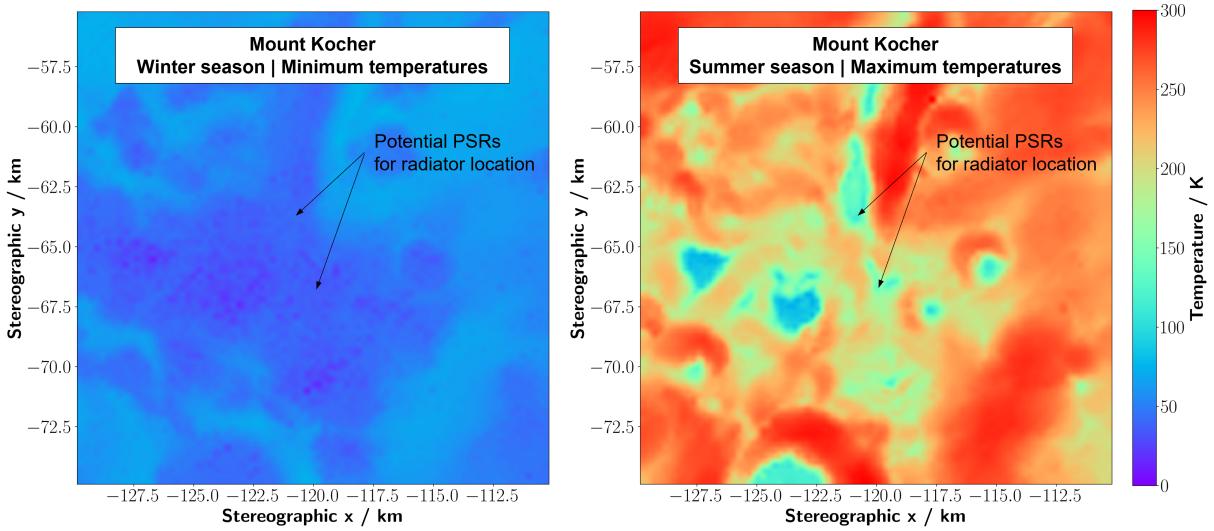

Fig. 2–5: Mount Kocher surface temperatures. The left figure represents the minimum temperatures reached during the winter lunar season. The right figure represents the maximum temperatures reached during the summer lunar season. The data has been obtained from the Diviner Lunar Radiometer Experiment (DLRE) onboard the Lunar Reconnaissance Orbiter (LRO) [37, 38].

2.3.1 Radiator Structure

The internal heat loads represented in Figure 2–4 are transferred to the radiator surface via forced convection of the working fluid and conduction across the radiator structure. Therefore, the thermal conductivity of the solid structure influences the overall performance of the radiator. Moreover, the structural material is responsible for withstanding the thermal and mechanical stresses suffered during operation. Thus, the yield strength is a relevant mechanical property of the structural material. Other relevant mechanical properties are the corrosion resistance with respect to the working fluid and the material hardness. Hard materials play a vital role in preventing working fluid leaks due to micrometeorite impacts.

Complex aluminum alloys are traditionally used as radiator structural materials for space applications due to their satisfactory combination of lightweight design, thermal conductivity, and strength [39]. However, this work also analyzes the thermal and mechanical properties of material concepts that are more easily produced on-site.

To limit the scope of this work, the following sections only describe two different radiator concepts. Both concepts differ on their geometrical design and, therefore, on their heat rejection rate. The manufacturing techniques that are used to directly produce them on-site might also be different. A state-of-the-art design based on the ISS radiators and a simpler tubular design are investigated.

2.3.1.1 State-of-the-art Radiator

The International Space Station is the largest crewed habitat ever developed for long-term missions. Therefore, most of its subsystems can be considered state-of-the-art

designs for space applications. Oren and Howell [32] provide a detailed description of the ISS heat rejection subsystem radiator assembly and its development. A geometrical radiator design based on [32] might be a possibility for the heat rejection subsystem of the Moonbase TCS considered in this work.

The ISS radiator assembly is modular. Each module is composed of two exterior 0.025 mm thick Al 6061-T6 face sheets and a 1.7 cm thick Al 5052 honeycomb core [32]. However, on-site manufacturing on the lunar surface does not critically require lightweight designs. Therefore, the proposed Moonbase radiator design is formed of a single solid material piece. This approach relaxes the manufacturing constraints, avoids using adhesive materials, and returns a higher mechanical strength compared to a honeycomb core. Since a higher mechanical strength can be expected, the radiator thickness is reduced to 1 cm compared to the ISS design. The module provides 16.22 m^2 of radiating area. Figure 2–6 and Figure 2–7 are representations of the radiator module.

Each module possesses a hot supply and a cold return ammonia flow path, which are located along the panel edges. The supply and return flow paths are connected through 22 flow tubes that perpendicularly cross the radiator panel. The internal diameter of the flow tubes is 1.73 mm. In the ISS, the flow path and tube materials are Inconel 718. However, to simplify the on-site manufacturing requirements, in the proposed Moonbase radiator, the tubing system is directly built within the solid structure, avoiding the use of multiple materials. To prevent ammonia from freezing, the supply and return flow paths are insulated with MLI, and the flow tubes are arranged in a specific configuration instead of equidistantly distributed. [32, 33]

To manufacture this complex radiator geometry as a single solid piece, additive manufacturing techniques are proposed in this thesis (see Section 4.6.3). Multiple modules can be connected in parallel or in series [32] to increase the radiating area. In the ISS, flexible hoses connect the flow path tubes between panels. However, to reduce the manufacturing requirements, rigid tube connectors are proposed to couple multiple modules using the same additive manufacturing techniques as for the radiator panel.

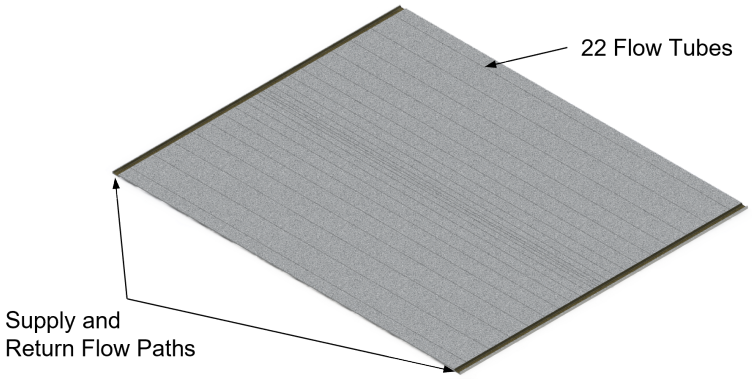

Fig. 2–6: Rendered state-of-the-art radiator. The figure represents a horizontal section of a state-of-the-art radiator module.

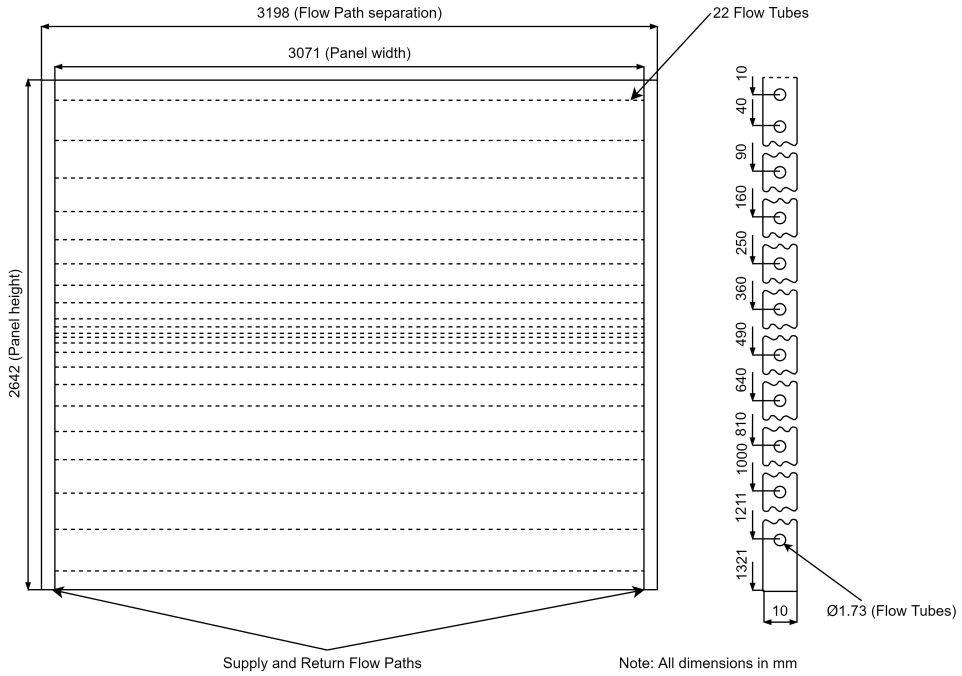

Fig. 2–7: Schematic representation of the state-of-the-art radiator. The left sketch represents a plan view of the radiator module. The flow tube configuration is illustrated by the dashed lines. The right sketch represents a section of the radiator module.

2.3.1.2 Tubular Radiator

A tubular radiator with a simpler design than the state-of-the-art radiator is also investigated. The radiator is composed of multiple tubes that directly reject heat to the environment. Each tube can be considered a single module. Modules are connected in parallel through supply and return manifolds. Extrusion is proposed in this thesis as the tube manufacturing technique (see Section 4.6.2). Rigid tube connectors can be manufactured by casting (see Section 4.6.4), with or without a subsequent machining process, or by additive manufacturing (see Section 4.6.3). Tube benders might be used to compact the design (see Figure 2–8).

Analog to the state-of-the-art radiator, if a specific distance is maintained between modules, it might be possible to prevent the working fluid from totally freezing at partial thermal loads (see Figure 2–9). The manufacturing techniques used for the tubular radiator can produce additional pipes for multiple habitat infrastructure components.

A tubular radiator module is composed of a hollow cylinder of a specific diameter and length. To allow a better comparison between designs, the radiating area of the state-of-the-art and tubular radiators is equal. A simplified thermal analysis, based on Equations 2–1 to 2–5, is carried out to select an adequate diameter-to-length ratio. Equation 2–1 represents the convective-conductive heat transfer across the tube. T_f is the temperature of the working fluid, and T_{wall} the temperature of the outer wall. R is the inner

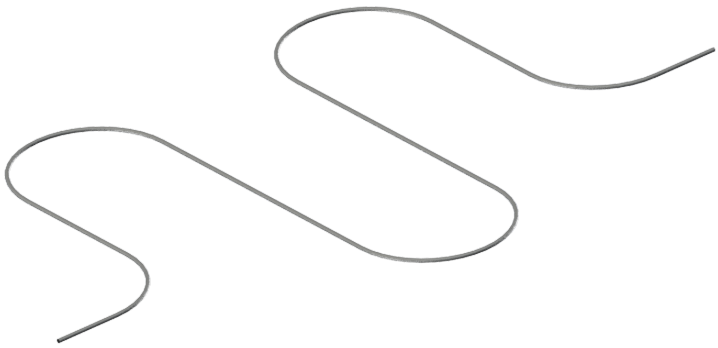

Fig. 2–8: Rendered tubular radiator.

tube radius, t the wall thickness, and L the tube length. The thermal conductivity of the structural material is k_{st}. The convective heat transfer coefficient (h) of the working fluid is calculated using Equation 2–2. Nu is the Nusselt number, considered 4.36 for a fully developed laminar flow [40], and k_f the thermal conductivity of the working fluid.

$$\dot{Q} = \frac{2 \cdot \pi \cdot L \cdot (T_f - T_{wall})}{\frac{\ln\left(\frac{R+t}{R}\right)}{k_{st}} + \frac{1}{h \cdot R}} \tag{2–1}$$

$$Nu = \frac{2 \cdot h \cdot R}{k_f} \tag{2–2}$$

Equation 2–3 represents the radiative heat transfer between the outer wall and the environment. A_{ext} is the external radiator area, which is 16.22 m^2 and equal to the state-of-the-art radiator module. T_{env} is the environment temperature, assumed 3 K for outer space. $T_{Regolith}$ is the lunar surface temperature, which can be estimated from Figure 2–5. A view factor between the radiator and the lunar surface of 0.5 is considered. The emittance (ε) is discussed in Section 2.3.2. The Stefan-Boltzmann constant (σ) is $5.67 \cdot 10^{-8}$ kg/($s^3 \cdot K^4$). To carry out the analysis, a thermal balance on the outer radiator wall is performed. Therefore, $\dot{Q}$ from Equations 2–1 and 2–3 must be equal.

$$\dot{Q} = \sigma \cdot A_{ext} \cdot \epsilon \cdot (T_{wall}^4 - \frac{1}{2} \cdot T_{env}^4 - \frac{1}{2} \cdot T_{Regolith}^4) \tag{2–3}$$

Equations 2–4 and 2–5 define the geometrical and structural constraints to maintain a constant radiating area. A maximum operating pressure (p) of 35 bar is assumed for the working fluid [31]. S is the allowable structural stress and f the safety factor.

$$L = \frac{A_{ext}}{2 \cdot \pi \cdot (R + t)} \tag{2–4}$$

$$t = \frac{f \cdot p \cdot R}{4 \cdot S} \tag{2–5}$$

The thermal analysis, based on Equations 2–1 to 2–5, reports that the rejected heat ($\dot{Q}$) exponentially decreases with increasing tube diameters (see Figure 2–10). For the same radiating area, a larger diameter shortens the tube length, reducing the amount of fluid directly in contact with the inner tube wall and, therefore, decreasing the convective heat transfer coefficient. For a constant mass flow rate, a larger diameter reduces the working fluid velocity, further decreasing the convective heat transfer coefficient. Moreover, larger diameters require larger wall thicknesses, which return lower outer wall temperatures. Smaller tube diameters also have a lower minimum bending radius, allowing better surface use. However, small tube diameters can incur manufacturing challenges and might be more easily covered by Moondust, reducing their heat rejection capabilities if the radiator is placed directly on the lunar surface.

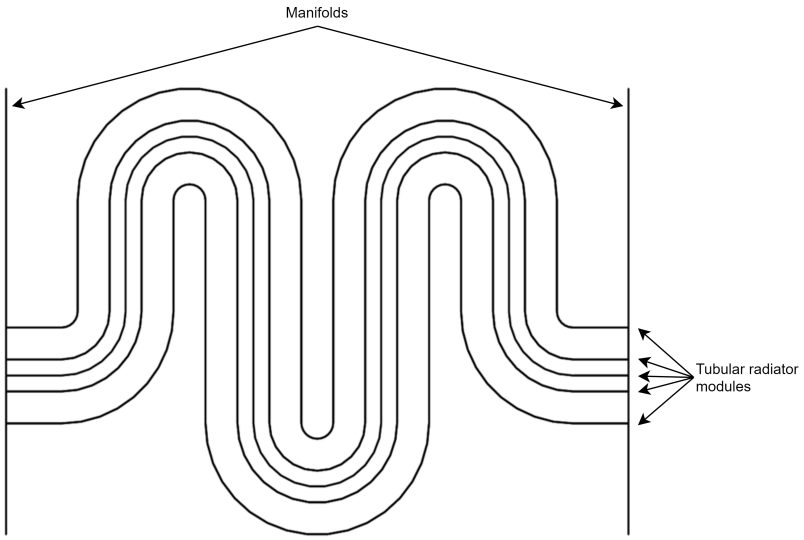

Fig. 2–9: Schematic representation of the tubular radiator assembly.

An inner tube diameter of 10 cm is assumed for this thesis. This pipe size is highly versatile and could be used for multiple infrastructure components other than the tubular radiator. An tube diameter of 10 cm is large enough to incur manufacturing limitations and shall be hardly covered by Moondust when placed on the lunar surface. For this tube diameter, a module length of 46.9 m is required and a tube bending radius of 20 times the diameter is chosen. A wall thickness of 5 mm returns a conservative design that is kept constant independently of the in-situ material production concept considered.

However, the selected tube diameter is a first-order estimation of a possible tubular radiator size. If the tubular radiator is proven to have a significantly better performance than the state-of-the-art radiator with respect to the evaluation criteria discussed in Chapter 8, a detailed analysis of the diameter-to-length ratio shall be carried out. Figure 2–10 reports that halving the tube diameter increases $\dot{Q}$ a 10%. Doubling and quadrupling the tube diameter, reduce $\dot{Q}$ a 15% and 30%, respectively.

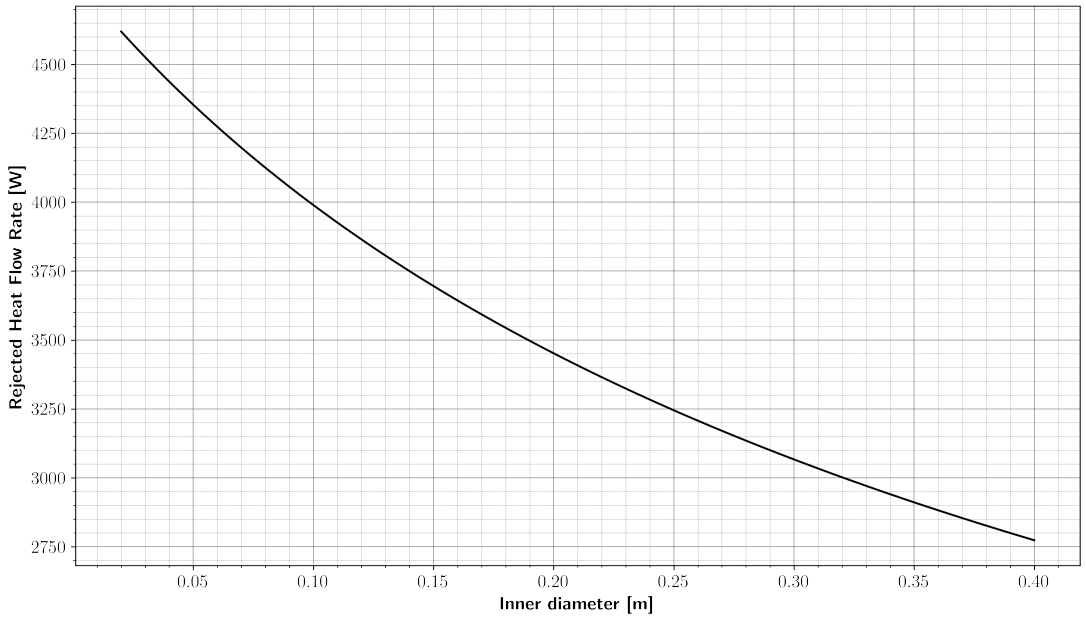

Fig. 2–10: Tubular radiator rejected heat flow rate as a function of the inner diameter.

2.3.2 Radiator Surface Finish

All physical objects absorb and emit thermal energy in the form of radiation. TCS radiators that release heat to the environment shall emit energy almost as a black body while minimizing their absorbed energy. Therefore, thermal-control coatings such as second-surface mirrors, white paints, and silver- or aluminum-backed Teflon, characterized by a high emittance (ε) and low absorptance (α), are usually applied to the outer surfaces of these radiators. [41]

Most of the mentioned surface finishes were originally designed for spacecraft applications, where the direct incidence of solar radiation is relevant. However, for the lunar surface reference mission discussed in this section, the radiator would be placed in a PSR and, therefore, shadowed from direct sunlight. The only external heat flows affecting the radiator would be the infrared radiation from the lunar surface and the reflected sunlight from the adjacent topography [27]. Due to this fact, the absorptance requirements of the outer surfaces might be relaxed.

The traditional space exploration problems of outgassing and mechanical adhesion to the substrate have both been resolved for most coatings [41]. Some surface finishes, such as white paint coatings, have a relatively inelastic behavior. Therefore, applying this type of coatings to surface materials that endure extreme temperature fluctuations and have high thermal expansion coefficients is undesired. Moreover, new challenges might arise on the lunar surface, in particular regarding the effect of Moondust in the optical properties of radiators under a continuous exposition. For shorter exposition times, lessons were learned from the Apollo program experience [42].

In this thesis, Z-93 white paint is selected as the reference surface coating of the radiator. Z-93 was used for both the Apollo Service Module and ISS radiators. Its emittance

is 0.92, and the absorptance at the beginning of life is between 0.17 and 0.20 [41]. Moreover, reliable data exists on the characterization of its solar absorptivity degradation in space environments, recommending a minimum coating thickness of 0.15 mm, It has been proven that this coating performs well in metal substrates [43]. Z-93 was firstly developed in the early 1960s by the Illinois Institute of Technology Research Institute (IITRI). However, nowadays, commercial versions of the coating are provided by various vendors such as AZ Technology or Alion Science and Technology, formerly IITRI [44]. From the product datasheets provided by the companies, the density of Z-93 is averaged to 1270 kg/m^3.

Other coatings such as silver-Teflon might also come into consideration depending on the actual surface finish of the radiator structural materials and its ease of in-situ application. However, Z-93 was chosen in this case due to its higher emittance and lower density.

3 Lunar Resources

Lunar and martian local resources will play a vital role in fulfilling the space exploration goals established by the ISECG and enabling a continuous and sustainable human presence on the lunar surface [23]. Prohibitive launch costs encourage the utilization of on-site indigenous resources to minimize the amount of oxygen and other supplies that must be brought from Earth to space [6]. To incorporate ISRU systems and capabilities into future space missions, it is necessary to first understand the amount, composition, and properties of extraterrestrial resources. This can be achieved through remote-sensing instruments or exploratory robotic and crewed missions [45]. In parallel, the necessary technology to extract useful materials from those resources can be developed on Earth. The first ISRU capabilities will be most likely demonstrated on the lunar surface due to the Moon being considered the next step towards the future exploration of the Solar System [22].

This chapter summarizes the most relevant resources available on the Moon, focusing on the composition and properties of lunar regolith as it is the preferred feedstock material for the in-situ material production concepts developed in this thesis.

The rocks found on the lunar surface can be classified into two main types of regions. Maria fill large impact basins composed of basaltic lava flows, whereas highlands represent the ancient lunar crust and are mainly composed of anorthositic rocks. Rocks are typically mixtures of several different minerals. For instance, basalts present in lunar maria are dominated by ilmenite ($FeTiO_3$), orthopyroxene ($(Mg, Fe)SiO_3$), clinopyroxene ($Ca(Fe, Mg)Si_2O_6$), and olivine ($(Mg, Fe)_2SiO_4$). Similar to highland anorthositic rocks, they also contain plagioclase, in which anorthite ($CaAl_2Si_2O_8$) predominates. [8]

Although the composition of mare and highlands significantly differs with the location, Table 3–1 presents rough estimates on the abundance of major lunar minerals in both types of regions. Mare rocks are further subdivided into high-Ti mare, richer in ilmenite, and low-Ti mare.

Lunar soils, also known as lunar regolith, are the unconsolidated layer of granular material that covers the entire lunar surface and has been generated over time due to the pulverization of rocks by meteorite and micro-meteorite impacts [47]. Due to its abun-

Tab. 3–1: Mineral composition ranges in vol.% of three different types of lunar rocks: Highlands, High-Titanium Mare, Low-Titanium Mare [46].

	Highlands (vol.%)	High-Ti Mare (vol.%)	Low-Ti Mare (vol.%)
Pyroxenes	5-35	42-60	42-60
Olivines	0-35	0-10	0-36
Plagioclases	45-95	15-33	17-33
Ilmenite	0-5	10-34	1-11

dance, characteristic properties, and relatively simple extraction process compared to solid rock, lunar regolith is an attractive source of raw materials such as oxygen, metals and metalloids, or water [6, 48]. Moreover, the oxygen and metal extraction from lunar regolith has been identified as the only ISRU production process that could be considered renewable for a sustainable long-term presence on the Moon [4].

The Lunar Sourcebook [49] and other lunar reports [50, 51, 52] already contain extensive data on lunar regolith characterization. However, the most relevant information is summarized in this section.

Lunar regolith is extremely fine, with an average particle size of 70 µm and a median particle size range between 40 and 130 µm. The first 15 cm of lunar soil have a medium to dense compaction. However, this compaction rapidly increases with depth. Below 30 cm, the relative density is considered to be very dense, making excavation tasks significantly harder when reaching deeper deposits. [53, 54]

Similar to lunar rocks, regolith also presents different compositions for mare and highland regions. Tables 3–2 and 3–3 show the average oxide and element composition, respectively, based on the data provided by Stoeser et al. [55] for the collected Apollo and Luna samples. As already discussed, lunar regolith is a direct source of oxygen with concentrations $>$40 wt.%. Highland regolith might be preferable for the extraction of Al and Ca, whereas Fe is considerably more abundant in mare regolith. Ti can be found in specific mare regions, known as high-Ti mare.

Although the oxide concentrations of regolith samples are usually provided from a chemical analysis perspective, it must be noted that these oxides are not found isolated in the lunar soil. They appear together in different types of minerals and cannot be treated as independent feedstock materials when analyzing ISRU oxygen and metal extraction processes [6, 48]. FeO and TiO_2 might be found combined in ilmenite, while anorthite might be the best available source of Al_2O_3 and CaO. A geological and mineralogical assessment of lunar regolith shall be a more suitable approach when analyzing its composition and adequacy for specific ISRU processes. Dry beneficiation techniques, as discussed in Section 4.3, might yield high-grade minerals. However, the direct isolation of single oxides without chemical processing might be impossible.

Most of the Apollo and Luna missions concentrated on the equatorial regions of the Moon, leaving the lunar poles highly unknown in terms of expected soil composition [56]. More recent remote-sensing missions have identified large masses of anorthositic highlands in the South Pole, except for the South Pole-Aitken Basin, where Fe-richer regolith is expected [8]. Mount Kocher, the location of the reference mission described in Chapter 2, lies on the edge of the South Pole-Aitken Basin. Consequently, FeO concentrations slightly higher than for traditional highland regolith might be found (see Figure 3–1).

As the access to actual samples of lunar regolith is extremely limited, terrestrial simulants are developed [57] to better understand its performance and properties during the investigation of ISRU oxygen and metal extraction processes and the simulation of lunar surface operations.

Tab. 3–2: Oxide composition in wt.% of the three different types of lunar regolith: Highlands, High-Titanium Mare, Low-Titanium Mare. Composition data from Apollo and Luna missions [55].

	Highlands (wt.%)	High-Ti Mare (wt.%)	Low-Ti Mare (wt.%)
SiO_2	44.90	41.00	45.10
FeO	6.20	16.60	17.00
Al_2O_3	25.10	12.40	13.10
CaO	14.90	11.40	10.70
MgO	7.50	8.90	9.90
TiO_2	0.50	8.50	2.90
Na_2O	0.42	0.40	0.40
P_2O_5	0.13	0.10	0.17
MnO	0.10	0.22	0.22
Cr_2O_3	0.14	0.37	0.37
K_2O	0.11	0.11	0.14

Tab. 3–3: Element composition in wt.% of the three different types of lunar regolith: Highlands, High-Titanium Mare, Low-Titanium Mare. Composition data from Apollo and Luna missions [55].

	Highlands (wt.%)	High-Ti Mare (wt.%)	Low-Ti Mare (wt.%)
O	44.60	40.90	42.40
Si	21.00	19.40	21.20
Fe	4.90	13.00	13.50
Al	13.30	6.60	7.00
Ca	10.70	8.30	7.70
Mg	4.60	5.50	6.00
Ti	0.29	5.30	1.80
Na	0.30	0.30	0.30
P	0.05	0.10	0.10
Mn	0.07	0.20	0.15
Cr	0.09	0.30	0.30
K	0.08	0.10	0.15

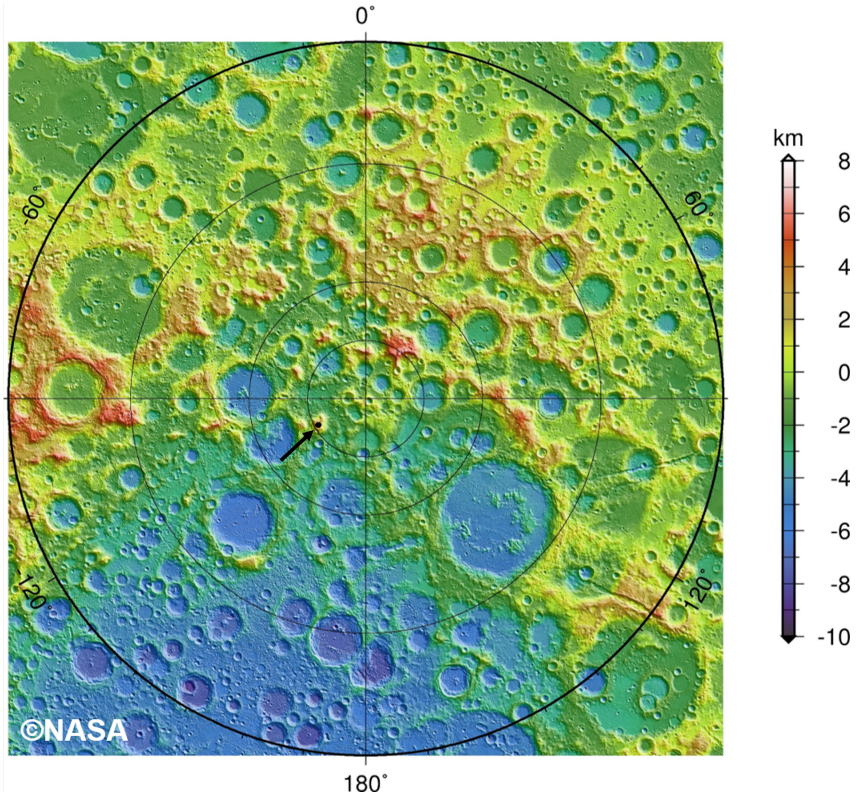

Fig. 3–1: LRO LOLA GDR elevation data for the Lunar South Pole (-60° to the pole) in stereographic projection [58]. The black point indicates the location of Mount Kocher. The blue regions at the bottom of the image correspond to the South Pole-Aitken Basin.

Thermophysical property models [59, 60] of lunar regolith shall also assist with the further development of ISRU techniques.

Minerals are not the only source of metals present in lunar regolith. Metallic iron particles appear from three different sources: meteoritic iron, iron released from disaggregated bedrocks, and iron produced from the reduction of iron oxides by solar wind hydrogen. However, these concentrations are considerably low, $<$1 wt.%. [61]

Iron is not the only element present in this form. At usually expected concentrations, a cubic meter of regolith could potentially yield not only 5 kg Fe but also 300 g Ni and 0.5 g of platinum group metals. A much higher concentration of these materials might be found in the vicinity of meteorites that survived the collision with the lunar surface. [8]

The iron oxide reduction by solar wind hydrogen mentioned above is possible due to the tenuous atmosphere and magnetic field of the Moon. Solar wind, mainly composed of helium and hydrogen nuclei, directly impacts the lunar surface, implanting ions into lunar regolith. These solar wind-implanted volatiles can be degassed from the regolith by heating them. Other volatile elements that might be also recoverable are C, N, F, and Cl. [8]

Although the Moon has generally been considered an anhydrous body, recent indirect measurements of the lunar surface might indicate the existence of a certain amount

of H_2O trapped at cryogenic temperatures. These water ice reservoirs are likely originated from the impacts of hydrated meteorites [8]. Of particular interest are PSRs near the lunar poles, where annual maximum surface temperatures stay below 110 K [27]. Although water ice would be a promising source of oxygen and hydrogen, the viability of exploiting this resource is still unclear due to the existing uncertainties concerning its location, concentration, and accessibility [62].

Although the lunar environment cannot be considered a material resource, it has some relevant properties that might also be exploitable. Solar radiation is the most readily available energy source. However, for most lunar surface locations, the lunar night lasts approximately 14 days. Certain regions, known as peaks of light, receive continuous sunlight for more than 90% of the year, and are essentially unlimited supplies of solar energy [8]. Severe temperature differences between the day and night cycle exist. Night-time and polar PSR cryogenic temperatures might be preferable for particular processes, as discussed in Chapter 2. The tenuous lunar atmosphere, sometimes considered vacuum from an Earth perspective, might facilitate some ISRU techniques such as metal refining, avoiding high concentrations of reactive atmospheric gases, and allowing trapped particles to easily escape from molten materials [63].

The actual pressure on the Moon highly depends on the lunar surface activity. Measurements carried out by Apollo 14 CMs reported a pressure of near 10^{-11} bar during astronaut operations. Furthermore, the landing module released large amounts of gases that locally distorted the lunar atmosphere in the short term. Pressures were also reported to vary during day and night cycles, presumably, due to the release of absorbed gases present in the lunar soil. After the conclusion of the Apollo 14 mission, data continued to be received. During the night, pressures in the order of 10^{-15} bar were measured, whereas, during the day, the pressure rose to 10^{-13} bar. [64]

Vapor pressures drastically decrease with temperature, allowing certain metals to sublimate when adding reasonably low heating energies [65]. This fact would encourage the development of new material refining techniques that are not available on Earth. Gravity on the lunar surface is approximately one-sixth of Earth's gravity (1.62 m/s^2). It can also be challenging issue for certain ISRU operations. For example, it might complicate the manipulation and processing of the finest regolith particles [20].

4 ISRU Process Chain

Although water ice has been detected at the lunar poles and might be a promising source of oxygen and hydrogen, the viability of exploiting this resource is still unclear due to the existing uncertainties with regard to its location, concentration, and accessibility. As water ice is expected to be found in permanently shaded regions, extraction and handling operations might become more difficult than in warmer surface areas. [27, 66, 62]

Lunar regolith is, however, a more direct source of oxygen, with a concentration >40 wt.% (see Table 3–3). It can be processed during the early exploration stages of the lunar surface to account for ECLSS and fuel resupply requirements, reducing the amount of material that must be launched from Earth. Moreover, during the oxygen extraction process, metallic byproducts are generated. These byproducts can be further refined to manufacture habitat and infrastructure components.

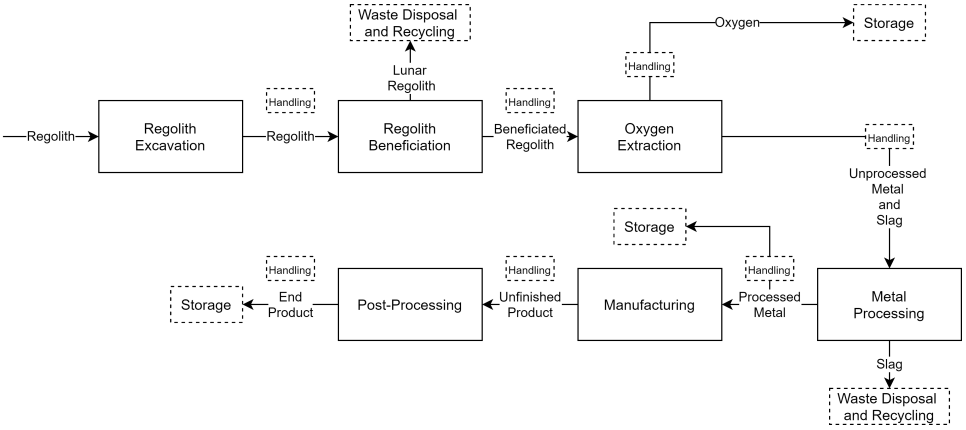

Fig. 4–1: High-level overview of the ISRU oxygen and metal extraction from regolith process chain.

Figure 4–1 presents a high-level overview of an ISRU process chain with focus on the oxygen extraction from regolith and the further processing of metallic byproducts for manufacturing purposes. In the first stage, the feedstock is excavated. Through handling processes, the regolith reaches an optional beneficiation step where the composition of the feedstock is improved. This step might be necessary to meet the requirements imposed by the oxygen extraction process, or to obtain a metallic byproduct with a desired composition and properties. The beneficiated regolith advances in the ISRU process chain, while the remaining regolith might be recycled (e.g., used to manufacture infrastructure parts through sintering [67, 68]) or disposed of. At the oxygen extraction stage, O_2 is obtained, processed, and stored for further utilization. The exact composition of the metallic byproduct depends on the introduced feedstock and the selected oxygen extraction process. In general, it can be defined as a mixture of unprocessed metal and slag. Through a series of techniques, the metal is refined and separated from the slag. This metal can be stored or directly used for manufacturing

purposes. The remaining slag is usually discarded. However, if it still contains useful resources, it could potentially be further processed. The manufactured products might be subject to an additional post-processing step before they can be used as end products.

This chapter discusses the most promising ISRU technologies for each process chain stage. The mass, volume, power, and cooling requirements of each technology are quantified.

4.1 Regolith Excavation

Although excavation is the first step in the ISRU process chain, little research has been carried out in this area. Most of the design concepts presented are still at a low Technology Readiness Level (TRL). A thorough review of existing regolith excavation techniques has recently been done by Just et al. [54]. For a deeper understanding of the current state of the art of ISRU excavation technologies, the reader is directed to this work and its references. However, in this section, the most relevant statements are summarized.

Regolith excavators must be specifically designed to withstand the effects of the harsh lunar environment and to operate under the reduced gravity present on the Moon. Therefore, they cannot be scaled-down concepts of terrestrial mining equipment. Two main groups of excavator designs have been tested for regolith extraction purposes: discrete excavators and continuous excavators. Discrete excavators need to break contact with the soil surface between cuts to dump the excavated material and clear the cutting surface. Examples of discrete excavators are front-end loaders, dozers, or backhoes. Continuous excavators have multiple cutting surfaces that are always in contact with the soil. When a cutting surface has gathered a certain amount of soil, it breaks contact with the ground, and the next cutting surface starts accumulating soil. Examples of continuous excavators are bucket wheels or bucket chains. [54]

Continuous excavators are characterized by a lightweight operation [69]. They would, therefore, be preferable in the initial exploration stages of the lunar surface, when most of the necessary equipment must be brought from Earth. Within the group of continuous excavators, bucket drums might be more promising than bucket wheels, as there is no need for an additional transportation system such as mobile platforms, haulers, or conveyor belts [54].

From the bucket wheel concepts collected by Just et al. [54], NASA's Regolith Advanced Surface Systems Operations Robot (RASSOR) project has the most advanced TRL (TRL 4) [70, 71, 72, 73] and, therefore, is selected as the reference vehicle to perform the regolith excavation operations for the concepts proposed in this work.

RASSOR, with a mass of 66 kg and a payload capacity of 80 kg, would be able to yield 0.38 kg of vehicle mass per kg of excavated regolith per working hour [71]. As each 24 hour period would consist of 16 hours of excavation and eight hours of battery recharging, this would mean an actual vehicle mass of 0.57 kg per kg of excavated regolith per hour.

Fig. 4–2: Regolith Advanced Surface Systems Operations Robot (RASSOR) [74].

The latest RASSOR tests report an increased payload capacity of 90 kg. The unit is able to excavate and transport within a 100 m range 1800 kg of regolith per battery charge (1410 Wh). However, no data is given on the actual excavation mass rate of regolith in kg/h. [73]

Although no dimensions have been found in the literature, the volume of the vehicle has been estimated using online imagery (see Figure 4–2) and single component dimensions [75]. The estimated volume is 1 m^3, which means a mass-to-volume ratio of 66 kg/m^3. This compact mass-to-volume ratio is achievable due to its lightweight and foldable design.

The power per mass of excavated regolith rate reported in [71] is 4 W/kg. Newer values for the energy requirements (0.761 Wh/kg) are stated in [73]. However, no testing time conditions are provided to derive the necessary power.

Table 4–1 presents the RASSOR mass, volume, power, and cooling requirements to excavate 1000 t/y of regolith. These estimated values from in-development lunar regolith excavators are considered a reasonable improvement over the ones provided by older sources, where analogies to terrestrial mining equipment or analytical calculations had to be made [11, 13]. Nevertheless, the values provided in this work shall become more accurate in the future once research focuses more on this stage of the ISRU process chain.

Tab. 4–1: Excavation summary of the mass, volume, power, and cooling requirements for 1000 t/y of excavated regolith.

Component	Mass (kg)	Volume (m^3)	Power (W)	Cooling (W)
RASSOR	66	1	320	0

4.2 Handling

Along the ISRU process chain, multiple stages are recursively necessary (see Figure 4–1). These stages can be grouped in a general handling stage that includes: the movement and transportation of mass flows of different nature, its storage, the disposal of waste products, or the recycling of valuable materials. Ideally, a characterization step of the mass flow properties would be performed in between the main stages. It would serve as quality control and, therefore, increase the efficiency and efficacy of the processes [54].

The transportation of mass flows is a broad concept that is present along the whole ISRU process chain. Hooper lift systems and conveyor belts have been proposed to move the regolith between the excavation, beneficiation, and oxygen extraction stages [72]. Additionally, a piping system would be necessary to lead and separate processed gases. In the later stages of the ISRU process chain, the transportation system shall be adapted to deal with mass flows that might be found in a molten state.

Pressure vessels or cryogenic deposits might be used to store gases. The literature provides values of the required tank mass per mass of stored gas for O_2, H_2, and N_2 [13, 76]. Carbon monoxide, a possibly necessary gas in the concepts proposed in this work (see Figure 2–2), might be comparable to N_2 in terms of storage performance due to a similar molecular weight. For other gases (e.g., methane), analytical calculations analog to [11] shall be performed. Storage tanks are also necessary for fluids such as water, whose tankage mass values can be found in [13]. Additional storage space would also be required for refined raw materials or end products.

Even during the initial exploration stages of the lunar surface, when local resources might still be relatively abundant, the costs of bringing materials from Earth, as well as the restricted area of influence of each lunar mission, would encourage the development of advanced waste management processes that allow a high level of resource recycling and reusability, while reducing the waste disposal. A sustainable human presence on the lunar surface would mean adopting closed-loop schemes for ISRU processes similar to those already implemented in ECLSS [4].

The infrastructure described above is not neglectable in terms of necessary mass that must initially be brought from Earth, and in terms of energy consumption. Nevertheless, the handling processes are omitted from the analysis performed in this thesis since ISRU is still in its early development stages. Researchers have focused on the main chain processes, leaving the requirements for the in-between processes highly undefined. Moreover, the required auxiliary infrastructure is expected to be shared among the in-situ material production concepts discussed in Chapter 6, and, consequently, the minor differences would not impact significantly the results of the analysis.

4.3 Regolith Beneficiation

Beneficiation has been proposed in Figure 4–1 as the second stage of the ISRU process chain. Beneficiation involves transforming lunar regolith into a suitable feedstock

before its chemical processing. It increases the efficiency of the oxygen extraction process and allows the obtention of byproducts with specific compositions [77].

A thorough review of regolith beneficiation techniques, including particle size separation and mineral enrichment, has recently been done by Rasera et al. [78]. For a deeper understanding of the current state of the art of ISRU beneficiation technologies, the reader is directed to this work and its references. However, in this section, the most relevant statements are summarized.

On Earth, beneficiation techniques require vast amounts of fluids, typically liquid water, to separate different ore components. They also rely on gravity to exploit their differences in mass, density, and volume. However, fluid processing must be avoided on the lunar surface. Although air cyclones have been mentioned by Williams et al. [77], and pneumatic concepts have been developed by Honeybee Robotics [79] for particle size separation, the long-term use of these technologies might not be viable. Fluids are consumables not readily available on the lunar surface. They would, therefore, have to be regularly transported from Earth.

Dry separation techniques have been proposed in the context of in-situ resource utilization to improve the composition and size distribution of regolith feedstock. Terrestrial gravitational beneficiation processes could be used to separate regolith particles by size. However, these processes must be adapted to operate under reduced lunar gravity. Electrostatic separation methods rely on how charged particles behave in electrostatic fields. These methods can be used to sort regolith particles by size, or to enrich minerals by exploiting their electrical conductivity differences. Ore minerals can be categorized by the way in which they interact with magnetic fields. They can be classified as diamagnetic, paramagnetic, or ferromagnetic. Magnetic separation methods can enrich minerals by exploiting how they react under magnetic fields of different strengths. [78]

More recently thermal decomposition has been proposed to recover specific regolith oxides, such as FeO, at moderate temperatures under ultra-high vacuum conditions [80].

Once the most relevant ISRU beneficiation methods have been discussed, the mass, volume, power, and cooling requirements of an ilmenite and anorthite enrichment assembly are presented in the following sections. The assemblies are based on fluid-free processing techniques. Ilmenite ($FeTiO_3$) is the most abundant iron oxide mineral in lunar regolith. It can be reduced with hydrogen to produce oxygen. Other FeO-rich minerals can also be beneficiated in an ilmenite assembly to enhance the extraction of Fe for ISRU manufacturing purposes. Anorthite ($CaAl_2Si_2O_8$) is the principal source of aluminum in lunar regolith and can be processed to extract Al for ISRU manufacturing purposes.

4.3.1 Ilmenite Enrichment

In Section 4.4, several oxygen extraction processes are presented. The chemical reduction of FeO-rich regolith minerals with H_2 is one of the principal processes dis-

cussed in this thesis. Table 3–2 reports typical FeO concentrations of 6 wt.% for highlands regolith and 17 wt.% for mare regolith. Ilmenite ($FeTiO_3$) is the most abundant iron oxide mineral in lunar regolith. Its concentration can be higher than 16 wt.% for high-Ti mare. However, in highlands regolith, this concentration can drop to less than 1 wt.%.

Even 16 wt.% of $FeTiO_3$ is far away from the ilmenite concentration of 80 wt.% reported by Gibson and Knudsen [81] for the chemical reduction of regolith with H_2. Therefore, excavated regolith must be beneficiated through mineral enrichment before entering the oxygen extraction stage. Gibson and Knudsen [81] also reported desired particle sizes between 20 µm and 200 µm. Sieving the coarse particle fraction ($>$200 µm) might improve the hydrogen reduction kinetics. Removing the fine particle fraction ($<$20 µm) could also enhance the performance and reliability of the oxygen extraction process, improving the flow dynamics and avoiding blockages in the fluidized bed reactors or feeders [82]. Therefore, the beneficiation stage shall be composed of particle size separation and mineral enrichment processes.

Gravitational methods can usually remove the coarse regolith fraction. Berggren et al. [82] suggest using a grizzly screen or a slotted ramp separator. Electrostatic [77, 83] and gravitational [84, 82] concepts have been proposed to separate the fine and medium regolith fractions. In an electrostatic sizer, regolith particles are initially charged and propelled due to their interactions with an electrostatic field [77]. Particles are discretely size-separated in different bins based on their trajectory under reduced lunar gravity and vacuum. The proposed gravitational sizers are based on differences in friction between medium and fine particles when flowing across a surface [82] or on their vibratory, shearing, or sonic behavior [84].

After the size separation process, the recovered regolith fraction could be enriched in $FeTiO_3$ through dry beneficiation methods. Two approaches that take advantage of the magnetic properties of lunar regolith components have been suggested to increase the ilmenite concentration.

A weak magnetic field could be applied to remove the agglutinate fraction [77, 85]. Besides the minerals presented in Table 3–1, lunar regolith is also composed of agglutinates and glasses. Agglutinates are formed by micrometeorite bombardment, which causes the welding and aggregation of smaller lunar regolith particles, such as minerals, glasses, or even older agglutinates [47]. Agglutinates also contain minute metallic Fe droplets. Therefore, ferromagnetic agglutinates easily interact with low-intensity magnetic fields, allowing its removal from lunar regolith [78].

$FeTiO_3$ could also be directly enriched by taking advantage of its particular magnetic properties. Ilmenite is paramagnetic, and, therefore, directly interacts with strong magnetic fields [78]. Bergreen et al. [82] proposed using drum separators and permanent magnets to increase the ilmenite concentration of mineral mixtures. Eagle Engineering, Inc. [11] also suggested using multi-stage permanent magnetic roll separators to increase the $FeTiO_3$ concentration of excavated regolith. Strong magnetic fields could also be used to enrich other FeO-rich minerals, which are also paramagnetic [82, 85].

Electrostatic separation based on the differences in electrical conductivity between $FeTiO_3$ and other regolith minerals is an alternative enrichment process to strong-field magnetic separation [78]. Several works have proposed conductive induction methods using slide separators, and tribocharging techniques using plate separation for lunar regolith beneficiation. A review of these works can be found in [78].

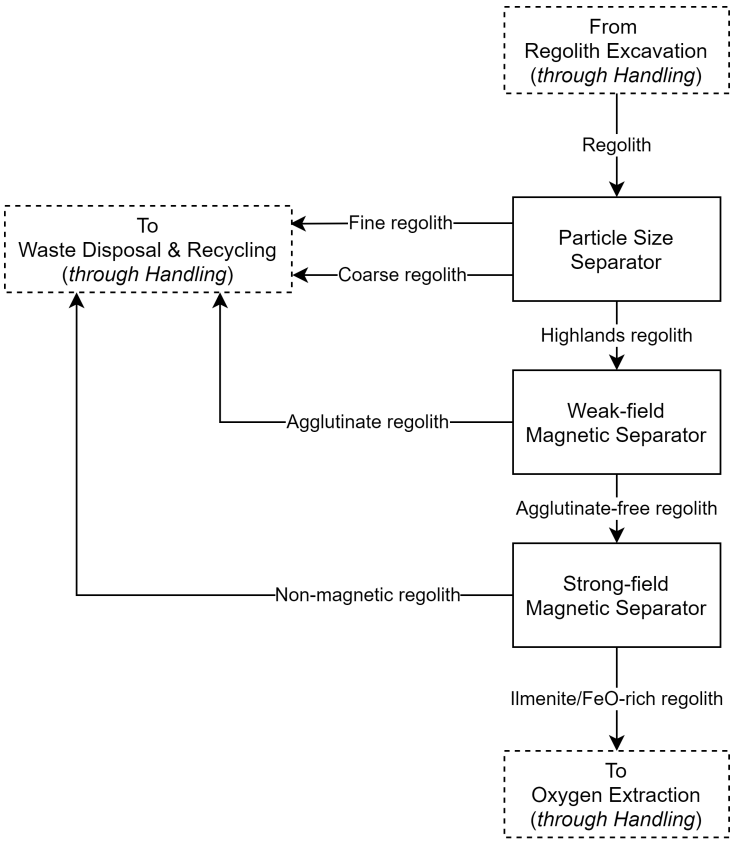

Fig. 4–3: Ilmenite enrichment assembly. Schematic representation based on [77, 85].

An ilmenite enrichment assembly is represented in Figure 4–3. Based on the designs proposed by Williams et al. [77] and Berggren et al. [85], the assembly is composed of a gravitational particle size separator and a weak-field magnetic separator that rejects the agglutinate fraction. The electrostatic separator proposed in [77, 85] is replaced by a strong-field magnetic separator that enriches $FeTiO_3$. Although magnetic separators are usually heavier and consume more power than electrostatic units [77], regolith must be heated from an environment temperature of 293 K to a processing temperature of 473 K before the electrostatic enrichment. Elevating the regolith temperature increases the electrical conductivity of $FeTiO_3$ and enhances the performance of the separation process [78]. Considering the regolith heat capacity reported in [59], 43 Wh/kg are required to increase the temperature 180 K. Since electrostatic separation would incur high mass penalties due to the required thermal energy input, strong-field magnetic separators are preferable. Moreover, strong-field magnetic separators are capable of separating not only ilmenite but other FeO-rich paramagnetic minerals [82].

The assembly components are investigated in terms of mass, volume, power, and

cooling requirements. Additional parts, such as feed bins or hoppers, used to transport the regolith between the separators, are considered part of the handling stage and, therefore, neglected in this analysis. The assembly is sized to process 197.5 t/y of ilmenite-rich regolith (80 wt.% of $FeTiO_3$). This processing rate produces 15 t/y of O_2 in a hydrogen reduction assembly (see Section 4.4.1). From Table 3–2, an approximate initial concentration of 1 wt.% of $FeTiO_3$ for highlands regolith can be derived.

The gravitational particle size separator is based on the experimental setup developed by Berggren et al. [82]. The coarse and fine regolith fractions are separated by two sequential slotted ramps. The gravitational particle size separator mass and volume factors are 150 kg and 0.15 m^3 per t/h of regolith, respectively. These factors have been estimated from the dimensions of the slotted ramp reported by [82], considering Inconel as structural material.

The medium particle fraction accounts for $\sim$35 wt.% of lunar regolith [82, 78]. Therefore, processing 60900 t/y of excavated highlands regolith would return 21300 t/y of medium-grained highlands regolith.

The weak-field magnetic separator model is based on the experimental setup developed by Berggren et al. [82]. A magnetic drum separator consists of a fixed inner cylinder and a rotating outer drum. The inner cylinder and outer drum structures are formed by a non-magnetic lightweight material capable of withstanding the harsh lunar environment. Half of the inner cylinder is covered by permanent magnets.

Regolith is fed at the top of a rotating drum. The agglutinate magnetic particles are attracted to the magnets attached to the fixed inner cylinder. The non-magnetic particles are propelled by dynamic forces and projected away from the rotating drum.

The magnetic separator mass, volume, and power factors are 20 kg, 0.2 kW, and 0.03 m^3 per t/h of regolith, respectively. The mass and volume factors have been estimated from the permanent magnet and outer drum dimensions reported in [82]. Both factors have been increased 1.5 times to account for additional lightweight structural materials that compose the separator. The power factor accounts for the outer drum electric drive motor.

Agglutinates have an average concentration of 33.34 ± 12.36 wt.% in lunar soils [47, 86]. If a magnetic separation efficiency of 0.93 is considered [77], processing 21300 t/y of medium-grained highlands regolith would return 13200 t/y of agglutinate-free highlands regolith. If no $FeTiO_3$ is lost during the magnetic separation process, the ilmenite concentration would increase from 1 wt.% to 1.5 wt.%. However, some of the ilmenite might be incorporated into the agglutinates and would not be recoverable by magnetic separation techniques [77].

The strong-field magnetic separator is sized using the Induced Magnetic Roll (IMR) model developed by Eagle Engineering, Inc. [11]. Although permanent magnets would require a lower mass, volume, and power, IMR allows the dynamic adjustment of the magnetic field strength, which improves the flexibility of the system [11]. The mass and volume factors are 1043 kg and 1.03 m^3 per t/h of regolith, respectively. The expression 0.7 kW + 0.602 kW per t/h of regolith can be used to estimate the power.

If a recovery efficiency of 80% is considered, 13200 t/y of agglutinate-free highlands regolith ($\sim$1.5 wt.% of $FeTiO_3$) could yield 197.5 t/y of ilmenite-rich regolith (80 wt.% of $FeTiO_3$).

Table 4–2 summarizes the mass, volume, power, and cooling requirements of an ilmenite enrichment assembly that processes 197.5 t/y of ilmenite-rich regolith (80 wt.% of $FeTiO_3$). A duty cycle of 0.75 is assumed. It must be noted that the beneficiation stage has been largely overlooked compared to the oxygen extraction stage [78]. The models considered in this analysis are first-order approximations based on scaled experimental setups or terrestrial equivalencies, which are not optimized for space applications. Moreover, the regolith mineral composition and particle distribution have been derived from the samples collected by the Apollo and Luna missions almost half a century ago. Even with the assistance of lunar regolith simulants, the enrichment grade and recovery efficiency that could be reached under a lunar environment are still highly uncertain.

The selection of electrostatic or strong-field magnetic beneficiation methods might depend on the initial ilmenite concentration of lunar regolith. The latest studies have focused on electrostatic instead of strong-field magnetic separation techniques [85, 87]. However, these studies do not assess the downside of heating the lunar regolith to enhance the electrical conductivity differences. When the initial ilmenite concentration is very low, as for highlands regolith, vast amounts of lunar soil must be processed to reach the appropriate ilmenite concentration. In this case, the required thermal energy does not favor using electrostatic separation methods. If lunar regolith heating is proven unnecessary, or if the initial ilmenite concentration is significantly high, as for high-Ti mare, electrostatic methods might be superior to strong-field magnetic separators due to a higher expected recovery efficiency. However, as reported by Rasera et al. [78], several knowledge gaps must be closed before being able to make these decisions.

Tab. 4–2: Summary of the mass, volume, power, and cooling requirements of an ilmenite enrichment assembly that processes 197.5 t/y of ilmenite-rich regolith (80 wt.% of $FeTiO_3$).

Component	Mass (kg)	Volume (m^3)	Power (W)	Cooling (W)
Particle Size Separator	1390	1.39	0	0
Weak-Field Magnetic Separator	65	0.10	650	0
Strong-field Magnetic Separator	2086	2.06	1904	0
Total	3541	3.55	2554	0

4.3.2 Anorthite Enrichment

Highlands regolith is mainly composed of plagioclase feldspar (see Table 3–1), a solid solution consisting of two components. Anorthite ($CaAl_2Si_2O_8$) is dominant, while albite ($NaAlSi_3O_8$) constitutes only a few percent [88]. Both components are the principal source of aluminum in lunar regolith. Normative anorthite can be calculated considering that all of the Al_2O_3 presented in Table 3–2 belongs to anorthite. An average normative concentration of 68.4 wt.% of $CaAl_2Si_2O_8$ can be assumed for highlands regolith. Although normative anorthite is a good measure of the theoretical maximum amount of anorthite that can be present in lunar soils, the actual $CaAl_2Si_2O_8$ concentration might be inferior due to aluminum presence in glasses and agglutinates [89].

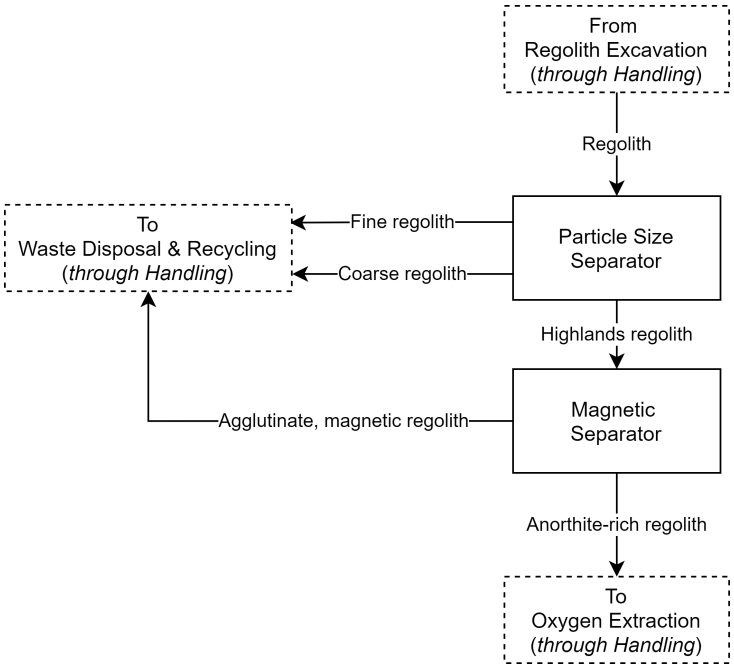

Fig. 4–4: Anorthite enrichment assembly. Schematic representation based on [77].

An anorthite enrichment assembly is represented in Figure 4–4. Based on the design proposed by Williams et al. [77], the assembly is composed of a gravitational particle size separator and a magnetic separator. The magnetic separator rejects the ferromagnetic agglutinates and the paramagnetic minerals, remaining the non-magnetic plagioclase ore. It must be noted that the ilmenite and anorthite enrichment assemblies are complementary. The tailings of the strong-field magnetic separator presented in Section 4.3.1 would be rich in plagioclase ore. The tailings of the magnetic separator of the anorthite assembly would be rich in minerals that contain FeO.

The assembly components are investigated in terms of mass, volume, power, and cooling requirements. Additional parts, such as feed bins or hoppers, used to transport the regolith between the separators, are considered part of the handling stage and are, therefore, neglected in this analysis. The assembly is sized to process 33.3 t/y of anorthite-rich regolith (90 wt.% of $CaAl_2Si_2O_8$). This processing rate produces 15 t/y of O_2 in a molten salt electrolysis assembly (see Appendix C). A conservative assumption

might consider an initial anorthite concentration of 50 wt.%, lower that the average normative concentration of 68.4 wt.% is considered. The 18.4 wt.% difference might be present in glasses and agglutinates.

The gravitational particle size separator of the anorthite enrichment assembly is assumed to be equal to the one of the ilmenite enrichment assembly. The medium particle fraction, between 20 µm and 200 µm, accounts for ∼35 wt.% of lunar regolith [82, 78]. Therefore, processing 185 t/y of excavated highlands regolith would return 65 t/y of medium-grained highlands regolith.

The magnetic separator of the anorthite enrichment assembly is assumed to be equal to the strong-field magnetic separator of the ilmenite enrichment assembly, which is based on the IMR model developed by Eagle Engineering, Inc. [11]. If a recovery efficiency of 93% is considered [77], 65 t/y of medium-grained highlands regolith could yield 33.3 t/y of anorthite-rich regolith (90 wt.% of $FeTiO_3$)

Table 4–3 summarizes the mass, volume, power, and cooling requirements of an anorthite enrichment assembly that processes 33.3 t/y of anorthite-rich regolith (90 wt.% of $CaAl_2Si_2O_8$). A duty cycle of 0.75 is assumed.

Tab. 4–3: Summary of the mass, volume, power, and cooling requirements of an anorthite enrichment assembly that processes 33.3 t/y of anorthite-rich regolith (90 wt.% of $CaAl_2Si_2O_8$).

Component	Mass (kg)	Volume (m^3)	Power (W)	Cooling (W)
Particle Size Separator	4	0.01	0	0
Magnetic Separator	29	0.03	717	0
Total	33	0.04	717	0

4.4 Oxygen Extraction

Over the last decades, numerous strategies for extracting oxygen from lunar regolith have been proposed [6]. From all these strategies, Monchieri et al. [90] and Schwandt et al. [48] identified the ISRU processes that would be most competitive economically and technically. One of these processes is the chemical reduction of iron oxides contained in lunar regolith, either by hydrogen, followed by the electrolysis of water (Section 4.4.1), or by methane, which additionally needs a further methane-reforming step [91]. Other possibilities are the carbothermal reduction of molten regolith, also requiring a subsequent methane-reforming step and water electrolysis [92], or the direct electrolysis of molten regolith (Section 4.4.2). Vapor phase pyrolysis is based on the vaporization of metal oxides, simultaneously reducing oxides and producing oxygen [93, 94]. The FFC-Cambridge process is another possibility to extract oxygen from lunar regolith by electrochemically reducing metal oxides in a molten salt electrolyte (Section 4.4.3).

Three of the processes mentioned above are analyzed in detail in this work: ilmenite reduction with hydrogen, molten regolith electrolysis, and molten salt electrolysis. As one of the goals of this thesis is to investigate ISRU processes that yield not only oxygen but also byproducts with adequate thermal properties for in-situ manufacturing of TCS radiators, vapor phase pyrolysis has been discarded as a possible oxygen extraction technique. When the metal oxides present in lunar regolith are vaporized, they dissociate into suboxides and O_2 [94]. Suboxides are characterized by a low thermal conductivity and are, therefore, not appropriate for TCS radiators. The regolith reduction with methane and the carbothermal reduction of molten regolith are conceptually similar to the ilmenite reduction with hydrogen. As methane is a more powerful reducing agent than hydrogen, it can reduce not only iron-containing ores but also the ones containing silicon, allowing the use of a wider regolith composition as feedstock [90]. However, the reduction of Si ores yields silicon and oxides as byproducts, which are also not desirable materials for a TCS radiator. Moreover, these processes require higher operating temperatures and are more complex than the ilmenite reduction with hydrogen due to the additional methane-reforming step required. For these reasons, they have not been analyzed in this thesis. However, controlling the feedstock composition entering the methane or carbothermal reduction reactor could potentially yield valuable byproducts while maintaining a high versatility of the oxygen extraction process. The analysis of these technologies might be included in the future to take into account the flexibility of the regolith composition compared to the restrictions of the ilmenite reduction with H_2.

4.4.1 Ilmenite Reduction with Hydrogen

The chemical reduction of regolith was one of the first proposed ISRU processes for oxygen production on the lunar surface [95]. In particular, H_2, in contrast with CH_4, is capable of reducing FeO-rich minerals at moderate temperatures without requiring a subsequent reforming step [48]. Abundant mare regolith minerals such as ilmenite ($FeTiO_3$) can be reduced using this process. During the last decade of the twentieth century, the first laboratory experiments were carried out using lunar samples and simulants [96, 97, 98]. More recently, work on hydrogen reduction has focused on analytical models [99, 24] and the development of experimental setups with higher TRLs [100, 101]. Within the scope of ESA's PROSPECT mission, an in-situ static hydrogen reduction demonstration instrument has been tested [102]. Moreover, the last In-Situ Resource Utilization Gap Assessment Report [23] disclosed that at least two different hydrogen reduction projects backed by NASA are currently active.

In the hydrogen reduction process, solid ilmenite-rich regolith is placed inside a reactor and heated up to temperatures near 1200 K [103]. During this process, solar wind-implanted volatiles might be degassed from the regolith and removed from the reactor before the H_2 gas stream comes into contact with the regolith. According to Equation 4–1, the endothermic reduction reaction produces water vapor and a mixture of solid iron and titanium dioxide. Additional oxides contained in the regolith do not react with hydrogen. After the reduction, Fe and TiO_2 are physically combined in former ilmenite grains [102]. Therefore, a direct recovery of metallic iron via magnetic separation is

not possible. Promising methods to separate iron from titanium dioxide are discussed in Section 4.5. Once separated, iron can be directly used or can be alloyed to manufacture steel components to support lunar surface exploration [85]. Fe produced from hydrogen reduction is one of the proposed material concepts in this thesis. TiO_2 might be further processed to recover titanium and oxygen via molten salt electrolysis [104] or directly used for specific space applications. For example, its high emissivity could allow the production of valuable surface finishes and coatings [105].

To favor the reaction kinetics, and enable efficient recovery of oxygen and metals, the beneficiated feedstock must have a high ilmenite grade. Gibson and Knudsen [81] reported desired $FeTiO_3$ concentrations between 80 and 90 wt.%, and Berggren and Zubrin [85] aimed for concentrations $>$70 wt.%. Moreover, FeO-rich minerals other than ilmenite can also be reduced [85]. This would be the case of the South Pole-Aitken Basin regolith near the surface reference mission location (see Chapter 3).

$$FeTiO_{3(s)} + H_{2(g)} \rightarrow Fe_{(s)} + TiO_{2(s)} + H_2O_{(g)} \tag{4–1}$$

$$H_2O_{(l)} \rightarrow H_{2(g)} + \frac{1}{2}O_{2(g)} \tag{4–2}$$

To sustain the reduction process, water vapor must be constantly removed from the gas phase of the reactor [103]. The gas phase does not only contain H_2O but also H_2 and toxic volatile components implanted in the regolith, such as NH_3, H_2S, or SO_2 [106]. As already discussed, it might be possible to remove most of the volatile components during the regolith heating phase, prior to the introduction of hydrogen into the reactor. The gaseous purification process would simplify accordingly. Moreover, during the thermochemical reduction, the gas stream might get loaded with hot particulate matter [106].

Figure 4–5 shows a schematic representation of an ilmenite reduction with hydrogen assembly based on the proposal made by Schlüter et al. [103]. After leaving the reactor, the gas passes through a filter and centrifugal collector unit, where the particulate matter is removed. Afterwards, the water purification unit condensates water, separating it from hydrogen and other volatiles. Hydrogen can be returned to the reactor, whereas liquid water serves as feedstock for an electrolyzer. The electrolyzer generates oxygen that can be used for life support or propellant production. Hydrogen produced from electrolysis is also returned to the reactor. Equations 4–1 and 4–2 show a stoichiometric H_2 closed-loop supply. If small losses occur during the process, additional H_2 might be supplied from the ECLSS water recycling.

Figure 2–2 proposed using the remaining hydrogen in a Sabatier reactor to produce methane. Instead, some of this hydrogen could be used to account for the H_2 losses of the ilmenite reduction process, reducing the annual production of methane. Kaschubek et al. [24] report an ideal SCRA hydrogen mass flow input of 1.13 kg/d produced from the ECLSS water recycling of 6 CMs. 15 t/y of oxygen production would stoichiometrically require 5.14 kg/d of H_2 if no hydrogen recirculation was considered. This would

mean that the hydrogen produced from the ECLSS water recycling could account for hydrogen losses up to 22%. Moreover, the reagent mass could also be recovered from solar wind-implanted hydrogen or lunar water ice [12]. For these reasons, hydrogen is not considered consumable and does not require a resupply from Earth.

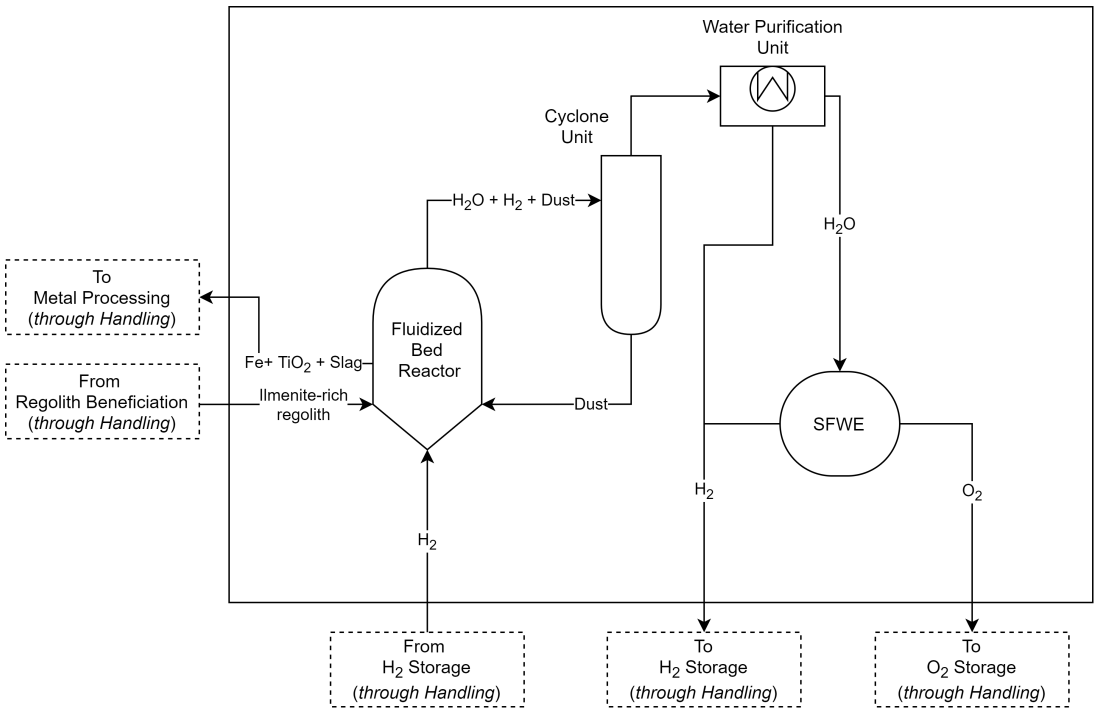

Fig. 4–5: Ilmenite reduction with hydrogen assembly. Schematic representation based on [103].

The components inside the large box in Figure 4–5 are considered part of the ilmenite reduction with hydrogen assembly and are investigated in terms of mass, volume, power, and cooling requirements. The dashed boxes are considered part of the handling stage, and are, therefore, neglected in this analysis.

A fluidized bed reactor has been proposed for the hydrogen reduction process [100, 101, 106]. Although a fluidized bed reactor concept is used in this thesis to define the overall ilmenite reduction with hydrogen assembly (see Figure 4–5), the fixed bed reactor model developed by Kaschubek et al. [24] is considered to dimension the reactor container, since a more suitable model has not been found in the literature. Moreover, the values returned by the fixed bed reactor are a more robust and reliable alternative for the early exploration stages of the lunar surface. A hollow Inconel cylinder with a wall thickness of 5 cm is conservatively assumed. The reactor is isolated with MLI layers to reduce the heat losses to the environment. To further decrease the heat losses, the container height equals the diameter, minimizing the container surface. Considering a $FeTiO_3$ content in the regolith of 80 wt.% and a conversion rate of 90%, Kaschubek et al. [24] report an optimized reactor temperature of 1000 K and 5.5 kW of available heating power for a water production rate of 9 kg/d. In this thesis, 61.6 kg/d of H_2O are required for an oxygen production rate of 15 t/y and a duty cycle of 0.75. The duty cycle is the amount of time per year that the reactor is in operation. As

discussed in Chapter 2, due to the location of the reference mission near POL regions, it is assumed that solar energy is available 75% of the year. A higher daily water production implies a larger reactor. Therefore, 11.15 kW of available heating power must be chosen to compensate for the higher heat losses to the environment. The available heating power accounts for the power to heat the regolith up to the reactor temperature, the heat losses to the lunar environment, and the power required to perform the reduction. Using the equations proposed in [24], the reactor dimensions, the batch mass, and conversion time can be estimated. The reactor inner diameter and height are 1.16 m. With the reactor dimensions, thickness, and an Inconel density of 8220 kg/m^3, a reactor mass and volume of 2834 kg and 1.57 m^3 are obtained, respectively. Each batch requires 59 h, including the preheating, reaction, and refill time, to reduce 1774 kg of ilmenite-rich regolith. To meet these requirements, 197.5 t/y of beneficiated regolith are necessary. The electric heater that provides the required 11.15 kW is scaled from the values provided in [11]. The volume of the heater equals one-sixth of the reactor volume. The heater mass depends on the thermal power by a factor of 5.6 kg/kW.

To remove the particulate matter, a cyclone separator as proposed in [106] is considered. As a simplification, the cyclone can be approximated to a hollow Inconel cylinder followed by a cone. Following the dimensioning approach proposed by de Paula et al. [107], the cyclone diameter depends on the volumetric flow inlet and the project constant R, which is 1.90556 m/s for a Lapple cyclone. The cylinder height equals two times the diameter and the total height four times the diameter.

$$\dot{V} = \frac{\dot{m}_{H_20} \cdot \bar{R}_{H_20} \cdot T_{reactor}}{\tau \cdot p_{H_20}} \tag{4–3}$$

$$D = \sqrt{\frac{\dot{V}}{R}} \tag{4–4}$$

For the required annual O_2 production, 16.875 t/y of H_2O must be generated. The ideal gas law allows the calculation of the volumetric flow (Equation 4–3). $\dot{V}$ is the volumetric flow entering the cyclone, $\dot{m}_{H_2O}$ the annual water production, $\bar{R}_{H_2O}$ the specific water constant, $T_{reactor}$ the operating temperature, τ the duty cycle, and p_{H_2O} the partial pressure of water vapor. A total operating pressure of 1 bar [96] and a maximum vapor partial pressure of 10% [102] are considered. The volumetric flow can be input in Equation 4–4, returning a cyclone diameter of 13.14 cm. The height of the cyclone is, therefore, 52.56 cm. The cyclone thickness is conservatively assumed to be 1 cm. With the cyclone dimensions, the thickness, and the Inconel density, the cyclone mass and volume are 16.75 kg and 0.0068 m^3, respectively.

Multiple cyclones and HEPA filters might be placed in series to increase the particle removal efficiency [106]. For this analysis, the concept proposed by Mantovani et al. [108] has been followed. The reactor exhaust gas passes through a double cyclone array with HEPA filters at the exit of each cyclone. As a simplification, the mass and volume of the HEPA filters are neglected.

The requirements of a purification unit for an ISRU water recovery system might differ from those of an ECLSS. Since the ISS WPA [109] has been designed to treat different substances than those present in ISRU water, using it as a reference for a purification unit might be questionable. For example, its catalytic reactor oxides organic compounds that are not be present in ISRU water. The WPA multi-filtration and ion-exchange beds might also not be suitable for the type of ions contained in ISRU water. Schlüter et al. [106] and Holquist et al. [110] propose cold trap concepts to separate water from the gas stream, removing H_2 and other volatiles. Moreover, before the electrolysis, water needs to be deionized. Ion-exchange membranes and electrodialysis are proposed in the literature [111, 110, 106] as possible deionization technologies.

A complete water purification unit schematic is presented in [112]. However, estimating the mass and volume of individual components is challenging due to the low TRL of the design. The Condensing Heat Exchanger (CHX) is expected to be the principal mass driver of the system. Thus, for this analysis, the water purification unit is assumed to be a CHX that cools down the gas stream to an environment temperature of 293 K, allowing water to condensate while hydrogen and unwanted volatiles flow out the unit. The expected cooling power is 9.67 kW, including the power required to cool down the hydrogen and water stream to the boiling point of H_2O, the enthalpy of vaporization of water, and the power to cool down liquid water to 293 K.

The mass and volume requirements are obtained from the Life Support Trade-Off Tool (LiSTOT) [113, 114, 115] developed at the Technical University of Munich. The CHX mass and volume are 705 kg and 5.57 m^3, respectively. In the future, additional purification components shall be incorporated into the analysis.

For the electrolysis, a Static Feed Water Electrolyzer (SFWE), as proposed by Holquist et al. [110], is chosen. Equation 4–5 is used to estimate the electrolysis power, where $\dot{m}_{H_2O}$ is the annual water production, τ the duty cycle, and M_{W,H_2O} the molecular weight of water. An overall electrolysis efficiency ($\eta_{electrolysis}$) of 0.8 is assumed. ΔG_{H_2O} defines the Gibbs free energy of H_2O, which is 237 kJ/mol.

$$P_{electrolysis} = \frac{\dot{m}_{H_20}}{\tau \cdot M_{W,H_2O} \cdot \eta_{electrolysis}} \cdot \Delta G_{H_2O} \tag{4–5}$$

$P_{electrolysis}$ is 11.75 kW. 9.4 kW contribute to the separation of water in hydrogen and oxygen, whereas 2.35 kW are released in form of heat. Due to the endothermic nature of the electrolysis, 1.95 kW are required to sustain the chemical reaction (Equation 4–6). Therefore, the remaining 400 W must be cooled. $\Delta H_{f,\,H_2O}$ defines the enthalpy of formation of H_2O, which is 286 kJ/mol.

$$\dot{Q}_{endothermic} = \frac{\dot{m}_{H_20}}{\tau \cdot M_{W,H_2O}} \cdot (\Delta H_{f,H_2O} - \Delta G_{H_2O}) \tag{4–6}$$

Based on the electrolysis power, the mass and volume of the SFWE are estimated using LiSTOT [113]. Its mass and volume are 875 kg and 1.22 m^3, respectively.

Infrastructure that connects the different components of the hydrogen reduction assembly, such as pipes, valves, pumps, dyers, or structural parts, is not considered in this analysis.

Table 4–4 presents the mass, volume, power, and cooling requirements for an annual oxygen production of 15 t and a duty cycle of 0.75. Eagle Engineering, Inc. [11] also carried out a similar study in 1988 for a lunar oxygen pilot plant that would produce 2 t/m of O_2. Although in both analyses, the reactor is the main mass driver of the hydrogen reduction assembly, the kinetics model proposed by Kaschubek et al. [24] is a significant improvement to determine the reactor dimensions and the conversion time. However, the considered wall thickness of 5 cm might be overdimensioned. A detailed investigation of the necessary Inconel thickness shall considerably decrease the reactor mass. Eagle's study [11] directly introduced the high-temperature exhaust gas stream into the electrolyzer instead of separating water and hydrogen via a CHX before the electrolysis. If compared, both approaches have a similar power demand. However, condensing water shall enable the separation of additional volatiles that might affect the performance of the SFWE. Moreover, the mass and volume estimates of the TCS and the electrolyzer presented in [11] are significantly lower than the values obtained from LiSTOT [113]. The values obtained from LiSTOT [113] are scaled from actual subsystems and not based on analytical sizing models.

Tab. 4–4: Summary of the mass, volume, power, and cooling requirements of a hydrogen reduction assembly for an annual oxygen production of 15 t and a duty cycle of 0.75.

Component	Mass (kg)	Volume (m^3)	Power (W)	Cooling (W)
H_2 Reduction Reactor	2896	1.83	11150	0
Cyclone Unit	34	0.01	0	0
Water Purification Unit	705	5.57	0	9670
SFPW	875	1.22	11750	400
Total	4510	8.63	22900	10070

4.4.2 Molten Regolith Electrolysis

Molten Regolith Electrolysis (MRE) was already proposed in the 1960s as a potential process to extract oxygen from lunar regolith [95]. During the last decades of the twentieth century, the first laboratory experiments were carried out using lunar simulants [116, 117]. More recently, work on MRE has continued at the Marshall Space Flight Center [118], the Ohio State University [119], and the Kennedy Space Center [120, 121, 122] in conjunction with the MIT [123, 124, 125, 17, 18]. Moreover, the last In-Situ Resource Utilization Gap Assessment Report [23] disclosed that at least three different molten regolith electrolysis projects backed by NASA are currently under development.

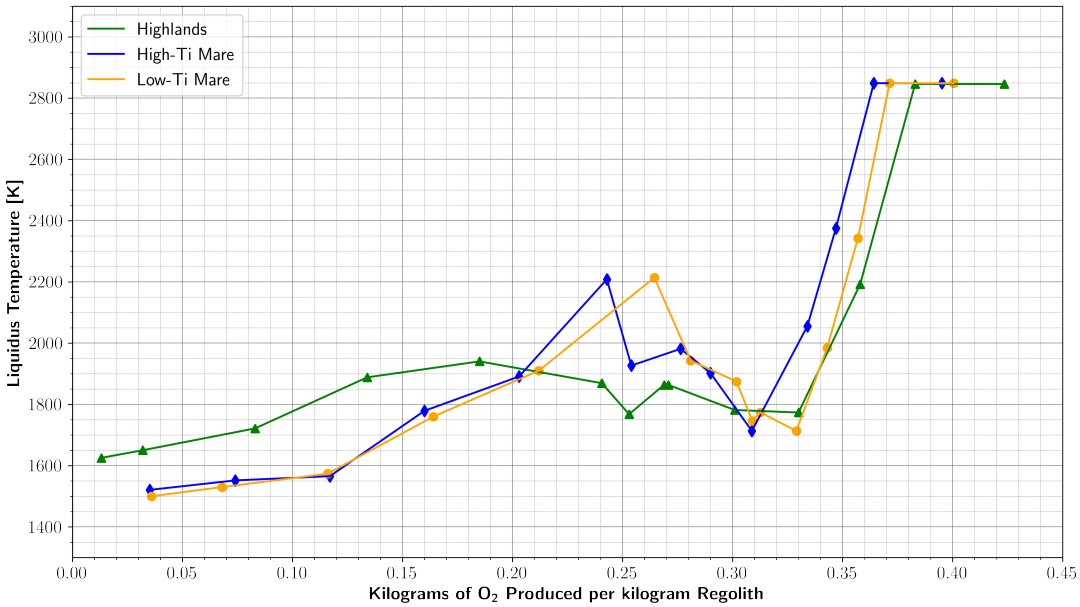

Fig. 4–6: Liquidus temperature of lunar regolith along the MRE process. Adapted from [17] for the regolith compositions presented in Table 3–2.

In the MRE process, regolith is fed into an electrolytic cell and heated to a molten state. Voltage is applied between two electrodes which are immersed in the molten regolith. The electrical conductivity of molten regolith is high enough to drive a current and sustain the electrolysis of the oxides. Oxygen gas is generated at an inert anode, whereas at the cathode, molten metals, such as iron, silicon, titanium, or aluminum, are produced. [18]

The main advantage of molten regolith electrolysis compared to the ilmenite reduction with hydrogen described in Section 4.4.1 is the possibility of using unbeneficiated regolith as feedstock for the process.

The order in which oxides are reduced depends on their stability. Schreiner [17] suggested an oxide electrolysis order based on their increasingly negative Gibbs free energies. FeO would be initially reduced, followed by SiO_2, MgO, TiO_2, Al_2O_3, and CaO. Although this assumption might be valid when oxide species are abundant, if the concentration of a species is too low, the oxide will no longer be preferentially reduced in favor of more abundant species. Due to the oxide reduction, the regolith composition varies during the electrolysis process, modifying the melting temperature and electrical conductivity of the mixture. Therefore, if the operating temperature of the electrolytic cell and the applied potential between the electrodes are controlled, MRE might allow the direct recovery of specific metals. A previous beneficiation step to control the feedstock composition could assist the metal recovery step.

Figure 4–6 represents how the regolith melting temperature varies as the electrolysis progresses. The values have been adapted from [17] for the regolith compositions presented in Table 3–2, assuming that only 95 wt.% of each oxide can be reduced. As the operating temperature increases, the reactor can reduce more oxides and extract

more oxygen and metals per unit of regolith. If the reactor design allows it, the oxygen yield can be as high as 0.4 kg of O_2 per kilogram of regolith.

Since the reference mission is located in the lunar South Pole, highlands regolith is the most likely available feedstock at the excavation site (see Chapter 3). Figure 4–7 presents the oxide reduction and O_2 yield for highlands regolith along the MRE process. The regolith melting temperature that reduces FeO is near 1650 K. If the operating temperature of the reactor was set to this level, iron could be directly extracted from the MRE. However, to allow an easy extraction process, metallic iron shall preferably be in a molten state. That would imply having a reactor temperature higher than 1800 K. In this case, not only the iron oxides but also SiO_2 would be reduced, enabling the recovery of Fe-Si alloys. For this reason, Fe-Si alloys produced from molten regolith electrolysis are one of the proposed material concepts in this thesis. Once the metals are recovered, the reactor temperature can rise to continue reducing the remaining molten oxides for a higher oxygen gain.

Existing MRE reactor designs aimed for operating temperatures near 1900 K [120, 123, 125], where reasonable amounts of oxygen could be extracted while yielding a valuable mixture of molten metals. If the temperature increases to 2000 K, an oxygen yield of 0.34 kg of O_2 per kilogram of regolith might be reachable for highlands regolith, producing a mixture of iron, silicon, titanium, and aluminum. The reduced products of MgO and other less abundant oxides such as Na_2O, P_2O_5, or K_2O might join the gaseous O_2 stream due to their lower boiling points [18]. For mare regolith, the oxygen yield might be lower than 0.23 kg of O_2 per kilogram of regolith if the operating temperature is not higher than 2000 K, recovering only iron and silicon as molten metals. It must be noted that highlands regolith typically contains low amounts of FeO. This fact would imply that highlands regolith might require a previous beneficiation step if the MRE process wants to favor the extraction of large quantities of Fe-Si alloys. Nevertheless, its composition has an average melting temperature lower than mare regolith and, therefore, allows a higher oxygen extraction yield for the same reactor temperature.

Molten regolith has an intrinsic corrosive nature that affects the durability of the electrodes and degrades the reactor walls. To protect the reactor walls from the corrosive effect of molten regolith, a Joule-heated electrolysis reactor concept has been proposed [122]. The reactor center is heated via Joule effect, maintaining the core material molten while the thermal gradients generate a separating layer of solid regolith between the reactor walls and the molten core. Handling concepts have been developed to additionally deal with the extraction of molten metals from the electrolytic cell [119]. Research has also focused on the development of electrode materials capable of sustaining operation for long periods of time. Anode materials must have a melting point above the operating temperature of the electrolytic cell, withstand the corrosion of molten regolith, display high electrical conductivity, and be resistant to high-temperature oxidation [120]. If these criteria are not met, they would require frequent replacements, which might end up in a prohibitive consumable mass. Suitable anode materials might include iridium, platinum, and rhodium [126, 127, 128], Ir-W alloys [124], or Fe-Cr alloys [129]. Cathode materials have similar requirements to anode materials regarding the melting point, electrical conductivity, and corrosion resistance.

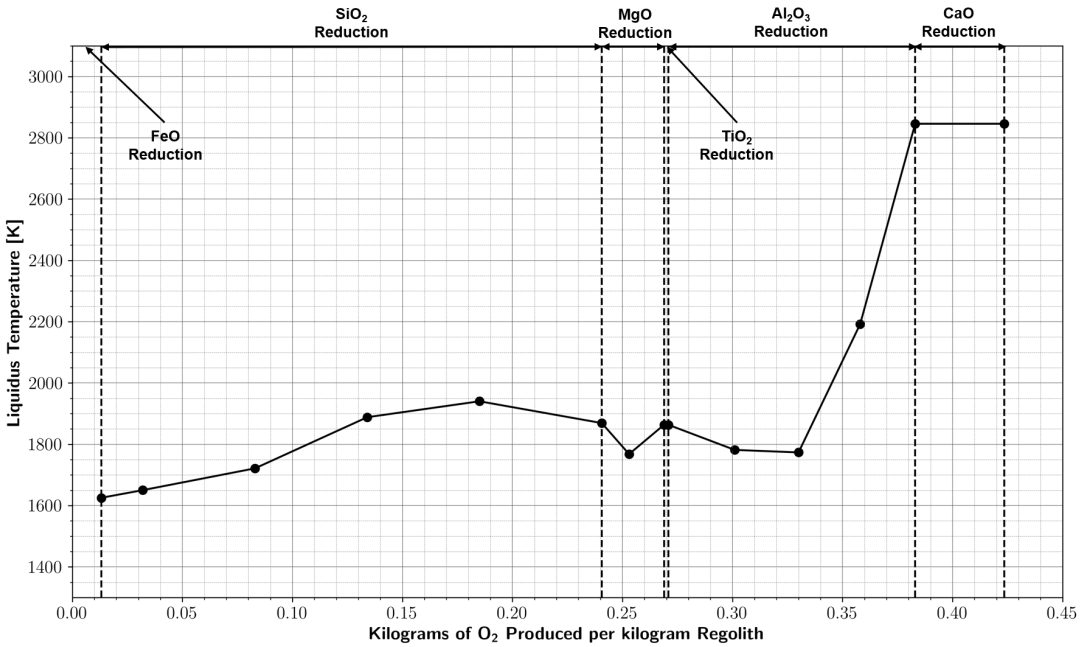

Fig. 4–7: Liquidus temperature of highlands regolith along the MRE process. Adapted from [17] for the regolith compositions presented in Table 3–2.

However, they must additionally avoid forming alloys with the reduced molten metals [120]. Historically, cathode materials have been less investigated than anode materials. Traditionally, molybdenum has been used for small-scale laboratory experiments [128, 124, 129]. However, using Mo does not prevent the molten iron produced in the reactor from alloying with the cathode current collector [17]. Paramore [127] proposed a molten copper pool to overcome this problem.

Figure 4–8 shows a schematic representation of an MRE assembly based on the proposal made by Schlüter et al. [103]. Regolith is introduced into the MRE reactor and heated up to a molten state. During the process, solar wind-implanted volatiles might be degassed from the regolith and removed from the reactor before the electrolysis starts. Metals can be recovered from the cathode while oxygen anions oxidize to gaseous O_2 at the inert anode.

Due to the high operating temperatures, the gas stream exhausting the reactor is composed of oxygen, non-removed solar wind-implanted volatiles, and light elements and oxides that are vaporized during the process. Moreover, the gas stream might come into contact with the separating layer of solid regolith between the reactor walls and the molten core, loading it with hot particulate matter. The oxygen purification unit is in charge of removing all these impurities from O_2.

The components inside the large box in Figure 4–8 are considered part of the molten regolith electrolysis assembly and are investigated in terms of mass, volume, power, and cooling requirements. A heat exchanger is included to reduce the temperature of the oxygen stream before its storage. It allows a better comparison between the ilmenite reduction with H_2 and the MRE due to the fact that the hydrogen reduction

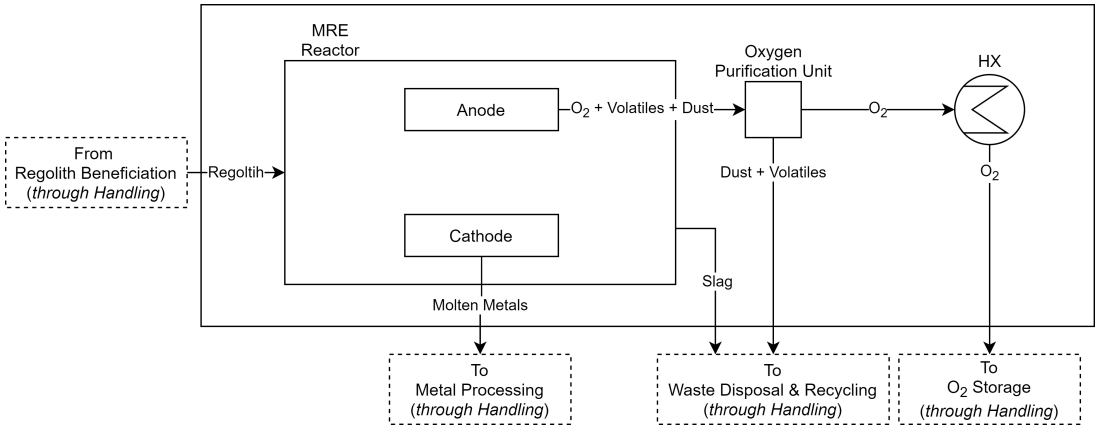

Fig. 4–8: Molten regolith electrolysis assembly. Schematic representation based on [103].

process has to obligatorily cool down the extracted water vapor to perform the electrolysis. The dashed boxes are considered part of the handling stage, and are, therefore, neglected in this analysis.

The parametric model developed by Schreiner [17, 18] is used to represent the reactor of the MRE assembly. This work modeled a Joule-heated MRE reactor using coupled electrochemical and thermodynamic simulations that included regolith material property models as input to analyze the performance of the ISRU facility. Furthermore, Schreiner [17] performed an integrated ISRU system optimization, including the excavation and feeding systems, the MRE reactor, a YSZ separator, the liquid oxygen storage infrastructure, and a power plant.

For highlands regolith feedstock, the optimized model reports a preference for a single larger reactor rather than multiple smaller ones. The reactor geometry is modeled as a hollow cylinder. The internal diameter of the cylinder increases with the annual oxygen production as shown in Equation 4–7. The equation has been obtained fitting a curve to the plots provided by Schreiner [17] and taking into consideration the effect of the duty cycle. The values between brackets represent the 95% confidence bounds.

$$D_{reactor} \approx 0.235[\pm 0.028] \cdot \left(\frac{N}{2\tau}\right)^{0.293[\pm 0.014]} \tag{4–7}$$

$D_{reactor}$ is the internal diameter of the reactor in m, N the oxygen production in kg/y, and τ the duty cycle. For the annual oxygen production of 15 t defined in Chapter 2, the required diameter would be 3.49 m. A duty cycle of 0.75 is chosen due to the location of the reference mission near POL regions. Schreiner [17], however, considered a duty cycle of 0.5 for his optimization. The internal height of the reactor equals 1.5 times the maximum electrode separation. The electrodes are circular plates placed parallel to the cylinder bases. Independently from the oxygen production rate, the optimal separation of the electrodes is 2 cm. The electrode separation fixes the inner reactor height to 3 cm. The total volume of the MRE reactor could be calculated if the internal reactor dimensions and the structural, insulation, and refractory thicknesses were known.

However, Schreiner [17] does not report the resultant thicknesses of the optimized design. In the model, the wall thickness is calculated as follows: a minimum wall thickness of 2 cm is initially set, and MLI layers are subsequently added in an attempt to meet the insulation requirements coming from the thermodynamics simulations. If this fails, the wall thickness is increased to reach the required thermal resistance. Without access to the thermodynamic model, estimating the actual wall thicknesses of each component is burdensome. For this reason, a wall thickness of 2 cm is assumed, for which the reactor volume is 0.69 m^3.

The mass of the reactor also scales with the oxygen production following Equation 4–8. Equation 4–8 is adapted from [17].

$$M_{reactor} \approx 1.492[\pm 0.33] \cdot \left(\frac{N}{2\tau}\right)^{0.608[\pm 0.0254]} \tag{4–8}$$

$M_{reactor}$ is the reactor mass in kg, including the structural, refractory, and insulation layers, as well as the preheater; N is the oxygen production in kg/y, and τ the duty cycle. For an annual oxygen production of 15 t and a duty cycle of 0.75, the reactor mass would be 403 kg.

The reactor power accounts for the necessary power to heat the regolith to the operating temperature, the latent heat of the phase change, the radiative heat losses to the lunar environment, and the power required to perform the electrolysis, in terms of breaking the chemical bonds of the oxides and maintaining thermal equilibrium throughout the endothermic reaction. This power scales with the oxygen production as shown in Equation 4–9. Equation 4–9 is adapted from [17].

$$P_{reactor} \approx 264[\pm 9] \cdot \left(\frac{N}{2\tau}\right)^{0.577[\pm 0.004]} \tag{4–9}$$

$P_{reactor}$ is the total MRE power in W, N the oxygen production in kg/y, and τ the duty cycle. For an annual oxygen production of 15 t and a duty cycle of 0.75, the required power would be 53.4 kW.

This annual oxygen production requires a considerably higher operating temperature (2254 K) compared to the aimed 1900 K of previous works [120, 123, 125]. The operating temperature for 15 t of O_2 per year has also been extrapolated from the plots provided by Schreiner [17] following Equation 4–10.

$$T_{reactor} \approx 1140[\pm 27] \cdot \left(\frac{N}{2\tau}\right)^{0.074[\pm 0.0028]} \tag{4–10}$$

$T_{reactor}$ is the operating temperature of the MRE reactor in K, N the oxygen production in kg/y, and τ the duty cycle. For this operating temperature of 2254 K, and including a safety factor of 50 K between the operating temperature and the liquidus temperature of regolith as considered in [17], the oxygen yield is 0.36 kg of O_2 per kilogram of

highlands regolith (see Figure 4–7). This oxygen yield would require the excavation of at least 41.7 t of highlands regolith per year.

When, instead of the oxygen production, the metal recovery throughput has to be optimized using the same MRE assembly dimensions, the operating temperature can be adjusted to extract valuable Fe-Si alloys. In this case, the power requirements would decrease as the regolith has to be heated to lower temperatures.

Following the same procedure of fitting a curve to the plots provided by Schreiner [17], the equations for the anode and cathode masses can be obtained. For an annual oxygen production of 15 t and a duty cycle of 0.75, the anode and cathode masses are 22.9 kg and 16.5 kg, respectively. As the chosen electrodes are iridium for the anode and molybdenum for the cathode, the required volume can be estimated from the component masses and material densities, requiring the anode and cathode 0.001 m^3 and 0.0016 m^3, respectively. A loss rate of 8 mm/y has been considered for the iridium anode [125]. This loss rate conservatively requires six replacements per year if the anode is replaced when 50% of the iridium has been consumed. An identical replacement rate has been chosen for the molybdenum cathode.

In contrast to the ilmenite reduction with hydrogen, HEPA filters might be enough to remove the particulate matter from the exhaust gas. Most of the regolith inside the reactor is in a viscous molten state except for a protecting layer of solid regolith between the core and the reactor walls. Therefore, the amount of dust through which the oxygen has to flow is low. Moreover, although, in the hydrogen reduction process, a rapid removal of the gas stream is encouraged to favor the reaction kinetics; in the MRE process, the removal rates and exhaust velocities can be kept low, decreasing the turbulence and, therefore, reducing the amount of particulate matter content suspended in the gas stream. After the particle filter, Schlüter et al. [106] propose using cryogenic distillation prior to the storage of O_2 in a liquid state to remove the volatiles and vaporized components from the gas stream. With identical intentions, the Yttria-Stabilized Zirconia (YSZ) separator model proposed by Schreiner [17] has been considered as the main component of the oxygen purification unit. The same procedure of fitting a curve to the plots provided by Schreiner [17] has been followed. For an annual oxygen production of 15 t and a duty cycle of 0.75, the YSZ separator mass is 30 kg, the volume 0.005 m^3, and the required power 0.82 kW. It must be noted that the mass and volume models are an oversimplification of an actual YSZ separator design [17]. More realistic mass and volume models shall be created in the future. Similar to the ilmenite reduction with hydrogen, the mass and volume of the HEPA filter and any additional purification components are neglected in this analysis.

The cooling power is the power required to bring the oxygen stream from the operating temperature to an environment temperature (T_{env}) of 293 K. It has been estimated using Equation 4–11.

$$\dot{Q}_{cooling} = \frac{M_{batch} \cdot \lambda_{O_2} \cdot \int_{T_{reactor}}^{T_{env}} C_{p,O_2}(T) dT}{t_{batch}} \tag{4–11}$$

$\dot{Q}_{cooling}$ is the cooling power, $T_{reactor}$ the operating temperature of the MRE reactor, C_{p,O_2} the specific heat at constant pressure of O_2, and λ_{O_2} the oxygen yield for a given reactor temperature. M_{batch} and t_{batch} are the optimal batch mass and time of the MRE reactor. Schreiner [17] reports values of 152 kg and 24 h, respectively, for an oxygen production rate of 15 t/y and a duty cycle of 0.75. For this rate, the required cooling power is 1.36 kW. The mass and volume requirements of the heat exchanger have been obtained using LiSTOT [113]. LiSTOT [113] only possesses sizing information for CHXs, since they are the most common type of heat exchanger for space applications. They are typically used in ECLSS to remove the cabin heat and control the relative humidity. Although they might be slightly heavier than normal HXs, a CHX with a mass of 100 kg and a volume of 0.79 m^3 that rejects 1.36 kW has been considered for this analysis.

Infrastructure that connects the different components of the MRE assembly, such as pipes, valves, pumps, or structural parts, is not considered in this analysis.

Tab. 4–5: Summary of the mass, volume, power, and cooling requirements of an MRE assembly for an annual oxygen production of 15 t and a duty cycle of 0.75.

	Non-consumables				Consumables	
Component	**Mass (kg)**	**Volume (m^3)**	**Power (W)**	**Cooling (W)**	**Mass (kg/y)**	**Volume (m^3/y)**
MRE Reactor	403	0.69	53400	0	0	0
Anode	0	0	0	0	137.4	0.006
Cathode	0	0	0	0	99.0	0.010
Oxygen Purification Unit	30	0.005	820	0	0	0
Heat Exchanger	100	0.79	0	1360	0	0
Total	533	1.49	54220	1360	226.4	0.016

Table 4–5 presents the mass, volume, power, and cooling requirements for an annual oxygen production of 15 t and a duty cycle of 0.75. As expected, the MRE reactor is the main ISRU driver. Due to the high operating temperature, the amount of O_2 cooling power required is significant. Schreiner [17] models the mass and power of a liquefaction system that cools down the O_2 stream. For an oxygen production of 15 t/y and a duty cycle of 0.75, the system mass, which includes not only a condensing heat exchanger to liquefy O_2 but also the storage tank, is around 500 kg. Although the modeling approach of the liquefaction system is not reported in [17], the order of magnitude of the components is similar. A TCS that releases all the waste heat generated during the complete ISRU process chain is also modeled in [11]. The TCS is modeled as a radiator and has a mass of 1362 kg for a heat rejection of 24.4 kW. Although the modeling approach that defines the TCS mass (in kg) as 20 times the required radiator surface area (in m^2) is questionable, the differences between the CHX in LiSTOT [113] and the values reported in [11] are reasonable. The oxygen purification unit, which accounts for $>$5% of the total mass, is expected to play a relevant role in

the MRE assembly design. For this reason, a more accurate oxygen purification model shall be developed in the future. Moreover, the electrode masses correspond to more than 7% of the total mass. Therefore, the replacement rate is expected to be a driving factor that would determine the feasibility of the MRE process.

4.4.3 Molten Salt Electrolysis

From the three oxygen extraction methods discussed in this work, Molten Salt Electrolysis (MSE), also known as the FFC-Cambridge process, is the ISRU technology with the lowest TRL. In the context of O_2 extraction from lunar regolith, only laboratory studies have been published [48, 130] based on the process proposed by Fray, Farthing, and Chen at the beginning of the twenty-first century [131, 132]. Other authors have focused on alternative electrochemical methods to reduce regolith oxides [133, 134]. However, MSE has been developed during the last decade for terrestrial applications [135, 136] and has enabled the implementation of end-to-end commercial processes to produce titanium powders and alloys [104]. Moreover, the last In-Situ Resource Utilization Gap Assessment Report [23] disclosed that ESA is currently supporting the development of MSE demonstrators to increase its technological maturity.

In the MSE process, regolith oxides, either sintered [48] or powdered [130], are submerged in a bath of molten calcium chloride ($CaCl_2$) mixed with a low content of CaO at around 1200 K.

Voltage is applied between the regolith (cathode) and an inert anode. $CaCl_2$ acts as the electrolyte and allows sustainable electrolysis of the oxides. Oxygen gas is generated at the anode, whereas the cathode is gradually reduced to form a mixture of metals and alloys. [48]

The main advantage of MSE compared to the ilmenite reduction with hydrogen is that it can theoretically reduce all lunar minerals and oxides, allowing the use of unbeneficiated regolith as feedstock for the process. Although molten regolith electrolysis can also reduce all regolith oxides, the operating temperatures ($>$1900 K) at which the electrolysis occurs are significantly higher than for MSE. [130]

The latest laboratory experiments carried out with regolith simulants reported a 96% oxygen removal from the cathode [130]. Lomax et al. [130] state that with the appropriate process modifications, a close to 100% oxygen recovery from lunar regolith could be achieved using the FFC-Cambridge process. Depending on the regolith type, this could imply an oxygen yield higher than 0.4 kg of O_2 per kilogram of regolith. The tests were performed using JSC-2A lunar regolith simulant. JSC-2A lunar regolith simulant is a replica of the previous simulant version JSC-1A [137]. In this case, three principal alloys dominated the metallic byproduct: an Al-Fe alloy, usually including Si; a Ca-Si-Al alloy, sometimes with the inclusion of Mg; and a Fe-Si alloy that regularly contained Ti and Al [130]. A previous beneficiation step to control the feedstock composition could assist the recovery of specific metals or alloys. For instance, in terrestrial applications, pure titanium and alloy powders can be gained from the MSE reduction of rutile [104]. If regolith was beneficiated to create a feedstock with high anorthite ($CaAl_2Si_2O_8$) content, Ca-Si-Al alloys might be directly recoverable. These metallic al-

loys could be potentially processed to deplete Ca and allow the further separation of aluminum and silicon (see Section 4.5). Al is a valuable metal for ISRU applications due to its lightweight structural properties. Moreover, it possesses favorable electrical and thermal properties. Silicon could also serve as raw material for photovoltaic cells [48]. For these reasons, two material concepts are considered in this thesis: a heterogeneous metal mixture produced from the MSE reduction of highlands regolith without further processing, and aluminum obtained after the reduction of anorthite-rich feedstock and its separation from calcium and silicon.

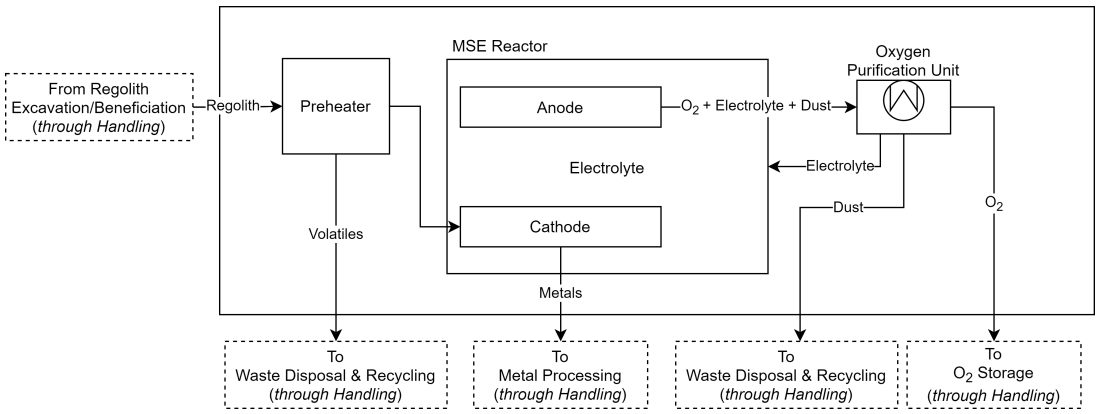

Fig. 4–9: Molten salt electrolysis assembly. Schematic representation based on [103].

Figure 4–9 shows a schematic representation of a molten salt electrolysis assembly based on the proposal made by Schlüter et al. [103]. The cathode is filled with regolith powder and introduced in an electrolyte bath. The temperature of the electrolytic cell rises to 1223 K. During this process, solar wind-implanted volatiles might be degassed from regolith and mixed with the molten salt. To prevent the contamination of the electrolyte, regolith must be preheated and degassed before entering the reactor [20]. Under extremely low pressures, $CaCl_2$ would vaporize at the suggested operating temperatures. To avoid the use of an inert gas that pressurizes the reactor, the FFC-Cambridge electrolyte is proposed to work in equilibrium between its gas and liquid phase. Direct lunar vacuum exposure of the molten salt must be prevented to avoid losing electrolyte mass. This could be achieved by solidifying the electrolyte during the regolith insertion and extraction operations [20].

Analog to MRE, the development of suitable inert anode materials capable of sustaining operation for long periods of time is challenging. The anode materials that have been proposed in the literature for $CaCl_2$ melts are doped SnO_2 [138], and calcium titanate or calcium ruthenate mixtures [139, 140].

An oxygen purification unit is necessary to separate oxygen from particulate matter, electrolyte vapor, and other volatiles present in the gas stream. A HEPA filter shall capture regolith particles exhausting the reactor. Schlüter et al. [106] propose the condensation or adsorption of the salt at still elevated temperatures ($>$850 K), recirculating it back into the reactor and minimizing electrolyte losses. It would enable a quasi-closed-loop operation, increasing the overall sustainability of the process. Other volatile components produced during the electrolysis, such as light elements contained

in the reduced regolith, could be distilled before liquefying oxygen for cryogenic storage [106] or removed by a YSZ separator [17].

The components inside the large box in Figure 4–9 are considered part of the molten salt electrolysis assembly and are investigated in terms of mass, volume, power, and cooling requirements. A heat exchanger is included to reduce the temperature of the oxygen stream before its storage. Similar to the MRE case, this allows a better comparison with the ilmenite reduction with H_2. The dashed boxes are considered part of the handling stage, and are, therefore, neglected in this analysis.

Due to the low TRL of the FFC-Cambridge process in the ISRU field, currently, no parametric reactor model is available in the literature. This section describes a simplified sizing model for an MRE assembly that produces 15 t/y of O_2 with a duty cycle of 0.75.

First, the preheater dimensions must be known. The preheater unit is composed of a container and an electric heater. The container is a hollow Inconel cylinder with a wall thickness of 2 cm and isolated with MLI layers to reduce the heat losses to the environment. To further decrease the heat losses, the container height equals the diameter, minimizing the container surface. The electric heater is scaled from the values provided in [11]. The volume of the heater equals one-sixth of the container volume. The heater mass depends on the required power ($P_{preheater}$) by a factor of 5.6 kg/kW.

$$D_{preheater} = \sqrt[3]{\frac{4 \cdot M_{batch}}{\pi \cdot \rho_{Regolith}}} \tag{4–12}$$

Equation 4–12 defines the preheater diameter ($D_{preheater}$). The regolith density ($\rho_{Regolith}$) is equal to 1500 kg/m^3 [59], and the regolith mass per reactor batch (M_{batch}) can be calculated using Equation 4–13.

$$M_{batch} = \frac{N}{\lambda_{O_2} \cdot n_{batch}} \tag{4–13}$$

N is the annual O_2 production, λ_{O_2} the oxygen yield, and n_{batch} the number of batches in a year. Lomax et al. [130] report a possible oxygen recovery of close to 100%. For highlands regolith, an oxygen yield of 0.44 is assumed. For this oxygen yield, 0.6 wt.% O_2 remains in the metallic byproduct (see Table 3–3). To produce 15 t of oxygen per year, an excavation rate of 34 t/y of highlands regolith would be required.

The number of batches in a year is defined by Equation 4–14.

$$n_{batch} = \frac{t_{operation}}{t_{batch}} \tag{4–14}$$

In this equation, $t_{operation}$ is the cumulative operating time for the reactor adjusted by duty cycle and t_{batch} total batch time, including the electrolysis and the downtime between batches. To completely reduce the regolith oxides, an electrolysis time of 45h

is considered [130]. The downtime accounts for the required time to insert and extract the preheated regolith basket. As discussed above, if instead of using an inert gas to pressurize the reactor, the electrolyte has to be melted and solidified during the insertion and extraction process, the downtime must also account for these operations. In this analysis, the downtime is considered 30 min.

$$t_{batch} = t_{electrolsys} + t_{downtime} \tag{4–15}$$

To avoid the contamination of the electrolyte during the regolith volatile degassing, the preheater container and the MSE reactor are independent units. Therefore, the preheating and the electrolysis can be carried out in parallel for subsequent batches. Equation 4–16 calculates the preheating power ($P_{preheater}$).

$$P_{preheat} = M_{batch} \cdot \frac{\int_{T_{env}}^{T_{reactor}} C_{p,Regolith}(T)dT}{t_{electrolysis}} + \dot{Q}_{loss} \tag{4–16}$$

The regolith is heated from an environment temperature (T_{env}) of 293 K to the operating temperature ($T_{reactor}$) of 1223 K. The temperature dependency of the specific heat ($C_{p,Regolith}$) is obtained from [59]. $\dot{Q}_{loss}$ are heat losses to the environment.

Equations 4–17 to 4–19 are solved iteratively for $\dot{Q}_{loss}$, $T_{MLI_{in}}$, and $T_{MLI_{out}}$, where $T_{MLI_{in}}$ and $T_{MLI_{out}}$ are the internal and external layer temperatures of the MLI insulation, as shown in Figure 4–10. As a simplification, one-dimensional flat plate and cylindrical wall conduction through the Inconel shell are considered. The MLI insulation is modeled as radiative heat transfer from the inner to the outer layer using an effective emissivity. It is assumed that half of the outer MLI cover radiates heat towards the regolith surface and the other half towards the outer space. The mass and thickness of the MLI layers are neglected in this analysis.

$$\dot{Q}_{loss} = k_{Inconel} \cdot \pi \cdot \left(\frac{D_{preheater}^2}{2 \cdot d_{Inconel}} + 2 \cdot \frac{D_{preheater} + 2 \cdot d_{Inconel}}{\ln\left(\frac{D_{preheater}+2 \cdot d_{Inconel}}{D_{preheater}}\right)} \right) \cdot (T_{reactor} - T_{MLI_{in}}) \tag{4–17}$$

$$\dot{Q}_{loss} = \sigma \cdot 2 \cdot A \cdot \epsilon_{eff_{MLI}} \cdot (T_{MLI_{in}}^4 - T_{MLI_{out}}^4) \tag{4–18}$$

$$\dot{Q}_{loss} = \sigma \cdot A \cdot \epsilon_{MLI} \cdot (2 \cdot T_{MLI_{out}}^4 - T_{\infty}^4 - T_{env}^4) \tag{4–19}$$

A can be defined as half of the container outer surface (Equation 4–20).

$$A = \frac{3 \cdot \pi \cdot (D_{preheater} + 2 \cdot d_{Inconel})^2}{4} \tag{4–20}$$

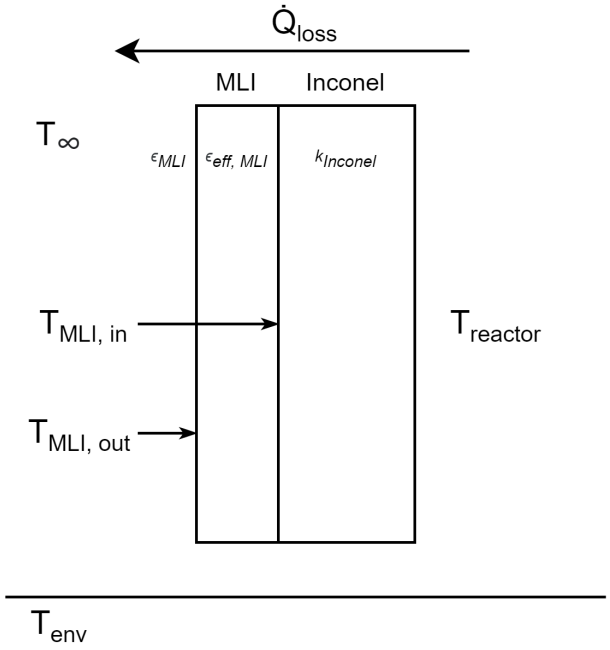

Fig. 4–10: Schematic representation of a simplified thermal analysis.

With the container dimensions (Equation 4–12), the preheater power (4–16), and the material thicknesses and densities, the mass and volume of the container and electric heater can be calculated.

For the reactor case, the inner volume can be estimated using the electrolyte ratio and the regolith and $CaCl_2$ densities (see Equation 4–21). The Metalysis Generation 1 R&D cells use an electrolyte ratio of 53.34 kg of $CaCl_2$ per kg of regolith [130]. This ratio has been optimized to generate ultra-pure terrestrial metals ($<$0.2 wt.% O_2 content) and not for oxygen production on the lunar surface. A lower electrolyte ratio could be potentially used for a more compact reactor design. However, the oxygen yield would also decrease, remaining more oxides in the metallic byproduct and increasing the complexity of the metal processing stage. In this analysis, the optimized electrolyte ratio (λ_{CaCl_2}) of 53.34 kg of $CaCl_2$ per kg of regolith is used. To calculate the reactor volume, a safety factor (f) of 1.1 is taken. This factor accounts for additional equipment, such as the inert anode or the cathode basket, and for the volume change between the molten and solid $CaCl_2$ phase.

$$V_{reactor} = f \cdot \left(\frac{M_{batch}}{\rho_{Regolith}} + \frac{\lambda_{CaCl_2} \cdot M_{batch}}{\rho_{CaCl_2}} \right) \tag{4–21}$$

The reactor design is similar to the preheater container design. A hollow Inconel cylinder with a wall thickness of 2 cm, isolated with MLI layers, and with a height equal to its diameter, is assumed. With the reactor dimensions (Equation 4–22), the material thicknesses and densities, the mass and volume of the reactor can be calculated.

$$D_{reactor} = \sqrt[3]{\frac{4V_{reactor}}{\pi}} \tag{4–22}$$

The electric power needed to perform the electrolysis can be estimated using the applied voltage and average current of the electrolysis cell. A cell voltage (U_{cell}) of 3 V shall reduce all the oxides in the regolith [20]. The average current is calculated using Equation 4–23, which is an adjustment of the Faraday law for the required oxygen production rate and considering the current efficiency (η_I). The current efficiency is assumed to be 35%, based on the data provided by Schwandt et al. [135], Hu et al. [141], and Lomax et al. [130].

$$I_{cell} = \frac{\lambda_{O_2} \cdot M_{batch}}{M_{W,O_2}} \cdot \frac{n_{0_2} \cdot F}{\eta_I \cdot t_{electrolysis}} \tag{4–23}$$

$$P_{electrolysis} = U_{cell} \cdot I_{cell} \tag{4–24}$$

I_{cell} is the average current flowing through the cell, M_{W,O_2} the molecular weight of diatomic oxygen, n the number of electrons required per diatomic oxygen molecule, which is 4 in this case, and F the Faraday constant.

The difference between the required electric power ($P_{electrolysis}$) and the theoretical electrolysis power ($P_{theor,electrolysis}$) defined in Equation 4–25 is assumed to be released in the form of heat. Equation 4–25 is directly related to the Gibbs free energy [17].

$$P_{theor,electrolysis} = \frac{M_{batch}}{t_{electrolysis}} \cdot \sum_{i}^{n} \frac{w_i \cdot \mu_{mol_i}}{M_{w,oxide_i}} \Delta G_i(T_{reactor}) \tag{4–25}$$

ΔG_i is the Gibbs free energy for the oxide i contained in the regolith at $T_{reactor}$, w_i is the weight fraction of the oxide i in highlands regolith (see Table 3–2), μ_{mol_i} is the ratio of the number of moles of O_2 per mole of oxide i, and $M_{W,oxide}$ the molecular weight of the oxide i. The Gibbs free energy of each oxide for the specified temperature has been obtained from [59]. To produce 15 t of oxygen per year with a duty cycle of 0.75, $P_{theor,electrolysis}$ is 18.45 kW, and $P_{electrolysis}$ is 66.29 kW.

$$\dot{Q}_{endothermic} = \frac{M_{batch}}{t_{electrolysis}} \cdot \sum_{i}^{n} \frac{w_i \cdot \mu_{mol_i}}{M_{w,oxide_i}} (\Delta H_{f,i}(T_{reactor}) - \Delta G_i(T_{reactor})) \tag{4–26}$$

Due to the endothermic nature of the electrolysis, 5.08 kW are required to sustain the chemical reaction (Equation 4–26). $\Delta H_{f,i}$ is the enthalpy of formation for the oxide i contained in the regolith at $T_{reactor}$ and, analog to the Gibbs free energy, it can be obtained from [59]. This thermal power can be provided by the 47.84 kW difference between $P_{electrolysis}$ and $P_{theor,electrolysis}$.

The heat losses to the environment ($\dot{Q}_{loss}$), which account for the remaining 42.76 kW, are calculated analog to the preheater container case (see Figure 4–10). However, the MLI insulation is reduced to increase the heat rejection to the environment, which avoids overheating the electrolyte. The total electric power required from the reactor is defined in Equation 4–24.

The mass and volume of the $CaCl_2$ electrolyte that must be initially brought from Earth can be directly calculated using Equations 4–27 and 4–28, respectively.

$$M_{electrolyte} = \lambda_{CaCl_2} \cdot M_{batch} \tag{4–27}$$

$$V_{electrolyte} = \frac{M_{electrolyte}}{\rho_{CaCl_2}} \tag{4–28}$$

Even if the vaporized electrolyte condensates in the oxygen purification unit and is recirculated towards the electrolysis cell, $CaCl_2$ losses will always be present in the FFC-Cambridge process. Existing regolith CaO might accumulate in the $CaCl_2$ salt, complicating salt reusability. Moreover, alkali metal oxides might also dissolve into the electrolyte as oxides or chlorides, contaminating the molten salt [130]. Although Lomax et al. [130] report that, for terrestrial applications, the Metalysis production units run throughout a year without replacing the salt, multiple $CaCl_2$ loss rates are evaluated in Chapter 8.

The inert anode is considered to be a calcium ruthenate composite. Its dimensions are based on the latest Metalysis FFC-Cambridge cell design [142]. The anode diameter is fixed at 70% of the reactor diameter with a thickness of 1 cm to provide sufficient structural strength. With the anode dimensions and material density, its mass and volume can be estimated. An anode loss rate of $1.5 \cdot 10^{-3}$ g/(cm^2·h) has been considered for $CaRuO_3$ [139]. The loss rate conservatively requires four replacements per year if the anode is replaced when 50% of the material has been consumed.

For this analysis, the oxygen purification unit is assumed to be a CHX that cools down the gas stream to the environment temperature. At around 850 K, the electrolyte salt condensates and is recirculated to the MSE reactor. The remaining volatiles might be separated from the oxygen stream with a YSZ separator after the condensation of the electrolyte. The CHX cooling power has been estimated using Equation 4–11. Analog to the MRE case, LiSTOT [113] has been used to estimate the CHX mass and volume. For the YSZ separator, the model proposed by Schreiner [17] has been considered. Compared to the MRE case, the exhaust gas has a lower temperature, which reduces the electrical conductivity of YSZ, significantly increasing the necessary power. For an annual oxygen production of 15 t and a duty cycle of 0.75, the YSZ separator mass is 31 kg, the volume 0.005 m^3, and the required power 2.07 kW. Alternative techniques, such as the volatile distillation at cryogenic temperatures proposed in [106], shall be investigated to develop oxygen purification units that require less power.

Similar to the hydrogen reduction and MRE processes, the mass and volume of the HEPA filter and any additional purification steps are neglected in this analysis. Infras-

tructure that connects the different components of the MSE assembly, such as pipes, valves, pumps, or structural parts, is also not considered in this analysis.

Tab. 4–6: Summary of the mass, volume, power, and cooling requirements of an MSE assembly for an annual oxygen production of 15 t and a duty cycle of 0.75.

	Non-consumables				Consumables	
Component	**Mass (kg)**	**Volume (m^3)**	**Power (W)**	**Cooling (W)**	**Mass (kg/y)**	**Volume (m^3/y)**
Preheater	298	0.22	2600	0	0	0
MSE Reactor	3417	7.48	66290	0	0	0
Electrolyte	12593	6.27	0	0	-[1]	-[1]
Anode	0	0	0	0	464	0.08
Oxygen Purification Unit	132	0.80	2070	1380	0	0
Total	16440	14.77	70960	1380	464	0.08

[1] Multiple electrolyte loss rates are evaluated in Chapter 8.

The final mass, volume, power, and cooling requirements of the MSE assembly for an annual oxygen production of 15 t and a duty cycle of 0.75 are summarized in Table 4–6. The model parameters used to calculate these requirements can be found in Table A–1. It must be noted that compared to the hydrogen reduction and MRE models, the MSE sizing model is not optimized. The assumption of a total oxide reduction might not yield the lowest equivalent system mass. A model that links the oxygen yield with the electrolysis time and the current efficiency shall be built based on the work already developed by Schreiner [17] for molten regolith electrolysis. The electrolyte is the principal mass and volume driver of the system. The electrolyte ratio has been chosen from terrestrial applications, and is, therefore, not optimal from an ISRU perspective. Experimental tests shall focus on investigating the influence of the electrolyte ratio on the oxygen yield to accurately assess the feasibility of the FFC-Cambridge process as an ISRU oxygen extraction technique. The current efficiency also plays a vital role in the power requirements of the overall assembly. Although a current efficiency of 35% has been chosen for a total oxide reduction, Hu et al. [141] report that, if the electrolysis conditions are carefully controlled, the efficiency could reach 50% for the Ti recovery from rutile. Moreover, Lomax et al. [130] studies also delivered a current efficiency of 49% for partial reduction of regolith simulants. However, the harsh environment and the restricted operations on the lunar surface might limit the achievable current efficiency and increase the electrolyte loss rate compared to analog terrestrial applications.

Furthermore, the use of an inert gas that pressurizes the reactor or the electrolyte melting and solidification during the insertion and extraction process must be further studied to select the option that requires the lowest equivalent system mass. Using an inert gas would include an additional consumable to the system, whereas a phase-changing electrolyte would demand more heating and cooling power. It would also increase the required downtime, reducing the assembly throughput.

4.5 Metal Processing

As most of the described O_2 extraction processes yield mixtures of unprocessed metals and slag, the metallic byproducts cannot be directly used for manufacturing purposes. The valuable materials must be separated from the slag, which might be further processed or disposed of.

Similar to the beneficiation case, the metal processing stage has been usually left out of ISRU process chain studies. As discussed in Section 4.4, most of the studies have focused on oxygen extraction, neglecting the further processing of their byproducts. Other works have assessed the challenges of on-site manufacturing on the lunar surface, assuming already available pure raw metals [143], or theoretically mentioning possible separation techniques, but without quantifying the efficacy of the refining processes [144].

Iron produced from reduced ilmenite must be separated from TiO_2 and other oxides. Magnetic separation is not possible due to the fact that Fe and the unreduced oxides are physically combined in former ilmenite grains [102]. The Carbonyl process (see Section 4.5.1) has been proposed as a possible technique to gain pure iron from regolith after its reduction with H_2. The remaining titanium dioxide might be further processed to extract Ti [4] or directly used for its material properties [105]. Another possibility would be to sinter it into structural components [67, 68]. A different approach to separate iron from unreduced oxides might be melting the solid byproduct and dissociating iron from the slag (see Section 4.5.2).

Other oxygen extraction techniques, such as molten regolith electrolysis, might be able to directly yield manufacturable metals and alloys by controlling the operating conditions of the process, minimizing, or totally avoiding, the necessity of a metal processing stage (see Section 4.4.2).

Molten salt electrolysis is capable of recovering close to 100% of the O_2 present in lunar regolith, yielding a heterogeneous mixture of metallic alloys [130]. Vacuum distillation is proposed in this work to extract specific metals from MSE alloys. In particular, the case of aluminum extraction from reduced anorthite-rich regolith is discussed in Section 4.5.3.

In the following sections section, the mass, volume, power, and cooling requirements for the recovery of Fe via carbonylation or melting and refining are presented. Aluminum extraction through vacuum distillation is also quantified. The values provided in the following sections are first-order approximations based on previous theoretical and experimental references. The behaviors of the materials during the processes are simplified to enable an analytical estimation of their requirements. Moreover, Chapter 5 discusses the material properties and purity levels of the gained raw materials.

4.5.1 Carbonylation

The Carbonyl process, also known as the Mond process, was already proposed during the last decade of the twentieth century as a promising method to extract Fe and

Ni from non-terrestrial local resources [145, 146, 147, 148]. As already discussed in Chapter 3, metallic iron and nickel might be found directly in lunar regolith at concentrations higher than 0.5 wt.% and 0.03 wt.%, respectively. A high concentration of these elements is expected in the vicinity of meteorites that survived the collision with the lunar surface [8]. The Carbonyl process would also be able to separate metallic iron from the slag produced during the ilmenite reduction with hydrogen. For an ilmenite concentration of 80 wt.% and a H_2 reduction conversion rate of 0.9, the solid byproduct would contain 41 wt.% TiO_2, 29 wt.% Fe, 8 wt.% unreacted $FeTiO_3$ and 22 wt.% unreduced regolith.

In the Carbonyl process, solid Fe and Ni are extracted by reaction with carbon monoxide gas, forming iron pentacarbonyl ($Fe(CO)_5$) and nickel tetracarbonyl ($Ni(CO)_4$), respectively. For the case where iron has to be extracted from reduced ilmenite, $Fe(CO)_5$ is formed at CO pressures above 70 bar and temperatures close to 400 K [149]. In contrast, the formation of $Ni(CO)_4$ would require lower CO pressures, close to 1 bar, and temperatures around 325 K.

$$Fe_{(s)} + 5CO_{(g)} \leftrightarrows Fe(CO)_{5(g)} \tag{4–29}$$

$$Ni_{(s)} + 4CO_{(g)} \leftrightarrows Ni(CO)_{4(g)} \tag{4–30}$$

Large-scale laboratory experiments on Fe extraction from reduced ilmenite reported that H_2S gas was capable of promoting the formation of iron pentacarbonyl. The optimum catalyst ratio was found to be 0.0061 kg of H_2S per kg of Fe. Higher amounts of hydrogen sulfide hindered the reaction. The addition of water vapor, which might directly come from the ilmenite reduction with hydrogen, enhances the catalytic activity of H_2S. Moreover, small quantities of NH_3 mixed with CO considerably improved the ability of H_2S to promote the carbonyl reaction. A gas mixture of 99.9 vol.% CO and 0.1 vol.% NH_3 was optimal. Two-hour experiments on 70 g and 140 g batches yielded iron recovery rates $>$90 wt.%. The reactor volume also played a vital role in the iron recovery rate. Increasing the batch mass for a constant reactor volume reduced the iron recovery due to lower vapor diffusion. [149]

$Fe(CO)_5$ and $Ni(CO)_4$ are solid below 252 K and 256 K; and liquid below 376 K and 316 K (at 1 bar), respectively. This fact eases their separation from the unreacted gas stream through condensation of the carbonyl compounds. The unreacted gas stream containing CO, NH_3, and H_2S might be recirculated into the reactor. However, it must be noted that during the carbonylation, undesired side reactions might form CO_2, Fe_3C, FeO, or FeN, among others. Therefore, carbon monoxide, ammonia, and hydrogen sulfide losses are expected to occur in the system.

The carbonyl compounds can be stored in pressure vessels if they are not decomposed directly after their formation. Iron and nickel dissociate from carbon monoxide at temperatures between 450 K and 525 K [150], regenerating CO for further generation of $Fe(CO)_5$ and $Ni(CO)_4$. Carbonyl decomposition is currently used in terrestrial applications to produce high-purity metal powders. If the carbonyl compounds are dissociated

during Chemical Vapor Deposition (CVD), it might be possible to directly manufacture specific components on-site via layer deposition (see Section 4.6.1).

The composition of carbonyl iron is presented in Chapter 5. Low concentrations of carbon, nitrogen, and sulfur are expected to be found in Fe, enabling the production of low-carbon steels. The presence of these elements within solid iron reasserts the losses in the system. Although most of the required carbon monoxide can be regenerated during the Carbonyl process, a CO_2 solid oxide electrolysis cell [151] would be able to account for the system losses while simultaneously producing additional O_2 from the carbon dioxide generated in the ECLSS. The ammonia and hydrogen sulfide losses must be resupplied from Earth.

$$2CO_{2(g)} \rightarrow 2CO_{(g)} + O_{2(g)} \tag{4–31}$$

The components inside the large box in Figure 4–11 are considered part of the carbonylation assembly and are investigated in terms of mass, volume, power, and cooling requirements. The dashed boxes are considered part of the handling stage and are, therefore, neglected in this analysis.

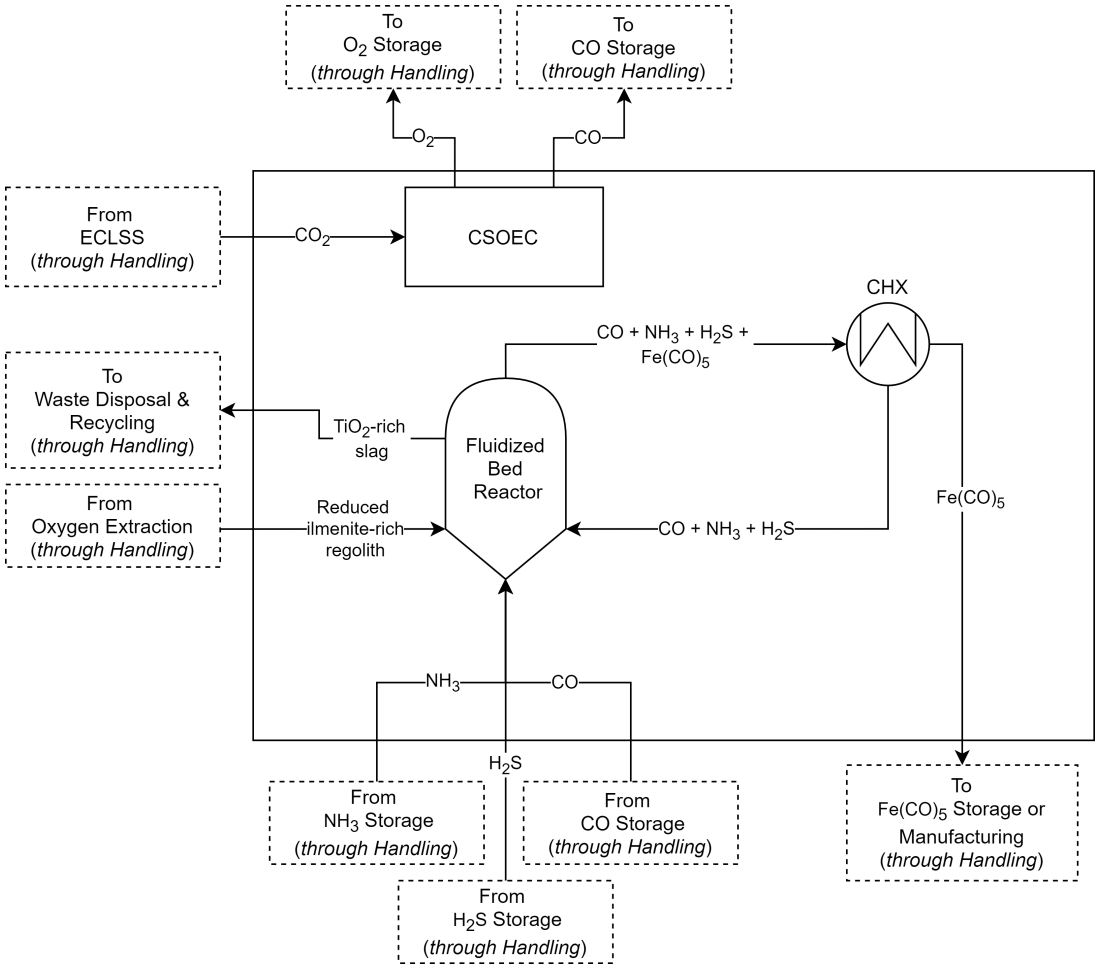

Fig. 4–11: Carbonylation assembly.

To dimension the carbonylation assembly, the solid byproduct produced by the hydrogen reduction assembly (see Section 4.4.1) is considered. For an oxygen production rate of 15 t/y (see Chapter 2), 197.5 t/y of ilmenite-rich regolith are necessary. Each kg of ilmenite-rich regolith (80 wt.% $FeTiO_3$) reduced with hydrogen yields 0.379 kg of TiO_2, 0.265 kg of Fe, 0.08 kg of unreacted $FeTiO_3$, and 0.2 kg of unreduced regolith. Therefore, after its reduction, 52.34 t/y of Fe would be available for recovery.

The reactor batch mass and time for the hydrogen reduction assembly are 1774 kg and 59 h, respectively. Theoretically, the same fluidized bed reactor could first reduce ilmenite with H_2, extracting water vapor, and subsequently generate $Fe(CO)_5$ to separate Fe from the slag [149]. However, in this analysis, two individual assemblies are considered. A single reactor, and sequential chemical processing, would increase the batch time, requiring larger reactor volumes. Moreover, a higher degree of freedom of the oxygen and metal production rates can be reached with two separate reactors.

As already mentioned, the recovery rate is highly sensitive to the inner reactor volume, which plays a vital role in vapor diffusion. To reach a 90 wt.% Fe recovery rate in a batch time of 2 h, Visnapuu et al. [149] reported a ratio of 50 kg of batch mass per m^3 of reactor volume. From the 1774 kg of ilmenite-rich regolith entering the hydrogen reduction assembly, only 1639 kg remain after the H_2O extraction. During the hydrogen reduction conversion time of 59 h, 29.5 carbonyl batches, with a reduced ilmenite mass of 55.6 kg per batch, could be processed. This batch mass would require an inner reactor volume of 1.11 m^3.

The carbonyl reactor is modeled as a hollow Inconel cylinder. The reactor is isolated with MLI layers to reduce the heat losses to the environment. To further decrease the heat losses, the height equals the reactor diameter, minimizing its surface. The carbonyl inner reactor volume requires a diameter and height of 1.12 m (see Equation 4–22). These dimensions are slightly lower than the required dimensions for the hydrogen reduction reactor.

Visnapuu et al. [149] also reported an optimal CO pressure of 83 bar. To dimension the reactor wall thickness, the highest wall thickness between d_u, which ensures the structural stability of the container (see Equation 4–32); d_c, which handles the circumferential stresses (see Equation 4–33); and d_l, which handles the longitudinal stresses (see Equation 4–34), is selected. Equations 4–33 and 4–34 are based on ASME's Boiler and Pressure Vessel Code [152].

$$d_u = 0.02\,m \tag{4–32}$$

$$d_c = f \cdot \frac{p \cdot D_{reactor}}{2S - 1.2p} \tag{4–33}$$

$$d_l = f \cdot \frac{p \cdot D_{reactor}}{4S + 0.8p} \tag{4–34}$$

An allowable Inconel stress (S) of 1050 MPa is considered. The internal pressure (p) is set to 83 bar. The reactor diameter ($D_{reactor}$) is 1.12 m, and a safety factor (f) of 5.5 is used. With these parameters, a shell thickness of 2.5 cm is calculated. The reactor dimensions and Inconel density allow the calculation of the required mass and volume.

It is assumed that the reduced ilmenite is processed directly after the reduction with H_2, which occurs at 1000 K. Therefore, the first carbonyl batches might have a temperature higher than the required 400 K, whereas the last batches a temperature below 400 K due to the heat losses to the environment. Although an optimized thermal control system might be able to completely avoid the need of heating the reduced ilmenite before its carbonylation, in this analysis, an electric heater is considered necessary to bring the solid material from an environment temperature (T_{env}) of 293 K to a reactor temperature ($T_{reactor}$) of 400 K in 15 min ($t_{heating}$). The heater also accounts for the reactor heat losses to the environment ($\dot{Q}_{loss}$). The losses are calculated following the approach presented in Figure 4–10 and Equations 4–17 to 4–19.

$$P_{heater} = \frac{\int_{T_{env}}^{T_{reactor}} \sum_i^n M_i \cdot C_{p,i}(T) dT}{t_{heating}} + \dot{Q}_{loss} \tag{4–35}$$

As a simplification, P_{heater} considers the necessary power to heat each of the solid byproduct components individually. M_i and $C_{p,i}$ are the individual batch masses and heat capacities of the solid byproduct components: TiO_2, Fe, $FeTiO_3$, and unreduced regolith. The individual batch masses can be obtained from the total batch mass and the yields discussed above. The electric heater dimensions are scaled from the values provided in [11]. The volume of the heater equals one-sixth of the container volume. The heater mass depends on the power by a factor of 5.6 kg/kW.

A CHX is added to the carbonylation assembly to reduce the gas stream temperature from the reaction temperature ($T_{reactor}$) of 400 K to an environment temperature (T_{env}) of 293 K, enabling the condensation of $Fe(CO)_5$ and the recirculation of CO, NH_3, and H_2S to the reactor. Due to the high operating pressures of the carbonylation reaction, a CHX might not be necessary. Iron pentacarbonyl might directly condensate inside the reactor, allowing an easier recovery [149]. A HEPA filter might be included before the CHX to remove the particulate matter from the gas stream. As a simplification, the mass and volume of the HEPA filter are neglected.

$$\dot{Q}_{cooling} = \frac{T_{reactor} - T_{env}}{t_{batch}} \cdot (M_{Fe(CO)_5} \cdot (C_{p,Fe(CO)_5} + \frac{L_{vap,Fe(CO)_5}}{T_{reactor} - T_{env}}) + M_{CO} \cdot C_{p,CO}) \tag{4–36}$$

$\dot{Q}_{cooling}$ is the heat flow rate that must be removed by the CHX and t_{batch} the batch time of 2 h. Visnapuu et al. [149] report that the CO flow rate exhausting the reactor is not essential for the carbonyl formation as long as a constant CO pressure is maintained by inflowing CO. M_i and $C_{p,i}$ are the batch masses and specific heats at constant pressure for $Fe(CO)_5$ and CO. The iron pentacarbonyl mass is obtained using the total batch mass of 55.6 kg, the yields discussed above, and Equation 4–29. The carbon monoxide

mass is calculated with the ideal gas law to maintain a reactor volume of 1.1 m^3 at 83 bar. $L_{vap,Fe(CO)_5}$ is the enthalpy required to condensate $Fe(CO)_5$ and separate it from the gas stream. The mass and volume requirements of the CHX have been obtained using LiSTOT [113].

Ammonia and hydrogen sulfide are considered consumables of the Carbonyl process. H_2S might react during the carbonylation, forming sulfides, such as FeS. A small amount of H_2S is expected to be recirculated into the reactor after the condensation of iron pentacarbonyl. However, sulfur might also be present in Fe during its decomposition. In this analysis, it is assumed that no H_2S can be recirculated during the Carbonyl process and that 0.0061 kg of H_2S are required per kg of Fe inside the reactor [149]. Hydrogen sulfide would be brought from Earth in pressurized vessels at 400 bar and 293 K.

As discussed above, Visnapuu et al. [149] propose a gas mixture of 99.9 vol.% CO and 0.1 vol.% NH_3, which would require 0.0006 kg of NH_3 per kg of CO. If the calculated masses of iron and carbon monoxide considered to dimension the CHX are used, a ratio of 0.0032 kg of NH_3 per kg of Fe is obtained. Ammonia encourages the formation of nitrogen compounds such as FeN, which increase the nitrogen content in Fe. The N content can reach 0.25 wt.% [153]. 0.25 wt.% is slightly lower than the optimal mass ratio between ammonia and iron. Some NH_3 might flow back into the reactor after the condensation of iron pentacarbonyl. To estimate the amount of ammonia that must be brought from Earth, a loss rate of 0.0025 kg of NH_3 per kg of Fe is considered. Ammonia is also transported in pressurized vessels at 400 bar and 293 K.

It must be noted that NH_3 and H_2S can be found in the form of solar wind-implanted volatiles on the lunar surface [154]. If their extraction and separation from other volatiles are proven feasible, it could potentially eliminate the resupply needs from Earth.

A crew of 6 CMs produces 6.19 kg/d of CO_2 [24] that can be reduced to 3.94 kg/d of CO through solid oxide electrolysis (see Equation 4–31). Considering the recovery rate and iron yield discussed above, as well as the carbonyl batch mass and time, 174 kg/d of Fe are produced, which require 435 kg/d of CO to generate $Fe(CO)_5$ (see Equation 4–29). If carbon monoxide was not regenerated during the decomposition of iron pentacarbonyl, the ECLSS could only account for 0.9 wt.% of the required CO. The carbon content in carbonyl iron is usually lower than 0.3 wt.% for terrestrial applications [153]. These unavoidable losses that occur during the decomposition of carbonyl compounds already account for a third of the maximum ECLSS CO production. Moreover, CO_2 might be formed during the carbonyl reaction, which would increase the CO losses.

A CSOEC is dimensioned to convert 6.19 kg/d of CO_2 to 3.94 kg/d of CO and 2.25 kg/d O_2. For the iron production defined in this work, a crew of 6 CMs can barely cope with the losses of a carbonyl assembly. If the actual system incurs higher losses or steel with a higher C content is desired, the Fe production rate must be reduced, or carbon must be resupplied from Earth. Moreover, the SCRA would hardly be able to produce CH_4 for rocket fuel.

The mass, volume, power, and cooling requirements for a CSOEC are obtained from

LiSTOT [113]. However, CO_2 electrolysis is usually combined with a Boudouard reactor to disproportionate CO into CO_2 and C, enabling the recirculation of carbon dioxide into the electrolysis cell. Therefore, most systems report the mass, volume, power, and cooling requirements of the electrolysis cell and Boudouard reactor combined. Although the Boudouard reaction would not be required for the carbonylation, its requirements are included in this analysis. A CSOEC composed of a CO_2 electrolysis cell and a Boudouard reactor would completely replace the SCRA of the ECLSS.

Infrastructure that connects the different components of the carbonylation assembly, such as pipes, valves, pumps, or structural parts, is not considered in this analysis.

Table 4–7 presents the mass, volume, power, and cooling requirements for an annual iron production of 47 t and a duty cycle of 0.75. The carbonyl reactor model is based on laboratory experiments conducted on 70 g and 140 g samples [149]. The reaction kinetics and iron recovery rates must be investigated in detail for large-scale productions. If iron pentacarbonyl cannot be recovered directly as liquid inside the reactor, it must be condensed in a CHX. CO that flows out of the reactor with $Fe(CO)_5$ must be controlled, as it significantly influences the amount of cooling power of the CHX. Ammonia and hydrogen sulfide act as catalysts and are consumables of the system. However, the required quantities to enhance the carbonyl reaction are relatively small. Even if they have to be resupplied from Earth, the process is expected to be feasible on the lunar surface. Volatile mining would completely eliminate their resupply. The CO production and, therefore, the metal production are limited by the amount of CO_2 produced by the crew. Large-scale steel and methane coproduction would require carbon resupply from Earth volatile mining is proven not feasible.

Tab. 4–7: Summary of the mass, volume, power, and cooling requirements of a carbonylation assembly for an annual iron production of 47 t and a duty cycle of 0.75.

	Non-consumables				Consumables	
Component	**Mass (kg)**	**Volume (m^3)**	**Power (W)**	**Cooling (W)**	**Mass (kg/y)**	**Volume (m^3/y)**
Carbonyl Reactor	1273	1.47	4130	0	0	0
CHX	258	2.04	0	3540	0	0
NH_3	0	0	0	0	118	0.45
H_2S	0	0	0	0	319	0.56
CSOEC	151	0.20	3420	750	0	0
Total	1682	3.71	7550	4290	437	1.01

4.5.2 Melting and Refining

Berggren et al. [85] propose refining iron produced from the ilmenite reduction with H_2 through metal-oxide phase separation. The solid byproduct is heated to 1850 K, melting Fe, while TiO_2 and the other oxides remain solid. In terrestrial iron refining,

quicklime (CaO) and other reagent fluxes are traditionally used to favor the coalescence of slag, easing the separation of impurities. However, for ISRU applications, the amount of reagent mass that must be brought from Earth must be minimized. Therefore, a metal-oxide phase separation that avoids using additional reagent fluxes is desirable.

As discussed in Section 4.5.1, for beneficiated regolith with an ilmenite concentration of 80 wt.% and a H_2 reduction conversion rate of 0.9, the solid byproduct would contain 41 wt.% TiO_2, 29 wt.% Fe, 8 wt.% unreacted $FeTiO_3$, and 22 wt.% unreduced regolith. The large amount of oxides present in the metallic byproduct, 71 wt.% compared to 29 wt.% of Fe, might favor their coalescence without adding reagent fluxes, making the direct phase separation of molten iron from slag a viable option. Moreover, the density of Fe is significantly higher than the density of TiO_2 and the other oxides. This fact might additionally favor the iron-slag phase separation as iron could be evacuated through the bottom of the crucible, remaining the slag on the top.

When the amount of slag that has to be separated from the metal is low, a direct phase separation would not be possible. The molten metal viscosity would prevent the coalescence of the impurities. This could be the case with molten regolith electrolysis. Although the composition of the metallic mixture might be controlled through the operating temperature of the MRE reactor (see Section 4.4.2), small amounts of oxides are expected to be found when extracting the molten metals from the electrolytic cell. The achievable purity level of the refined metals might be limited if no additional reagent fluxes is considered. Berggren [155] shared that laboratory tests conducted on reduced regolith simulants returned iron purity levels $>$98.5 wt.%. In these studies, no additional purification steps other than a metal-oxide phase separation were taken.

It must be noted that this approach is relatively unstudied in the literature. Terrestrial refining techniques do not need to limit the reagent fluxes, and ISRU analyses have usually omitted the metal refining steps. Experimental tests must be carried out to assess the feasibility of this purification process, and to determine its purity level limitations. This process is expected to be simpler than the carbonylation discussed in Section 4.5.1. However, operating on the lunar surface might impose significant constraints on the melting operations. Due to the tenuous atmosphere, iron and the oxides might vaporize before reaching a molten state, requiring a pressurized environment for the process to be viable. Although a high amount of energy is expected to be required to melt the solid byproduct, the refined iron might be directly manufacturable via casting or extrusion without an additional solidification and storage step.

Figure 4–12 shows a schematic representation of a melting and refining assembly. Reduced ilmenite is processed following the approach proposed by Berggren et al. [85]. A direct iron-oxide phase separation without reagent fluxes or other consumables is considered. The refined iron properties are discussed in Chapter 5. A total iron recovery of 90 wt.% is assumed.

Each kg of beneficiated regolith (80 wt.% $FeTiO_3$) reduced with hydrogen yields 0.379 kg of TiO_2, 0.265 kg of Fe, 0.08 kg of unreacted $FeTiO_3$, and 0.2 kg of unreduced regolith. For an oxygen production rate of 15 t/y, 197.5 t/y of beneficiated regolith are necessary. This rate would produce 47 t/y of Fe.

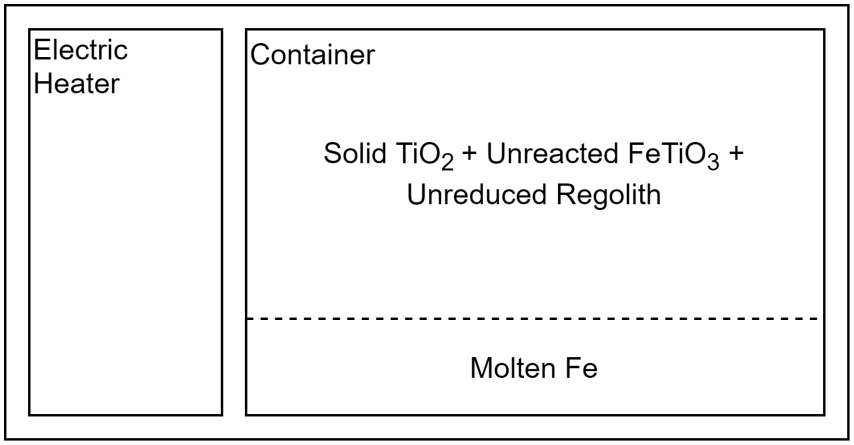

Fig. 4–12: Schematic representation of a melting and refining assembly.

The melting and refining assembly might be composed of a container and a heater, which might be based on induction or electric arc heating. As already discussed, molten iron might accumulate at the bottom of the container due to its higher density.

The container is modeled as a hollow cylinder. The walls are composed of an inner 2 cm layer of refractory material with a density of 3000 kg/m^3 and thermal conductivity of 1.5 W/(m·K), as proposed in [17] for MRE, and a 5 mm outer Inconel layer as structural shell. The container is isolated with MLI layers to reduce the heat losses to the environment. To further decrease the heat losses, the container height equals the diameter, minimizing its surface. The inner volume of the container equals the inner volume of the H_2 reduction reactor presented in Section 4.4.1. With the material thicknesses and densities, the total container mass and volume can be estimated.

The electric heater that provides the required power is scaled from the values provided in [11]. The volume of the heater equals one-sixth of the container volume. The heater mass depends on the power by a factor of 5.6 kg/kW. As a simplification, P_{heater} considers the necessary power to individually heat each of the components of the solid byproduct from a reactor temperature ($T_{reactor}$) of 1000 K to a container temperature ($T_{container}$) of 1850 K. At 1850 K, iron is already molten. It is assumed that the solid byproduct is directly processed after the ilmenite reduction with H_2. Therefore, its initial temperature equals the operating temperature of the reactor. P_{heater} also considers the latent heat of fusion of iron and the heat losses to the environment ($\dot{Q}_{loss}$). The losses are calculated following the approach presented in Figure 4–10 and Equations 4–17 to 4–19 for the chosen refractory and structural materials instead of exclusively for Inconel.

$$P_{heater} = \frac{\int_{T_{reactor}}^{T_{container}} \sum_i^n M_i \cdot C_{p,i}(T) dT + M_{Fe} \cdot L_{fusion,Fe}}{t_{batch}} + \dot{Q}_{loss} \tag{4–37}$$

M_i and $C_{p,i}$ are the individual batch masses and heat capacities of the solid byproduct components: TiO_2, Fe, $FeTiO_3$, and unreduced regolith. M_{Fe} and $L_{fusion,Fe}$ are the iron mass and enthalpy of fusion, respectively. The batch masses of the individual com-

ponents can be obtained from the 1774 kg of regolith per batch presented in Section 4.4.1 and from the yields discussed above. The batch time (t_{batch}) equals the hydrogen reduction batch time of 59 h.

The mass, volume, power, and cooling requirements of a melting and refining assembly that produces 47 t/y of Fe from reduced ilmenite are summarized in Table 4–8. The Carbonyl process is significantly more complex than the melting and refining technique. It must operate under high pressures and include catalysts that might need to be resupplied from Earth. Although the mass and volume requirements of the melting and refining assembly are lower than for the carbonylation assembly, the required power is significantly higher. It must be noted that, to model the melting and refining assembly, first-order assumptions have been made due to the lack of experimental data. The iron recovery rate and the quality of the yielded metal must be investigated in detail to assess its feasibility as an ISRU process.

Tab. 4–8: Summary of the mass, volume, power, and cooling requirements of a melting and refining assembly for an annual iron production of 47 t and a duty cycle of 0.75.

Component	Mass (kg)	Volume (m^3)	Power (W)	Cooling (W)
Heater	152	0.23	27220	0
Container	670	1.39	0	0
Total	822	1.62	27220	0

4.5.3 Vacuum Distillation

Most of the oxygen extraction and metal processing techniques discussed in this work view the lunar environment as a challenge. For instance, processes in which materials are found in a molten state, such as molten regolith and salt electrolysis, or melting and refining, require pressurized vessels to avoid the vaporization of the components due to the tenuous lunar atmosphere. The lunar atmosphere has already been described in Chapter 3. The pressure on the Moon considerably depends on the lunar surface activity. Therefore, for continuous human presence and ISRU operations on the lunar surface, a pressure higher than 10^{-11} bar might be expected [64]. These atmosphere conditions shall be viewed as an opportunity to apply material processing techniques that might not be readily available on Earth.

Vapor phase pyrolysis has been proposed as an oxygen extraction technique that takes advantage of the vacuum and solar radiation conditions experienced on the lunar surface. This technique is based on the vaporization of metal oxides present in lunar regolith, simultaneously reducing the oxides into suboxides and producing oxygen [93, 94, 156]. However, vapor phase pyrolysis demands significantly high temperatures and large amounts of energy to break the chemical oxide bonds. Specific metals, such as sodium and potassium, whose associated oxides have relatively low Gibbs free energies, might be directly recoverable at moderate temperatures under ultra-high vacuum conditions [80]. More abundant lunar metals (see Table 3–3), such as cal-

cium or aluminum, shall be more challenging to recover due to their higher Gibbs free energies [156].

In this section, vacuum distillation is proposed as a metal processing technique that takes advantage of the lunar vacuum and recovers specific metals for further ISRU manufacturing purposes. Vacuum distillation separates elements or compounds based on differences in their boiling points. The reduced pressure environment lowers the boiling points of the elements, saving thermal and chemical energy. This process shall be applied once most of the oxygen has been removed from the lunar regolith by, for instance, the FCC-Cambridge process. As discussed in Section 4.4.3, molten salt electrolysis yields a heterogeneous metallic mixture composed of multiple alloys as a byproduct after the oxygen extraction. The metals contained in this heterogeneous mixture could be separated via vacuum distillation. In particular, aluminum can be easily recovered using this method due to the difference in its boiling points compared to other elements contained in lunar regolith.

Based on the latest laboratory experiments carried out by Lomax et al. [130], the principal elements present in the metallic mixture after the FCC-Cambridge process are silicon, aluminum, calcium, iron, magnesium, and titanium. A small amount of unreduced oxides and minor regolith elements, such as sodium, phosphorus, manganese, chromium, or potassium (see Table 3–3), might also be present. With respect to Al, these elements can be sorted into two groups based on their vapor pressures and boiling points. Table 4–9 presents the approximate boiling points of these elements at different pressures. The values have been obtained from the data provided by Honig [65]. Group I corresponds to the elements that have a lower boiling point than Al. Group II corresponds to the elements that have a higher boiling point than Al. The unreduced oxides present in the metallic mixture would mostly belong to Group II due to their high boiling points [156].

To recover aluminum, a two-step process might be carried out. First, for a certain operating pressure, the metallic mixture is heated to a temperature lower than the boiling point of aluminum. The components that belong to Group I would vaporize, remaining Al and the Group II elements mostly in solid or liquid state. The vaporized elements might be vented to the lunar atmosphere or conducted towards a condenser for recovery and further processing. Afterwards, the operating temperature increases to a temperature higher than the boiling point of Al and lower than the lower boiling point of Group II elements. Aluminum gas shall be conducted towards a condenser for recovery. Group II elements remain as solids or liquids and could be processed further.

The difference between the boiling points of Al and Mn, the closest Group I element, is higher than 150 K for the whole pressure range. The difference between the boiling points of Al and Cr, the closest Group II element, is also higher than 150 K. Moreover, Mn and Cr are scarce in lunar regolith, with expected concentrations lower than 0.5 wt.% (see Table 3–3). The difference between the boiling points of Al and Ca, the second closest Group I element and one of the most abundant regolith constituents, is higher than 400 K for the whole pressure range. The difference between the boiling points of Al and Fe, the second closest Group II element, is also higher than 200 K.

Tab. 4–9: Boiling points of regolith components at several operating pressures [65].

Element		Boiling points (K)					
		10^{-10} bar	10^{-8} bar	10^{-6} bar	10^{-4} bar	10^{-2} bar	1 bar
Group I	P	340	380	430	490	570	700
	K	315	365	430	530	700	1030
	Na	370	430	510	620	800	1150
	Mg	490	560	640	780	980	1665
	Ca	580	670	780	950	1240	1760
	Mn	850	970	1120	1325	1370	2335
	Al	1010	1160	1350	1610	2000	2740
Group II	Cr	1175	1325	1530	1800	2210	3035
	Fe	1210	1360	1580	1880	2310	3135
	Si	1260	1430	1670	1955	2400	3540
	Ti	1340	1590	1825	2165	2700	3560

Group I and II might be subdivided into further groups to separate additional elements through vacuum distillation. For instance, Fe and Si, or Mg and Ca could also be separated through this technique.

Two options might be considered to extract aluminum after the FCC-Cambridge process. If no beneficiation is performed and highlands regolith is the feedstock of the molten salt electrolysis cell, a metallic byproduct rich in Si ($\sim$38 wt.%), Al ($\sim$24 wt.%), and Ca ($\sim$19 wt.%), with significant amounts of Fe ($\sim$9 wt.%), and Mg ($\sim$8 wt.%) can be expected. However, if anorthite beneficiation (90 wt.% $CaAl_2Si_2O_8$) is considered, the solid byproduct would contain Si ($\sim$36 wt.%), Al ($\sim$31 wt.%), and Ca ($\sim$24 wt.%). The remaining $\sim$9 wt.% would be composed of Fe, Mg, minor regolith elements, and unreduced oxides.

If the boiling points at constant pressure or the vapor pressures at constant temperature are compared between these components, the differences can be used as guidance when determining which one should exhibit preferential vaporization [157]. If only the principal elements are considered, Calcium contained in Ca-Al-Si alloys would easily vaporize during the first step of the vacuum distillation process. Once Ca has been removed, Al contained in Al-Si alloys would also easily vaporize during the second step of the vacuum distillation process, remaining Si in the residual phase.

However, to completely understand the vacuum distillation process and be able to quantify the separation degree of multiple components at different operating pressures and temperatures, the phase diagrams of the metallic mixtures must be known. Phase diagrams are usually developed in metallurgy for binary alloys at atmospheric temperature. Phase diagrams of more than two components or phase diagrams under low-pressure conditions are scarce or non-existent. Building these diagrams is usually

time-consuming and cost-intensive. A large number of experiments must be carried out to obtain reliable data. Therefore, theoretical thermodynamic models are a more efficient method to derive the thermodynamic properties and calculate the phase equilibrium of multicomponent systems under vacuum conditions. For instance, Liu et al. [157] developed a Molecular Interaction Volume Model (MIVM) to predict the behavior of ternary Si-Fe-Al alloys during vacuum distillation. The MIVM is capable of estimating the separation coefficients, which can be used to determine whether two components can be separated from each other by vacuum distillation and to obtain the separation degree of these elements. In the future, the model developed by Liu et al. [157] could be adapted for Ca-Al-Si alloys to obtain the corresponding separation degree of different elements. Although the development of an MIVM model for ternary Ca-Al-Si alloys is out of the scope of this work, the separation degree of Ca has been guessed from the conclusions reached in [157] and from the boiling point differences between Ca, Al, and Si. This degree should be close to 100% regardless of the Ca content in the liquid-solid phase. As a simplification, only Ca, Al, and Si are considered in this analysis, as they are the principal components of the metallic mixture. Nevertheless, the elements of Group I would behave analog to Ca, and the elements of Group II would behave analog to Si. For the second step of the vacuum distillation process, the remaining metallic mixture might be simplified to a binary Si-Al alloy. Liu et al. [158] also developed an MIVM model for binary Si-Al alloys under vacuum conditions.

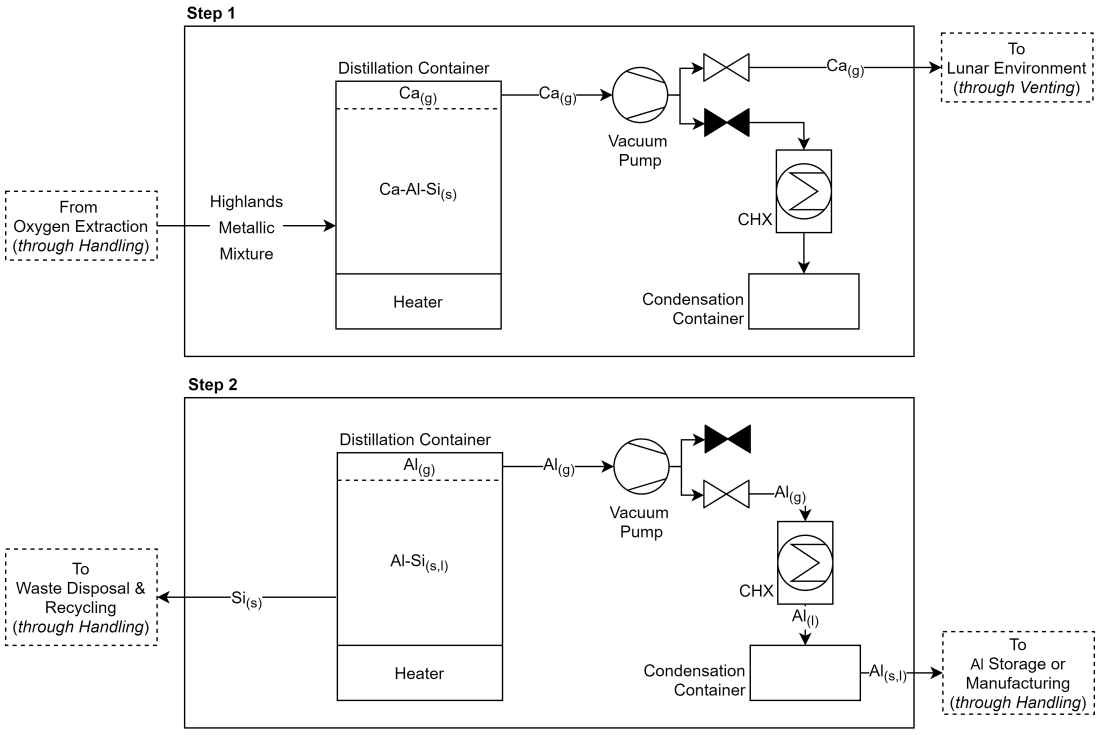

Fig. 4–13: Vacuum distillation assembly for a two-step process. Ca represents all Group I elements. Si represents all Group II elements.

The components inside the large boxes in Figure 4–11 are considered part of the vacuum distillation assembly and are investigated in terms of mass, volume, power, and cooling requirements. The dashed boxes are considered part of the handling stage and

are, therefore, neglected in this analysis. Infrastructure that connects the different components of the assembly, such as pipes, valves, or structural parts, are also neglected. The vacuum distillation assembly is similar to the schematic concepts proposed in the literature for vapor phase pyrolysis [19, 103, 80]. However, an electric heater could be used instead of a solar concentrator due to the lower required temperatures.

From Section 4.4.3, a regolith batch mass of 236 kg and an electrolysis time of 45 h for the FFC-Cambridge process is obtained. Considering an oxygen yield of 0.44 kg of O_2 per kg of highlands regolith, each batch produces 132 kg of highlands metallic mixture. The vacuum distillation is carried out in parallel to the molten salt electrolysis. Therefore, for the Ca and Al contents discussed above, the assembly must vaporize $\sim$80 kg every 45 h.

Due to the characteristic shape of the vapor pressure curves, decreasing the operating pressure of a vacuum distillation assembly would always be beneficial in terms of thermal power requirements. Lower operating pressures mean lower boiling points. Therefore, less heat shall be required to bring the elements from solid to vapor phase. However, the operating pressure also influences the removal rate of the vapor phase from the distillation container. For a constant pumping speed, a lower operating pressure reduces the mass flow exhausting the chamber, requiring longer processing times.

If the maximum aluminum distillation temperatures are limited to 1800 K, which is between the molten regolith and molten salt electrolysis temperatures, the operating pressure would be 10^{-3} bar. For this operating pressure, a temperature above 1100 K would be required to distill calcium. Roots pumps can operate at 10^{-3} bar. A Leybold RUVAC WH vacuum pump is considered to dimension the vacuum distillation assembly. The pump speed at 10^{-3} bar is 1.36 m^3/s. Using the ideal gas law, a single vacuum pump could extract 2.2 kg/h of Ca, and 0.9 kg/h of Al. This processing rate would annually yield 5400 kg of Al, for a recovery rate of 90 wt.%, and require two vacuum pumps connected in parallel. If lower boiling points and operating pressures are considered, the mass flow rate would excessively increase, requiring a significantly higher number of vacuum pumps.

The distillation container is modeled as a hollow cylinder. The walls are composed of an inner 2 cm layer of refractory material with a density of 3000 kg/m^3 and thermal conductivity of 1.5 W/(m·K), as proposed in [17], and a 5 mm outer Inconel layer as structural shell. The container is isolated with MLI layers to reduce the heat losses to the environment. To further decrease the heat losses, the container height equals the diameter, minimizing its surface. The inner volume of the container equals the inner volume of the MSE preheater described in Section 4.4.3.

The electrolyzed regolith is at approximately 1223 K at the end of the MSE process. If the metallic mixture was exposed directly to the lunar environment at that temperature, it would vaporize almost completely, losing most of its aluminum content. Therefore, the temperature must be reduced below 1000 K. This temperature reduction could be achieved during the FCC-Cambridge process if the electrolyte is solidified during the extraction process instead of using an inert gas to pressurize the MSE reactor. The melting point of the $CaCl_2$ electrolyte would be close to 1000 K.

To estimate the power requirements of the electric heater, the composition of MSE byproduct is simplified to Si (40.5 wt.%), Al (31 wt.%), and Ca (28.5 wt.%). As the thermophysical properties of the Ca-Al-Si alloy are not known, the properties of the individual components are weight averaged. The Ca-Al-Si alloy is introduced at 1000 K. During the first two hours, the temperature rises to 1100 K. For 9 h, maintaining a distillation pressure of 10^{-3} bar, Ca is totally vaporized and removed from the container. During the next 11 h, the container temperature increases to 1800 K. At this point, Al vaporizes for 23 h. The electric heater power is calculated using the distillation times, the batch masses, the individual enthalpies of fusion and vaporization of Ca and Al, and the heat capacities of Ca, Al and Si. The heat losses to the environment are calculated analog to the preheater container case. Once the power is known, the heater is scaled from the values provided in [11]. The volume of the heater equals one-sixth of the container volume. The heater mass depends on the thermal power by a factor of 5.6 kg/kW.

After the vaporization, aluminum must be condensed. The pressure rise across the vacuum pump would reduce the required temperature drop to start the condensation. Schlüter et al. [103] propose that metals separated through vapor pyrolysis are condensed on cooled plates. If the refined metals are not directly conducted to the manufacturing stage in liquid phase, it shall solidify in the condensation container to ease its further handling and storage. To estimate the cooling power requirements of a CHX, aluminum is assumed to be brought from a distillation temperature of 1800 K to an environment temperature of 293 K. The enthalpies of vaporization and fusion of Al are also considered. The mass and volume requirements of the condensing heat exchanger have been estimated using LiSTOT [113].

The aluminum condensation container is modeled as a hollow Inconel cylinder with a wall thickness of 2 cm. Its inner volume is 35% of the distillation container volume.

Tab. 4–10: Summary of the mass, volume, power, and cooling requirements of a vacuum distillation assembly for an annual aluminum production of 5.4 t and a duty cycle of 0.75.

Component	Mass (kg)	Volume (m^3)	Power (W)	Cooling (W)
Heater	99	0.03	17600	0
Distillation Container	178	0.20	0	0
Vacuum Pumps	1400	0.77	5370	0
CHX	464	3.65	0	6300
Condensation Container	152	0.07	0	0
Total	2115	4.72	22970	6300

Table 4–10 presents the mass, volume, power, and cooling requirements of the vacuum distillation assembly for an annual aluminum production of 5.4 t and a duty cycle

of 0.75. It must be noted that the sizing model is not optimized with respect to the operating pressure, temperature, and mass flow rate exhausting the reactor. However, considering commercial vacuum pump designs, reasonable operating pressures have been selected to process the entire batch masses. The CHX size could be reduced if part of the necessary cooling power is provided by the heat losses to the environment of the condensation container. Unlike the rest of the containers described in this work, it would be detrimental to include MLI insulation in the condensation container.

4.6 Manufacturing

After the metal processing stage, bulk materials might be transformed into end products. This process is carried out in the manufacturing and post-processing stages of the ISRU process chain. Moreover, the refined feedstock might need to be prepared before entering the manufacturing stage. Several manufacturing techniques currently used on Earth have been proposed for on-site construction on the lunar surface [147, 23]. The reduced lunar gravity and tenuous atmosphere would require modifications to these proposed techniques [159].

The shape of the end products and the nature of the feedstock materials define the requirements to select a suitable manufacturing technique. Therefore, from the processes proposed in [147], the suitable manufacturing techniques to produce the state-of-the-art and tubular radiator geometries described in Section 2.3.1 have been identified. Supplementary processes have been considered to prepare the feedstock for the manufacturing stage.

CVD is discussed in Section 4.6.1. This technique can be combined with the Carbonyl process presented in Section 4.5.1 to deposit coating layers on preheated forms, which could produce pipes for the tubular radiator. Extrusion is discussed in Section 4.6.2. It could return products with uniform cross-sections, such as wire feedstock for additive manufacturing, or pipes for the tubular radiator. Additive manufacturing and casting are discussed in Sections 4.6.3 and 4.6.4, respectively. These techniques shall be capable of producing complex shapes, such as the ones required for the state-of-the-art radiator.

In the following sections, the manufacturing techniques mentioned above are qualitatively analyzed. However, the mass, volume, power, and cooling requirements of each technology are not quantitatively determined. The quantitative analysis is only carried out between the excavation and metal processing stages of the ISRU process chain. The mass, volume, power, and cooling requirements for on-site manufacturing on the lunar surface are highly uncertain. These requirements significantly depend on the dimensions and shapes of the produced parts. Moreover, no relevant data has been found in the literature on equipment specifically designed for space environments. Similar to the regolith excavation case, if analogies to terrestrial manufacturing equipment are made, the reported values would be excessively high compared to other stages of the ISRU process chain. Terrestrial equipment is not characterized by a lightweight and compact design with low energy consumption, which is essential for space-related technologies.

4.6.1 Chemical Vapor Deposition

CVD involves allowing metal vapors to contact a hot surface and build coating layers atom by atom [147]. CVD has been proposed in conjunction with the Carbonyl process discussed in Section 4.5.1 to manufacture components from $Fe(CO)_5$ on the lunar surface [146, 150].

For substrate temperatures between 450 K and 525 K, iron pentacarbonyl decomposes upon contact with the surface to yield metallic iron and carbon monoxide [150]. CO is then recirculated to the carbonylation assembly to further generate $Fe(CO)_5$. The kinetics of iron pentacarbonyl deposition have been thoroughly investigated in the literature [160, 161]. The deposition rate of iron layers increases with increasing temperatures and decreases with increasing pressures [160]. Moreover, similar to the carbonylation case, the addition of water vapor, ammonia, carbon dioxide, or hydrogen favors the purity level and deposition rate of carbonyl iron coatings [146, 161].

Preheated forms enable the production of a wide variety of thin shapes by vapor layer deposition. For instance, cylindrical forms could be used to manufacture pipes that are used for the assembly of lunar infrastructure components. However, the maximum reachable thickness of the carbonyl vapor deposition process must be determined by experimental testing. Jenkin [150] suggested that CVD could deposit coatings with the necessary thicknesses to produce pressure vessels, structural members, and other relevant components for a Moonbase.

Iron pentacarbonyl can also decompose thermally into fine-grained powder. Particle sizes $<$10 µm are usually obtained [153]. This carbonyl iron powder might serve as feedstock material for the powder-based additive manufactured techniques discussed in Section 4.6.3.

CVD is a promising manufacturing process on the lunar surface. This flexible technique could produce complex thin geometries and repetitive lunar infrastructure components. However, its TRL with respect to the production of iron parts with a thickness greater than a few microns is still low even in terrestrial environments. Its combination with the Carbonyl process enables the recovery of carbonyl iron from one of the most studied ISRU oxygen extraction methods, the ilmenite reduction with hydrogen. Moreover, the thermal decomposition of $Fe(CO)_5$ can also yield iron powders. Their combination with additive manufactured techniques returns highly flexible ISRU manufacturing processes.

It must be noted that similar to the carbonylation case, CVD might require consumables, such as ammonia, water vapor, carbon dioxide, or hydrogen, to accelerate the kinetics of the dissociation reaction.

4.6.2 Extrusion

Extrusion involves pushing bulk material through a die to produce shapes with uniform cross-sections through plastic deformation. Extrusion shall be easily adaptable to space operation [147].

Cold forward or backward extrusion occurs at environment temperature. For this process, ductile feedstock materials are required due to the strong plastic deformations they must endure. Hot extrusion might be applicable when brittle feedstock materials are considered. Hot extrusion occurs at temperatures higher than the recrystallization temperature of the feedstock materials, preventing them from hardening. In this case, aluminum is usually shaped between 650 K and 800 K. Iron requires higher temperatures between 1500 K and 1600 K. Therefore, hot extrusion methods need a significantly high thermal energy input. Hydrostatic methods use a fluid instead of a punch to exert pressure on the bulk material. This process improves formability as crack formation is deferred to higher strains [162]. Brittle materials could also be shaped through hydrostatic extrusion techniques.

Extrusion methods capable of shaping ductile and brittle feedstock materials are promising manufacturing processes on the lunar surface. Although the process equipment is highly rigid with respect to the variety of shapes that can be manufactured, it can efficiently produce repetitive lunar infrastructure components. Dies, which must be initially brought from Earth, are usually designed to shape unique geometries. Pipes and tubes could be easily produced by this method. A tube bender could subsequently modify the shape of the tubes. Feedstock for wire-based additive manufacturing could also be produced by extrusion. However, the production of thin components must be avoided if brittle materials are considered [163].

4.6.3 Additive Manufacturing

Additive Manufacturing (AM), also known as 3D printing, involves the manufacturing of three-dimensional parts by adding successive layers of material. In the last years, the introduction of AM as a standard manufacturing technique in the space industry, combined with the increasing interest in indigenous resources to enable long-term space exploration, led to several studies focused on developing AM, in particular, considering regolith as feedstock material [164, 163, 165]. Recent AM reviews discuss the feedstock materials, methods, and challenges [166], summarize the state of the art with respect to the space industry [167], and investigate its possible utilization to produce regolith-based lunar infrastructure [165]. Moreover, frameworks have been developed to adapt existing AM industrial standards to the ISRU field [168].

AM is a highly flexible manufacturing technique that can produce a wide variety of complex geometrical shapes. Its use is expected to be essential during the initial stages of space exploration, where a high level of adaptability might be required. CNC machining could potentially produce similar geometries to AM techniques. larger amounts of material shall be lost during the manufacturing process, and its recycling shall be more energy-consuming.

Two main AM categories can be distinguished with respect to the type of feedstock. Powder-based and wire-based additive manufacturing techniques are discussed in Sections 4.6.3.1 and 4.6.3.2, respectively.

4.6.3.1 Powder-based Additive Manufacturing

Powder-based additive manufacturing involves fusing layers of fine-grained compact powders with a laser beam [166]. Selective Laser Sintering (SLS) and Selective Laser Melting (SLM) have been proposed as suitable powder-based AM techniques for ISRU feedstocks [4, 165]. The SLS sintering temperature (1200-1600 K for Fe) shall be considerably lower than the SLM melting temperature (1800 K for Fe) [4]. However, a higher manufacturing temperature also returns superior mechanical properties [166].

Powder size distribution and compact packing determine the density of the manufactured part, which significantly influences its final properties [166]. For SLS/M techniques, particles shall be sieved down to $<$50 µm [165].

As discussed in Section 4.6.1, carbonyl iron powders shall be a suitable feedstock for powder-based AM techniques. The metallic alloys produced by the FFC-Cambridge process are also in granular form. Therefore, they could be combined with powder-based AM techniques to manufacture on-site [4]. A previous crushing and sieving step might be included to improve the quality of the granular material. The ISRU materials that are liquid after their refinement could be atomized to produce powders. However, the feasibility of powder atomization as an ISRU process is still unclear. Traditional atomization techniques use high-energy jets of gas or liquid to disintegrate and cool down metal droplets. However, similar to the beneficiation stage, fluid processing is challenging on the lunar surface.

Although powder-based AM techniques are likely unsuitable for µg environments, these methods show significant potential for ISRU manufacturing on the lunar surface [168].

4.6.3.2 Wire-based Additive Manufacturing

Direct Energy Deposition (DED) is the most common metal additive manufacturing technique for wire-based feedstocks. The principal difference between DED and SLM/S is that the feedstock material is melted before its deposition, requiring no powder bed [166]. Electron Beam Additive Manufacturing (EBAM) is a kind of DED method in which the laser is replaced by an electron beam, increasing the energy efficiency of the manufacturing process [4].

Wire-based AM techniques on the lunar surface would require the production of feedstock filaments from ISRU materials. The typical AM wire diameter is considerably low, in the order of 1 mm. Therefore, brittle materials must be avoided [163]. As discussed in Section 4.6.2, feedstock filaments for wire-based AM techniques could be produced by extrusion from ISRU refined materials that are molten after the metal processing stage.

4.6.4 Casting

Casting involves pouring liquid metal into a mold and allowing it to solidify. Casting on the lunar surface would incur operational challenges compared to its terrestrial equivalent. Under a lunar atmospheric pressure of 10^{-15} bar, iron vaporizes at 1200 K, lower

than its melting point of 1811 K. Aluminum also vaporizes under 10^{-15} bar at 800 K, lower than its melting point of 933 K. Therefore, a pressurized casting environment is required to avoid the direct sublimation of the feedstock metals. This fact increases the operational complexity of the overall process. Moreover, reduced lunar gravity shall slightly influence the solidification mechanisms and end-product microstructures.

Similar to the refining process discussed in Section 4.5.2, casting would require high energy input to bring metals to a molten state. However, most of the refined materials discussed in Section 4.5 are liquid at the end of the metal processing stage. Molten Fe-Si alloys produced in an MRE assembly, melt-refined iron, or distilled aluminum could be cast directly without additional energy input.

Casting is particularly convenient for complex geometries. If parts must be manufactured several times, permanent molds might be required. These molds could be produced on-site by additive manufacturing techniques. However, if indigenous metals, such as Fe, are used for the permanent molds, the casting feedstock might be restricted to aluminum, since its melting temperature is significantly lower than that of iron. Permanent molds could also be brought directly from Earth. Although it would greatly affect the process flexibility and increase the mass that must be transported to the lunar surface, a wider selection of feedstock materials could be used, and higher precision parts could be manufactured.

If a part is rarely manufactured multiple times, sand casting might be applicable. Sand casting methods use green sands, binders, and industrial additives to produce unreusable molds from patterns. Patterns could be produced on-site by additive manufacturing techniques. Baasch et al. [143] investigated the possibility of using lunar regolith as a substitute material for sand casting molds. For a deeper understanding of their experimental results, the reader is directed to their work. However, in the following paragraphs, the most relevant findings are summarized.

Since industrial additives cannot be recycled, and, therefore, must be brought from Earth, the physical properties of lunar regolith were analyzed to increase the cohesion of the mold particles without using additional binders. However, the particle cohesion reached through compressive pressure was proved to be insufficient to produce reliable molds. Regolith was then sintered at temperatures close to 1350 K to increase its tensile strength. The sintered molds had to be preheated at 773 K to avoid crack formation due to the thermal shock when pouring molten metals. This sintering step would significantly increase the necessary energy input of the overall casting process.

The regolith castings returned surface qualities close to the ones achieved with industrial green sands. Nevertheless, the mineral composition and sharp particle edges limited the wetting ability of the mold, preventing the casting of fine structures. Fine structures could be added in a post-processing stage through CNC machining.

Sand casting methods that use sintered regolith as mold material are a promising manufacturing process on the lunar surface. This flexible technique does not require consumables brought from Earth. It can directly take advantage of the molten state of the refined materials after the oxygen extraction and metal refining stages to produce

large and diverse complex geometries. The required pressurized environment of the oxygen extraction and metal refining stages can be extended to the casting infrastructure. However, to ensure the quality of the end products, supplementary manufacturing processes have to be included. FDM 3D printers could easily produce the necessary patterns. CNC machining could generate fine structures in the casted parts.

5 Material Characterization

In this chapter, the metals yielded by the ISRU processes described in Chapter 4 are characterized with respect to their mechanical and thermal properties. Estimates for the yield strength and thermal conductivity are found when possible. The ductility of the metals is also qualitatively discussed. Carbonyl and melt-refined irons, Fe-Si alloys, distilled aluminum, and heterogeneous highlands metallic mixtures can be obtained.

Materials science studies the properties of solid materials and how these properties are determined by their composition and structure. Understanding the composition and structure of materials is usually done by experimental analyses of samples. However, the actual composition of the regolith feedstock is highly uncertain as it has only been inferred from samples taken by the Apollo and Luna programs as well as from remote-sensing missions [45]. Moreover, numerous unknowns still exist regarding the ISRU technologies that will be involved in the early exploration stages of the lunar surface. Most of them are currently under development and rely on lunar regolith simulants to understand their operation. When laboratory experiments are carried out on these processes and simulants, they are performed under controlled terrestrial environments, which might not represent the conditions met at large-scale lunar facilities. If analogies are drawn with already existing Earth processes, it must be highlighted that the technological resources available on the Moon might differ significantly from those obtainable on Earth, and, therefore, the material refining capabilities and purity levels might be considerably reduced.

The values given in the following sections are simple estimates of the possible ranges of specific material properties based on the currently existing information for lunar resources and ISRU processes. When available, values have been taken from previous studies or derived from numerical and analytical models. The assumptions made, as well as the absolute values, can considerably deviate from reality. However, the relative differences between the material properties might be reasonable to evaluate the concepts and draw conclusions about the most promising ISRU process chains.

As a last remark, it must be noted that every ISRU process chain stage influences the material properties of the end product. The main drivers are those processes that influence the end product final composition or microstructure, such as the regolith feedstock composition, the degree and type of beneficiation, the operational conditions of the oxygen extraction processes (e.g., the operating temperature, the chemical reactions involved, or the material phase changes present), the achievable degree of refinement of the metal processing stage, or the microstructure changes provoked by the different manufacturing processes. Therefore, to completely understand the properties of on-site produced materials, these factors must be thoroughly investigated in the future.

5.1 Carbonyl Iron

Ilmenite reduction with hydrogen yields iron as a refined material after the metal processing stage of the ISRU process chain. In this case, the iron is extracted from reduced ilmenite by the Carbonyl process.

Pure iron usually has a purity level >99.98 wt.%, where the remaining 0.02 wt.% is composed of small amounts of carbon, nitrogen, oxygen, and other metallic and non-metallic impurities. The mechanical properties of pure iron are highly sensitive to its purity level. The yield strength and ductility decrease with increasing material purity. For commercial pure iron (Fe>99.98 wt.%), the yield strength at ambient temperature is 215±30 MPa, while for ultra-high-purity iron (Fe>99.99998 wt.%), this value is almost quartered (60±40 MPa) [169]. The iron thermal properties remain nearly constant for high purity levels. In particular, the thermal conductivity is close to 78.5 W/(m·K) at ambient temperature [170, 171].

Carbonyl iron belongs to this group of high-purity irons. As this iron is formed from the decomposition of iron pentacarbonyl ($Fe(CO)_5$), carbon and oxygen are common impurities present in the metal. Its carbon concentration is usually lower than 0.26 wt.% (1.2 at.%). If ammonia gas is introduced during the Carbonyl process to limit the formation of CO_2, Fe_3C, and FeO, the carbon content can be further reduced to 0.16 wt.% (0.7 at.%) [172]. However, adding ammonia might encourage the formation of FeN, increasing the nitrogen content in the iron up to 0.25 wt.% (0.9 at.%) [153]. Oxygen at 0.09 wt.% (0.3 at.%) content is also typically present in carbonyl iron [153, 173]. These typical carbon, nitrogen, and oxygen contents produce iron with a purity level >99.50 wt.%.

The lower purity level of carbonyl iron compared to commercial pure iron means a higher yield strength and a lower thermal conductivity. For this analysis, the mechanical properties are obtained from the values provided by Lin and German [174]. For a 0.2 wt.% C content, the yield strength is 240 MPa at ambient temperature. The 0.2 wt.% C content is similar to those of traditional structural steels used for terrestrial applications, which also require good ductility together with high mechanical strength [175].

To determine the thermal conductivity, the model proposed by Helsing and Grimvall [170] has been used. Iron with 0.2 wt.% C content composed of a mixture of pure ferrite and pearlite is assumed. Ferrite accounts for a volume fraction of ∼0.75 and has a thermal conductivity of 78.5 W/(m·K). Pearlite (0.8 wt.% C) accounts for a volume fraction of ∼0.25 and has a thermal conductivity of 57.8 W/(m·K). The thermal conductivity of pearlite has been calculated considering a pearlite composition of pure ferrite (0.88 volume fraction) and cementite (0.12 volume fraction). The thermal conductivity of cementite is 8 W/(m·K). No impurities or additional alloying elements dissolved in the ferrite have been considered. Under these assumptions, the thermal conductivity of iron with 0.2 wt.% C content is estimated to be 73 W/(m·K) at the radiator working temperature.

Nickel can also be extracted from lunar regolith as nickel tetracarbonyl ($Ni(CO)_4$) by the Carbonyl process. The average concentration of Ni in lunar soils is expected to be ap-

proximately 0.03 wt.% (see Chapter 3). Therefore, to use nickel as an alloying element of iron, large amounts of regolith must be processed. However, once processed, the metals might be easily alloyed by combining the $Fe(CO)_5$ and $Ni(CO)_4$ gas streams. Although nickel might modify the material properties of iron, the influence of Ni as an alloying element is not discussed in this work.

5.2 Melt-refined Iron

Ilmenite reduction with hydrogen also yields iron as a refined material after the metal processing stage of the ISRU process chain. In this case, the iron is extracted from reduced ilmenite via melting and metal-oxide phase separation.

As already discussed in Section 4.5.2, the melting and refining approach is relatively unstudied in the literature. Therefore, several assumptions have been made to estimate the order of magnitude of the mechanical and thermal properties of melt-refined iron. The Fe composition after the metal-oxide phase separation is highly uncertain. Berggren [155] shared that laboratory tests conducted on reduced regolith simulants returned iron purity levels $>$98.5 wt.%. In these studies, no additional reagent fluxes or purification steps other than a metal-oxide phase separation were taken. It must be noted that before the metal processing stage, the solid byproduct is mainly composed of a mixture of TiO_2, Fe, unreacted $FeTiO_3$, and unreduced regolith. Consequently, the remaining 1.5 wt.% content of the refined metal would most likely contain oxide inclusions.

Oxide inclusions deteriorate the mechanical properties of iron, reducing its strength and ductility. The effect depends on their content, morphology, and distribution within the metallic matrix [175]. Melt-refined irons are expected to have a brittle behavior and a extremely low elastic strength. As a first-order approximation, melt-refined irons might behave analog to Fe-Si alloys with high silicon contents. For these alloys, the yield strength cannot be measured due to its excessively brittle behavior (see Section 5.3).

The thermal conductivity of the refined iron has been estimated using the analytical model developed by Wang and Li [171], which considers the effect of alloying elements dissolved in ferrite. No model has been found in the literature to account for the effect of oxide inclusions. As a first-order approximation, the refined iron is considered to be a pure ferritic matrix with 1.5 wt.% Si dissolved. Silicon is the alloying element that more impacts the thermal conductivity of ferrite and might have a similar effect to the oxide inclusions. Under this assumption, the model returns a thermal conductivity close to 34 W/(m·K) at the radiator working temperature, which is significantly lower than the thermal conductivity of pure iron ($\sim$78.5 W/(m·K)).

Melt-refined Fe has a lower purity level than carbonyl iron. If the correct alloying elements are added, a lower purity level shall return better mechanical properties and worse thermal properties. However, it is not the case for melt-refined iron due to existing oxide inclusions in the Fe matrix. The existing oxide inclusions do not only reduce the thermal conductivity but also the ductility and strength.

5.3 Fe-Si Alloy

Ferrosilicon (Fe-Si) alloys can be obtained as a byproduct after the molten regolith electrolysis stage of the ISRU process chain. While FeO is electrolyzed almost entirely, the amount of the reduced SiO_2 can be controlled via the operating temperature of the MRE reactor (see Section 4.4.2). Therefore, Fe-Si alloys with specific Si contents can be directly obtained during the oxygen extraction process.

Silicon usually appears dissolved in the ferrite for alloys with low Si content. In this case, the alloying element tends to harden the ferrite, increasing its strength while reducing its ductility [175]. The thermal properties are also significantly influenced by the presence of alloying elements. In particular, silicon strongly reduces the thermal conductivity of ferrite [171].

The alloys are expected to be extruded to manufacture either wire feedstock for additive manufacturing purposes or tubes that must be bent afterwards to assemble the tubular radiator concept (see Chapter 6). For these reasons, ductile materials are required. Grossman et al. [163] characterized the mechanical properties of various ferrosilicon samples with a composition ranging from pure iron to 12 wt.% Si. The samples with a silicon content $>$6 wt.% were too brittle and ruptured at low strain values. This statement agrees with other works on ferrosilicon alloys that set the ductile-to-brittle transition at 4.7-5.8 wt.% (9-11 at.%) Si [176]. Moreover, traditional structural steels used for terrestrial applications, which also require a trade-off between strength and ductility, have Si contents $<$1 wt.% [175].

For a TCS radiator, high thermal conductivities are desirable to increase the amount of released heat to the environment. Lunar surface radiators are not subject to particularly high mechanical stresses, and, therefore, their strength shall not be a driving factor when selecting the material. Furthermore, ductile materials are beneficial during the manufacturing and assembly processes. These facts encourage the selection of an alloy with the lowest Si content possible. However, to allow an easy extraction process from the MRE reactor, metallic iron shall also preferably be in a molten state during the electrolysis. Therefore, a reactor temperature higher than 1800 K would be required. In this case, not only FeO but also SiO_2 would be reduced (see Figure 4–7). Consequently, the presence of dissolved Si in the metallic byproduct cannot be avoided. Although ideally, oxides species are discretely reduced in the order of increasingly negative Gibbs free energy, when their concentration decreases, they will no longer be preferentially reduced in favor of more abundant species [18]. For this reason, total avoidance of other electrolyzed oxides present in lunar regolith might be impossible. A small presence of oxide and metallic inclusions, such as Al or Ti, shall be expected in the Fe-Si alloys [177].

Grossman et al. [163] establish an upper limit of 3 wt.% Si in ferrosilicon alloys used as wire feedstock for additive manufacturing. For this upper limit, yield strengths of 153.7$\pm$3.4 MPa are reported. These values, lower than the reported yield strength of pure iron (200.0$\pm$73.8 MPa), disagree with the expected strengthening character of Si. Using the highlands regolith model of Schreiner et al. [18], a maximum liquidus temperature of 1700 K shall be reached for 3 wt.% Si content, yielding only 0.07 kg

of O_2 per kg of highlands regolith (see Table Tables 3–2 and 3–3 and Figure 4–7). However, to maintain Fe in a molten state, 1800 K are required. A reactor temperature of 1800 K would yield 0.11 kg of O_2 per kg of highlands regolith and a Si content of 17 wt.%, significantly higher than the required 3 wt.%. To maintain the Si content close to the desired range, Fe, which is reduced first and accumulates at the bottom of the reactor [177], must be continuously removed before the total reduction of silicon.

It must be noted that the yield strength values reported by Grossman et al. [163] correspond to pure Fe-Si alloys with almost no presence of other elements. As already discussed, the purity level of ferrosilicon alloys produced on the lunar surface shall be lower due to the existence of oxide slag impurities and metal inclusions. If these impurities are not completely removed in a subsequent metal processing stage, they might impact the mechanical properties of the alloy. They would further reduce the material ductility, allowing a lower silicon content, and hindering the extraction operations.

The analytical model developed by Wang and Li [171] has been used to estimate the thermal conductivity of the alloys. The model predicts the effect of dissolved alloying elements and temperature on the thermal conductivity of ferrite applying the theory of metal heat conduction. As discussed in Section 5.1, the thermal conductivity of pure iron is 78.5 W/(m·K) at ambient temperature. However, when the silicon content increases to 3 wt.%, the thermal conductivity drops to 23 W/(m·K). As the silicon content drastically reduces the thermal conductivity of the ferrite, the effect of other alloy elements and impurities can be neglected.

5.4 Highlands Metallic Mixture

Molten salt electrolysis yields a heterogeneous metallic mixture as a byproduct after the oxygen extraction from highlands regolith. MSE is able to produce powdered metallic byproducts with low oxygen contents. In Section 4.4.3, an O_2 concentration of 0.6 wt.% was considered.

Lomax et al. [130] performed experiments of the FFC-Cambridge process using JSC-2A lunar regolith simulant. JSC-2A lunar regolith simulant is a replica of the previous simulant version JSC-1A [137]. In these tests, three principal alloys dominated the metallic byproduct: an Al-Fe alloy, usually including Si; a Ca-Si-Al alloy, sometimes with the inclusion of Mg; and a Fe-Si alloy that regularly contained Ti and Al [130]. Moreover, the metallic byproduct appeared to be depleted of silicon and magnesium, relative to the amount of these elements present in the starting JSC-2A simulant. Although Si accounted for approximately 40 wt.% of the metallic elements in JSC-2A, only $\sim$20 wt.% Si could be found in the solid byproduct after the electrolysis [130].

Pure metals and alloy powders can be gained from the FFC-Cambridge process [104]. However, if the highlands regolith feedstock is not previously beneficiated, heterogeneous metallic mixtures composed of multiple alloys are obtained. Table 3–3 shows the average element composition of highlands regolith. When oxygen is recovered from the regolith, and no Si and Mg depletion are considered, a metallic byproduct rich in Si ($\sim$38 wt.%), Al ($\sim$24 wt.%) and Ca ($\sim$19 wt.%), and with significant amounts of

Fe (∼9 wt.%) and Mg (∼8 wt.%) can be expected. The metallic mixture would have anisotropic mechanical and thermal properties.

It is impossible to predict these anisotropic properties without further experimental analyses. However, some conclusions can be drawn from the expected material composition. The metal byproduct shall have an extremely brittle behavior due to three principal reasons. The heterogeneity of the mixture might affect the internal cohesion of the grains. The large amount of silicon present in the material significantly reduces the achievable ductility (see Section 5.3). 0.6 wt.% O_2 would be present in the form of oxide inclusions, which would further deteriorate the mechanical properties (see Section 5.2). Therefore, the metallic byproduct would lack elastic behavior and have a significantly reduced plastic character, which would restrict the manufacturing techniques that could be used.

The thermal conductivity strongly depends on the purity level of the material. Heterogeneous anisotropic materials shall have a significantly lower thermal conductivity than their pure components. For instance, adding aluminum to an iron matrix reduces the overall thermal conductivity even if the thermal conductivity of Al is superior to the one of Fe [171]. As a first-order approximation, the thermal conductivity of the highlands metallic mixture is considered 15 W/(m·K) for the simulations performed in Chapter 7. 15 W/(m·K) might be close to the thermal conductivity of high alloy steels.

Although the material properties of highlands metallic mixtures shall be inferior to those obtained from other ISRU processes, this material concept does not require a metal processing stage, saving infrastructure and simplifying the overall process chain. The metallic byproduct might be directly used for manufacturing purposes after the oxygen extraction stage. If beneficiation and metal processing stages are added to the molten salt electrolysis, specific metals with superior material properties, such as the one discussed in Section 5.5, could be recovered.

5.5 Distilled Aluminum

As discussed in Section 4.5.3, aluminum can be obtained through vacuum distillation after the molten salt electrolysis of unbeneficiated highlands regolith or anorthite-rich regolith. Aluminum is a frequent material used for space applications due to its satisfactory combination of lightweight mechanical and thermal properties. If an anorthite-rich feedstock is considered, the composition of the MSE byproduct is simplified to a Si (40.5 wt.%), Al (31 wt.%), and Ca (28.5 wt.%) alloy. However, as already discussed in Section 4.5.3, small amounts of Fe, Mg, minor regolith elements, and unreduced oxides can also be expected.

The first step of the vacuum distillation process, where calcium is separated from the Ca-Al-Si alloy, occurs at 1100 K. At 1100 K, the vapor pressure of Ca is six orders of magnitude higher than the vapor pressure of Al and almost ten orders of magnitude higher than the vapor pressure of Si [65]. Although no MIVM has been developed to specifically calculate the separation degree of the Ca-Al-Si alloy, calcium could be easily depleted from the metallic mixture due to the high vapor pressure differences.

For the vacuum distillation of aluminum from a Si-Fe-Al alloy, Liu et al. [157] report that, when the vapor pressure of Al is three orders of magnitude higher than the vapor pressure of Fe and four orders of magnitude higher than the vapor pressure of Si, only 0.6 wt.% of Fe and Si, at an aluminum concentration of 7 wt.% in the residual phase, are lost during the distillation of aluminum. As the vapor pressure differences of the Ca-Al-Si alloy are more than two times higher than the vapor pressure differences of the Si-Fe-Al, the amount of Al and Si lost during the total separation of calcium shall be insignificant. Therefore, an Al-Si alloy with an initial composition of 56.5 wt.% of Si and 43.5 wt.% of Al can be assumed for the second step of the vacuum distillation process.

The second step of the vacuum distillation process, where aluminum is separated from the Al-Si alloy, occurs at 1800 K. At 1800 K, the vapor pressure of Al is only two orders of magnitude higher than the vapor pressure of Si [65]. To estimate the purity level of distilled aluminum, the molecular interaction volume model developed by Liu et al. [158] for Al-Si alloys and the experimental results reported by Wei et al. [178] have been used. For the aluminum recovery rate of 90 wt.% discussed in Section 4.5.3, an Al concentration of 7.35 wt.% would remain in the residual phase. The gas phase would be composed of Al (96 wt.%) and Si (4 wt.%). If a higher recovery rate was desired, the silicon content would increase in the gas phase. For an aluminum recovery rate of 99 wt.%, the gas phase would be composed of Al (75 wt.%) and Si (25 wt.%). However, if a distilled aluminum purity level of 99.5 wt.%, close to the purity level of commercially pure Al, was desired, the aluminum recovery rate would decrease to 13 wt.%. The reported recovery rates and purity levels are calculated for a single-pass vacuum distillation process. If simultaneously high aluminum purity levels and recovery rates were desired, multiple distillation passes would be necessary. Multiple sequential passes increase the overall energy consumption and processing time.

The MIVM model used for the Al-Si alloy [158] could be expanded to account for additional elements, such as Fe, that are also present in the metallic mixture [157].

As a reasonably large amount of Si is expected to be found in the distilled aluminum, its alloying effect on the mechanical and thermal properties must be investigated. Silicon tends to harden Al, increasing its strength while reducing its ductility. For this analysis, the mechanical properties are obtained from the values provided by Kalhapure and Dighe [179]. The yield strength of the recovered Al-Si alloy with 4 wt.% of Si would be close to 20 MPa. For silicon contents of 14 wt.%, the yield strength would increase over 80 MPa. However, the elongation would reduce from 65%, at 4 wt.% Si, to 10%, at 14 wt.% Si.

The thermal conductivity of the recovered Al-Si alloy with 4 wt.% of Si is estimated from the values reported in the literature for alloys with a similar composition. A thermal conductivity of 190 W/(m·K) is considered [180].

Additional alloying elements that might be present in the initial MSE byproduct and might not be entirely removed during the distillation process be shall further increase the aluminum strength and decrease the thermal conductivity of aluminum.

6 In-Situ Material Production Concepts

The single ISRU processes described in Chapter 4 can be combined together to result in in-situ material production concepts capable of manufacturing a TCS radiator. A systematic approach is followed to select the most suitable combinations of processes.

First, as discussed in Section 4.4, processes capable of yielding metallic byproducts are identified from the existing ISRU O_2 extraction techniques. These processes are the ilmenite reduction with hydrogen, molten regolith electrolysis, and molten salt electrolysis. Afterwards, the regolith composition close to the location of the reference mission is studied. For the ilmenite reduction with hydrogen, a previous beneficiation stage is necessary. For the other two O_2 extraction techniques, beneficiation stages could potentially increase the refinement level of the metallic byproduct. In particular, anorthite shall be abundant close to the location of the reference mission and would significantly improve the refinement level of the MSE byproduct. A single excavation concept, RASSOR, is considered to account for the excavation rates that depend on the beneficiation and O_2 extraction processes.

In parallel, the radiator concepts discussed in Section 2.3.1 are investigated. Possible ISRU manufacturing processes are defined for the state-of-the-art and tubular radiators. Due to the complexity of the state-of-the-art radiator geometry, only powder-based and wire-based additive manufacturing techniques are found to be feasible for its production on the lunar surface. However, extrusion and chemical vapor deposition could potentially manufacture the required pipes for the tubular radiators. Additive manufacturing and casting would also be necessary to produce complex geometries, such as tube joints.

Finally, the necessary stages to link the metallic byproducts to the manufacturing processes are determined. To this end, the manufacturing requirements are defined. For instance, powder-based additive manufacturing requires fine metallic powder as feedstock, whereas wire-based additive manufacturing requires thin metallic wires. The metallic byproducts are refined at the metal processing stage to improve their material properties and purity levels. This operation is particularly relevant after the ilmenite reduction with hydrogen. In this case, carbonylation, and melting and refining can separate iron from the slag. The other two O_2 extraction techniques might directly yield suitable materials, such as Fe-Si alloys or highlands metallic mixtures. However, metal processing techniques, such as vacuum distillation, can be included to improve the properties of the output material.

After manufacturing the radiator structure, the concepts pass through a post-processing stage, where the Z-93 white paint coating is applied.

Figure 6–1 represents the workflow followed to define the overall in-situ material production concepts based on the facts and restrictions discussed above. The workflow is subdivided into three steps. In the first step, for each ISRU O_2 extraction technique, the upstream process chain stages are defined. In the second step, for each radiator

concept, the manufacturing stage is determined. In the third step, the metal processing and output materials are specified based on steps 1 and 2. Moreover, the partial production concepts generated in steps 1 and 2 are combined together and tagged as accepted or rejected.

Once the overall production concepts are obtained, they are compared one to one for each radiator design. As the manufacturing stage is not studied in terms of mass, volume, power, and cooling requirements, the concepts are combined together into a single representative concept if only this stage differs. This operation allows the simplification of the analysis and a better evaluation of the results presented in Chapter 8. Tables 6–1 and 6–2 show the final analyzed concepts that output state-of-the-art and tubular radiators, respectively.

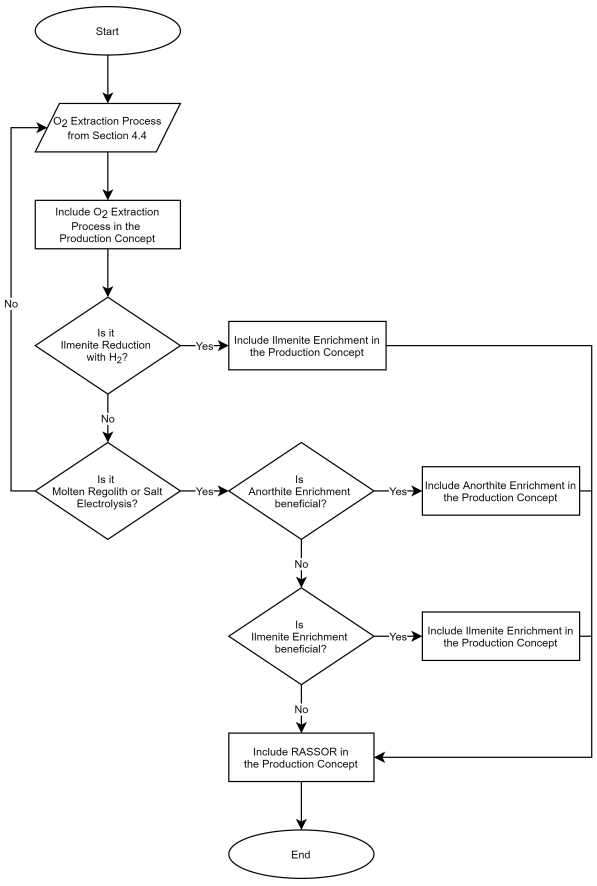

(a) Step 1.

Fig. 6–1: Flowchart of the in-situ material production concept definition.

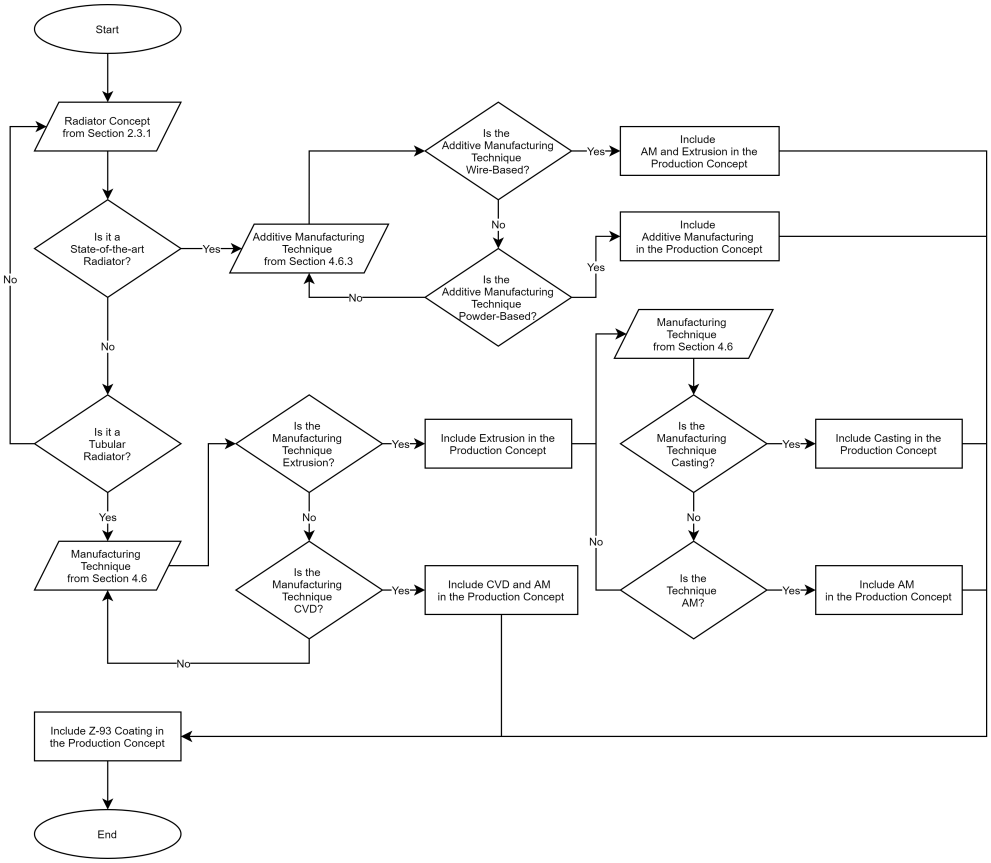

(b) Step 2.

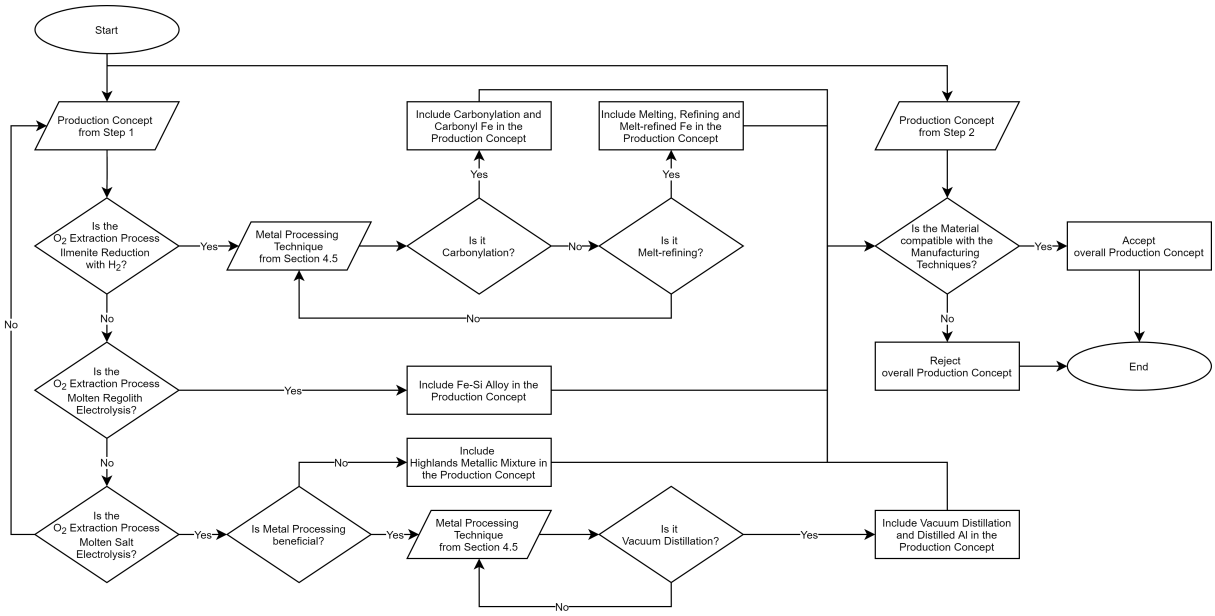

(c) Step 3.

Fig. 6–1: Flowchart of the in-situ material production concept definition (cont.).

Tab. 6–1: State-of-the-art radiator in-situ material production concepts.

	Excavation	Beneficiation	Oxygen Extraction	Metal Processing	Material	Manufacturing Preparation	Manufacturing	Post-Processing
S1	RASSOR	Ilmenite Enrichment	Ilmenite Reduction with H_2	Carbonylation	Carbonyl Fe	Chemical Decomposition	Additive Manufacturing	Z-93 Coating
S2	RASSOR	Ilmenite Enrichment	Molten Regolith Electrolysis	-	Fe-Si Alloy	Extrusion	Additive Manufacturing	Z-93 Coating
S3	RASSOR	Anorthite Enrichment	Molten Salt Electrolysis	Vacuum Distillation	Distilled Al	Extrusion	Additive Manufacturing	Z-93 Coating
S4	RASSOR	-	Molten Salt Electrolysis	-	Highlands Metallic Mixture	-	Additive Manufacturing	Z-93 Coating

Tab. 6–2: Tubular radiator in-situ material production concepts.

	Excavation	Beneficiation	Oxygen Extraction	Metal Processing	Material	Manufacturing Preparation	Manufacturing	Post-Processing
T1	RASSOR	Ilmenite Enrichment	Ilmenite Reduction with H_2	Carbonylation	Carbonyl Fe	Chemical Decomposition	CVD and Additive Manufacturing	Z-93 Coating
T2	RASSOR	Ilmenite Enrichment	Molten Regolith Electrolysis	-	Fe-Si Alloy	-	Extrusion and Casting	Z-93 Coating
T3	RASSOR	Anorthite Enrichment	Molten Salt Electrolysis	Vacuum Distillation	Distilled Al	-	Extrusion and Casting	Z-93 Coating
T4	RASSOR	Ilmenite Enrichment	Ilmenite Reduction with H_2	Melting and Refining	Melt-refined Fe	-	Extrusion and Casting	Z-93 Coating

A thorough description of the concepts presented in Tables 6–1 and 6–2 can be found in the following sections.

6.1 Concepts S1 and T1

The concepts S1 and T1 share the ISRU process chain until the manufacturing stage. Multiple RASSORs excavate regolith in the vicinity of the lunar surface reference mission. The regolith is likely to be highlands regolith with an abnormally high concentration of iron oxide.

This regolith is beneficiated to obtain ilmenite-rich feedstock. In the ilmenite enrichment assembly, the regolith passes through particle size, magnetic, and electrostatic separators to reach 80 wt.% of $FeTiO_3$.

The beneficiated feedstock is introduced into a hydrogen reduction assembly to produce 15 t/y of O_2. Ilmenite-rich regolith is heated to 1000 K in a fluidized bed reactor. Hydrogen, which reacts with $FeTiO_3$ to produce water vapor, metallic Fe, and TiO_2, is also introduced into the reactor. The exhaust gas stream passes through a cyclone unit and a water purification unit, which separate H_2O from H_2 and dust. Water is split into hydrogen and oxygen in a static feed water electrolyzer. Hydrogen is recirculated to the reactor, and oxygen is stored for life support or propellant production.

The remaining metallic Fe, TiO_2, and slag are introduced into a carbonylation assembly. At 400 K and 70 bar, carbon monoxide reacts with metallic Fe in a fluidized bed reactor producing iron pentacarbonyl. CO is generated in a solid oxide electrolysis cell from the CO_2 supplied by the crew. NH_3 and H_2S are added to accelerate the kinetics of the carbonyl reaction. $Fe(CO)_5$ is condensed in a CHX to separate it from the exhaust gas stream. In the reactor, TiO_2-rich slag remains.

At this point, the concepts S1 and T1 deviate from each other. In concept S1, iron pentacarbonyl is chemically decomposed into carbonyl Fe powder and carbon monoxide at 500 K. CO is recirculated to the carbonylation assembly. Powder-based additive manufacturing techniques use carbonyl Fe powder as feedstock to produce all the necessary parts of a state-of-the-art radiator.

In concept T1, the necessary pipes of the tubular radiator are manufactured by chemical vapor deposition of $Fe(CO)_5$. Iron is separated from CO and deposited, at 475 K, in layers on bent tubular forms. The dissociated CO is recirculated to the carbonylation assembly. Some iron pentacarbonyl is chemically decomposed into carbonyl Fe powder and used as additive manufacturing feedstock to produce radiator parts with complex geometries. Finally, both concepts are coated with Z-93 white paint brought from Earth.

6.2 Concepts S2 and T2

The concepts S2 and T2 share the ISRU process chain until the manufacturing stage. Multiple RASSORs excavate regolith in the vicinity of the lunar surface reference mission. The regolith is likely to be highlands regolith with an abnormally high concentration of iron oxide.

This regolith is beneficiated to increase its iron concentration, which would yield a higher amount of iron alloys after the oxygen extraction process. In the FeO enrichment assembly, the regolith passes through particle size, magnetic, and electrostatic separators to reach 20 wt.% of FeO.

The beneficiated feedstock is introduced into a molten regolith electrolysis assembly and heated to 2254 K to produce 15 t/y of O_2. Diatomic oxygen is generated at the inert anode, whereas molten metals start to accumulate at the cathode. At 1800 K, the molten metals begin to be extracted from the electrolysis cell. At this temperature, ferrosilicon alloys are directly recoverable. Oxygen gas exhausts the reactor and passes through an oxygen purification unit and a heat exchanger before being stored for life support or propellant production.

At this point, the concepts S2 and T2 deviate from each other. In concept S2, Fe-Si alloys, with a silicon content $<$3 wt.% to avoid a brittle behavior, are extruded to generate wire feedstock. Wire-based additive manufacturing techniques use this feedstock to produce all the necessary parts of a state-of-the-art radiator.

In concept T2, the necessary pipes of the tubular radiator are extruded. The Fe-Si alloys with a silicon content $<$3 wt.% allow subsequent tube bending. Casting is used to produce radiator parts with complex geometries. Finally, both concepts are coated with Z-93 white paint brought from Earth.

6.3 Concepts S3 and T3

The concepts S3 and T3 share the ISRU process chain until the manufacturing stage. Multiple RASSORs excavate regolith in the vicinity of the lunar surface reference mis-

sion. The expected highlands regolith shall contain abundant plagioclase feldspar minerals, such as anorthite.

This regolith is beneficiated to obtain $CaAl_2Si_2O_8$-rich feedstock. In the anorthite enrichment assembly, the regolith passes through particle size and magnetic separators to reach 90 wt.% of $CaAl_2Si_2O_8$.

The beneficiated feedstock is preheated to 1223 K and subsequently introduced into a molten salt electrolysis assembly to produce 15 t/y of O_2. The molten salt electrolysis assembly is composed of an inert anode, a molten $CaCl_2$ electrolyte, and a cathode basket, where the anorthite-rich regolith is placed. Diatomic oxygen is generated at the inert anode, whereas metallic alloys begin to form at the cathode. Due to the feedstock composition, Ca-Al-Si is the principal alloy. Oxygen exhausts the reactor and passes through an oxygen purification unit before being stored for life support or propellant production.

The remaining Ca-Al-Si-rich alloys are introduced into a vacuum distillation assembly. At 1100 K and 10^{-3} bar, calcium vaporizes inside the distillation container. The gas is constantly removed and vented to the lunar environment to maintain the operating pressure inside the container. Once Ca has been depleted, the temperature increases to 1800 K. At this point, aluminum vaporizes. Some silicon is expected to also vaporize at 1800 K and 10^{-3} bar. A vacuum pump constantly removes the Al-rich gas from the distillation container. The gas stream passes through a condensing heat exchanger and accumulates in a condensation container. In the distillation container, a Si-rich residual product remains.

At this point, the concepts S3 and T3 deviate from each other. In concept S3, distilled Al is extruded to generate wire feedstock. Wire-based additive manufacturing techniques use this feedstock to produce all the necessary parts of a state-of-the-art radiator.

In concept T3, the necessary pipes of the tubular radiator are extruded and bent. Casting is used to produce radiator parts with complex geometries. Finally, both concepts are coated with Z-93 white paint brought from Earth.

6.4 Concept S4

In the concept S4, multiple RASSORs excavate regolith in the vicinity of the lunar surface reference mission. The regolith is likely to be highlands regolith with an abnormally high concentration of iron oxide.

This regolith is preheated to 1223 K and subsequently introduced into a molten salt electrolysis assembly to produce 15 t/y of O_2. The molten salt electrolysis assembly is composed of an inert anode, a molten $CaCl_2$ electrolyte, and a cathode basket, where the anorthite-rich regolith is placed. Diatomic oxygen is generated at the inert anode, whereas metallic alloys begin to form at the cathode. Oxygen gas exhausts the reactor and passes through an oxygen purification unit before being stored for life support or propellant production.

Due to the granular nature of the regolith feedstock, the heterogeneous highlands

metallic mixture formed in the cathode basket is also powdered. Powder-based additive manufacturing techniques use this heterogeneous highlands metallic mixture as feedstock to directly produce all the necessary parts of a state-of-the-art radiator. A previous crushing and sieving step can be included to improve the quality of the granular material entering the manufacturing stage. Finally, the concept is coated with Z-93 white paint brought from Earth.

6.5 Concept T4

In the concept T4, multiple RASSORs excavate regolith in the vicinity of the lunar surface reference mission. The regolith is likely to be highlands regolith with an abnormally high concentration of iron oxide.

This regolith is beneficiated to obtain ilmenite-rich feedstock. In the ilmenite enrichment assembly, the regolith passes through particle size, magnetic, and electrostatic separators to reach 80 wt.% of $FeTiO_3$.

The beneficiated feedstock is introduced into a hydrogen reduction assembly to produce 15 t/y of O_2. Ilmenite-rich regolith is heated to 1000 K in a fluidized bed reactor. Hydrogen, which reacts with $FeTiO_3$ to produce water vapor, metallic Fe, and TiO_2, is also introduced into the reactor. The exhaust gas stream passes through a cyclone unit and a water purification unit, which separate H_2O from H_2 and dust. Water is split into hydrogen and oxygen in a static feed water electrolyzer. Hydrogen is recirculated to the reactor, and oxygen is stored for life support or propellant production.

The remaining metallic Fe, TiO_2, and slag are introduced into a melting and refining assembly. At 1850 K, molten iron is refined through metal-oxide phase separation without using additional reagent fluxes.

Melt-refined Fe is extruded to produce the necessary pipes of the tubular radiator. Although melt-refined Fe is expected to be particularly brittle, it could be shaped using hydrostatic or high-temperature extrusion. A subsequent hot bending step is applied to the produced tubes. Casting is used to produce radiator parts with complex geometries. Finally, the concept is coated with Z-93 white paint brought from Earth.

7 Thermal Simulations

Once the in-situ production concepts have been defined and the materials characterized, three-dimensional thermal simulations are conducted on the radiator concepts described in Section 2.3.1 to quantify the heat rejected to the environment and understand which design would perform better.

Figure 7–1 represents the four analyzed configurations. The state-of-the-art and tubular radiators are elevated 30 cm above the lunar surface in Figure 7–1(a) and Figure 7–1(c), respectively. In these cases, the systems exchange heat via radiation with the lunar surface and the environment. The state-of-the-art and tubular radiators lay on the lunar surface in Figure 7–1(b) and Figure 7–1(d), respectively. In these cases, the systems primarily exchange heat through conduction with the lunar surface and radiation with the environment. In Figure 7–1(d), half of the cylindrical radiator surface is covered by regolith.

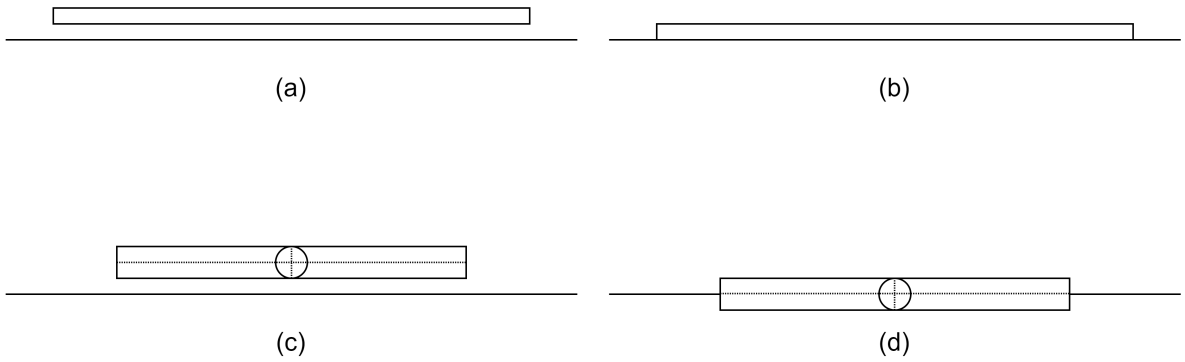

Fig. 7–1: Configurations of the thermal simulations. State-of-the-art radiator above the lunar surface (a). State-of-the-art radiator on the lunar surface (b). Tubular radiator above the lunar surface (c). Tubular radiator on the lunar surface (d).

For each configuration, a single radiator module is simulated. As already discussed in Section 2.3.1, the radiator assembly can be scaled by connecting multiple modules in parallel to meet the heat rejection requirements of the ECLSS and ISRU facility.

No vertical configuration of the state-of-the-art radiator has been simulated. Vertical radiators have been proposed for the lunar equatorial regions, where the solar incidence angle is predominantly perpendicular to the lunar surface [35, 36]. The view factor between a vertical radiator and a lunar surface shall be lower than for a horizontal radiator case. Therefore, a larger amount of heat could be radiated towards the environment. However, the solar incidence angle in the South Pole is almost parallel to the lunar surface, which would be detrimental for a vertical radiator. Even if the radiator

is located in a PSR, which never receives direct solar radiation, the radiation reflected by the lunar surface features would also be more detrimental for a vertical radiator than for a horizontal radiator. Although the reflected radiation has been neglected in the thermal simulations, it can be in the range of 5 to 10 W/m^2 [181].

Moreover, a horizontal radiator positioning would also reduce the structural stresses due to its own weight compared to a vertical radiator, enabling the use of materials with inferior mechanical properties. For these reasons, two horizontal configurations have been investigated. The structural stresses of radiator designs that lay on the lunar surface are expected to lower than for the raised designs.

The temperature fluctuations in a PSR are also relatively small compared to other regions (see Figure 2–5). Therefore, low thermal stresses are expected, reducing further the structural requirements of the TCS radiator.

7.1 Numerical Model

Coupled steady-state thermo-fluid dynamic simulations are performed with Ansys^{TM}. A CFD simulation in Ansys^{TM} Fluent is developed to model the convective heat transfer between the working fluid and the radiator structure. The calculated convective heat transfer coefficient and near-wall temperatures of the solid-fluid interface are connected to thermal simulation in Ansys^{TM} Mechanical, which models the conductive and radiative heat transfer between the radiator structure, the lunar surface, and the environment.

The 3D simulations include the radiator CAD models presented in Section 2.3.1 and a concentric cylindrical section of the lunar surface with a diameter of 25 m and a depth of 1 m.

Liquid ammonia is used as working fluid for the CFD simulations. The NH_3 properties are summarized in Table B–1 together with the rest of parameters used in the numerical models. For both radiator geometries, the flow enters the module through a supply manifold. The supply manifold is modeled as a mass flow inlet boundary condition. The ISS thermal control system has been considered to define the inlet boundary conditions. Each ISS radiator module receives 140 kg/h of liquid ammonia during nominal operation [35]. Therefore, the same mass flow rate has been used for the state-of-the-art and tubular radiators. The inlet temperature is 276 K [31]. The flow exhausts the radiator modules through a return manifold. The return manifold is modeled as a pressure outlet boundary condition with a backflow temperature of 275.5 K [35]. The conducts are modeled as stationary no-slip walls. The near-wall temperature is considered a solid-fluid interface and coupled with the Ansys^{TM} Mechanical simulations.

In the Ansys^{TM} Mechanical simulations, the radiator structure is composed of the materials presented in Chapter 5. The thermal conductivity of carbonyl iron, melt-refined iron, Fe-Si alloy, highlands metallic mixture, and distilled aluminum is input into the numerical model. The internal radiator surfaces that would be in contact with the working fluid are modeled as solid-fluid interfaces and receive the convective heat transfer coefficient and near-wall temperatures from the Ansys^{TM} Fluent simulations.

The external radiator surfaces that are not in direct contact with the lunar surface are considered to be coated with Z-93, whose emissivity is 0.92 (see Section 2.3.2). The external surfaces exchange radiative heat with the environment and the lunar surface. The environment temperature is defined as the temperature of outer space (3 K). The lunar surface is modeled as regolith with a thermal conductivity of 0.001 W/(m·K) [59]. Regolith also emits infrared radiation to the radiator structure and the environment. The average infrared emissivity of the lunar surface is considered 0.95 [60]. Although the regolith temperature fluctuates with depth due to its low thermal conductivity [60], a constant lunar surface temperature is defined at all cylindrical section boundaries. As the radiator is located in the PSR discussed in Chapter 2, a regolith surface temperature of 120 K is defined. This temperature is the highest seasonal temperature in the permanently shaded region. Therefore, it accounts for the worst-case scenario regarding the amount of rejected heat.

7.2 Results

Table 7–1 summarizes the results of the thermal simulations described above. The configurations presented in Figure 7–1 are simulated for the five structural materials discussed in Chapter 5. The total rejected heat flow rate per radiator module and the radiator mass per unit of rejected heat flow rate are reported.

Tab. 7–1: Thermal simulation results.

	Description	Structural Material	Heat Flow Rejection (W)	Mass Factor (kg/kW)
(a)	State-of-the-art radiator above the lunar surface	Carbonyl Fe	3322	192
		Melt-refined Fe	3199	200
		Fe-Si Alloy	3167	197
		Highlands Met. Mixture	3075	71
		Distilled Al	3429	61
(b)	State-of-the-art radiator on the lunar surface	Carbonyl Fe	2240	285
		Melt-refined Fe	2209	289
		Fe-Si Alloy	2198	284
		Highlands Met. Mixture	2173	100
		Distilled Al	2270	93
(c)	Tubular radiator above the lunar surface	Carbonyl Fe	3132	194
		Melt-refined Fe	3131	194
		Fe-Si Alloy	3130	190
		Highlands Met. Mixture	3129	66
		Distilled Al	3133	64
(d)	Tubular radiator on the lunar surface	Carbonyl Fe	2448	249
		Melt-refined Fe	2430	251
		Fe-Si Alloy	2406	248
		Highlands Met. Mixture	2359	88
		Distilled Al	2456	82

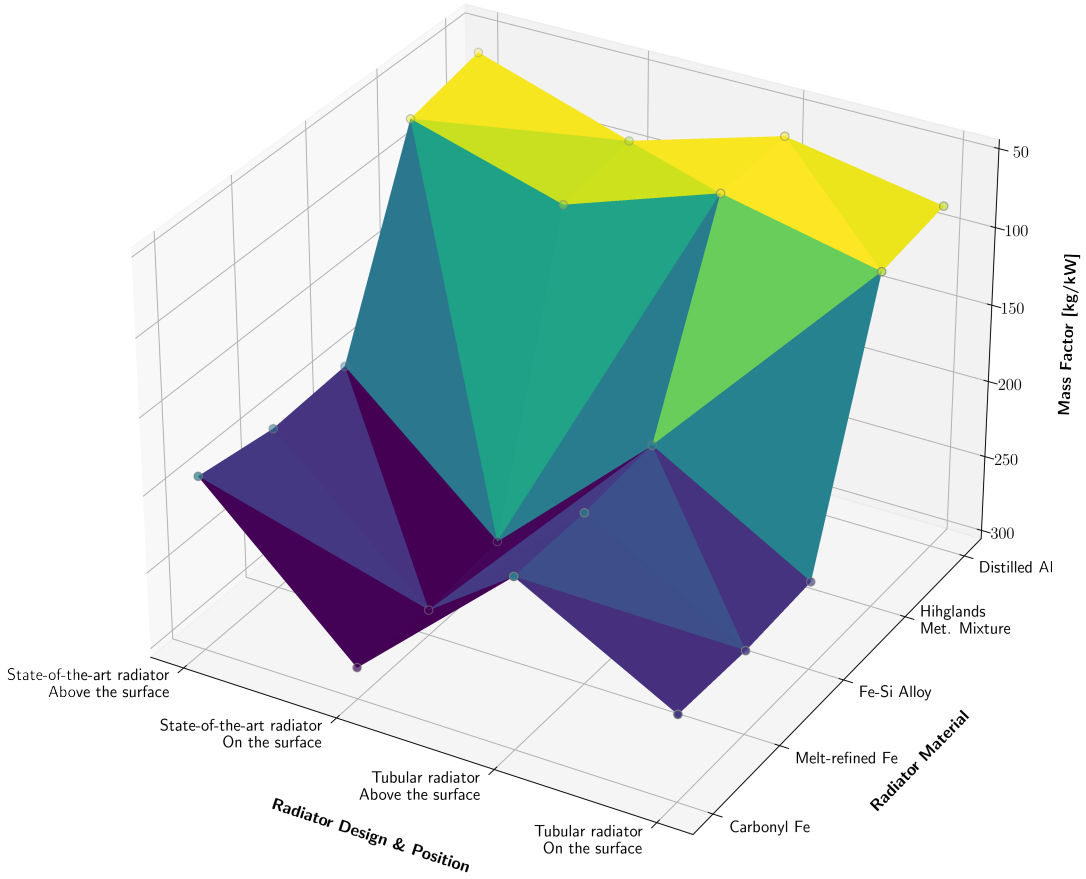

Fig. 7–2: Radiator mass factors

The tubular radiator is capable of rejecting a higher amount of heat than the state-of-the-art radiator when placed on the lunar surface. As already discussed in Section 2.3.1.2, a tubular radiator with a smaller diameter shall magnify the differences between both concepts. However, if the radiators are placed above the lunar surface, both concepts perform similarly. The radiator designs that lay on regolith, where not only radiation but also conduction occurs, reject a lower amount of heat than the concepts placed above the lunar surface.

The thermal conductivity of the different material concepts does not significantly impact the amount of rejected heat. The influence of the thermal conductivity is more notable for the state-of-the-art radiator due to the greater structural material thickness. As thermal and mechanical stresses are expected to remain low, the strength shall not be a determining material property. Therefore, other relevant mechanical properties, such as corrosion resistance with respect to the working fluid or hardness to prevent leakages due to micrometeorite impacts, shall play a more relevant role when selecting an ISRU material. Ductility would also determine the suitability of various manufacturing concepts. However, these properties cannot be estimated easily without experi-

mental testing. They do not only depend on the material composition but also on the processing and manufacturing techniques used. For instance, casting parts under reduced lunar gravity shall slightly influence the solidification mechanisms and material microstructure.

Figure 7–2 is a visual representation of the mass factors presented in Table 7–1. If the mechanical requirements can be assured, light materials, such as the highlands metallic mixture or distilled aluminum, are preferable as they require less processed mass per unit of rejected heat flow rate. It must be noted that the mass factors do not account for the necessary structure to elevate the radiator concepts above the lunar surface.

8 Concept Evaluation

A Multi-Criteria Analysis (MCA) is carried out to evaluate the in-situ material production concepts defined in Chapter 6.

In Section 8.1, the evaluation criteria of the MCA are discussed. In Section 8.2, the MCA results are presented, and an in-situ material production concept is selected as an appropriate ISRU process chain to simultaneously produce oxygen for life support or propellant production, and metals to manufacture a TCS radiator on-site.

8.1 Evaluation Criteria

The MCA combines an Equivalent System Mass (ESM) analysis with a qualitative weighted evaluation of the ISRU process chain versatility. The ESM analysis accounts for the mass, volume, power, and cooling requirements of the excavation, beneficiation, oxygen extraction, and metal processing stages. The equivalent system mass of these stages is normalized ($M_{ESM,norm}$) between 0 and 100 and weighted by a factor (γ_{ESM}) of 0.70. The qualitative evaluation of the ISRU process chain considers the versatility of the oxygen extraction, metal processing, and manufacturing stages. Its evaluation criteria and scoring system is described in Section 8.1.2. The versatility score ($\Gamma_{vers,norm}$) ranges between 0 and 100 and is weighted by a factor (γ_{vers}) of 0.30.

$$\Gamma_{concept} = \gamma_{ESM} \cdot (100 - M_{ESM,norm}) + \gamma_{vers} \cdot \Gamma_{vers,norm} \tag{8–1}$$

Equation 8–1 is used to calculate the overall score of each in-situ material production concept ($\Gamma_{concept}$). The higher the score, the less initial mass must be brought from Earth, and the more versatile the concept is.

8.1.1 Equivalent System Mass

For each in-situ material production concept, the ESM analysis calculates the mass that must be initially brought from Earth to produce 15 t/y of O_2 and manufacture, within a year, a TCS radiator capable of rejecting the heat generated by the ECLSS and ISRU facility.

The ISS-based ECLSS described in [24] is simulated in V-HAB [182] for 6 CM to estimate the maximum required heat rejection. A schematic representation of this ECLSS can be found in Figure 2–2. The maximum heat rejection is 26 kW.

The heat that must be rejected by the ISRU facility depends on the in-situ material production concept. Appendix C summarizes the ESM input data of each production concept. From the cooling requirements reported, the maximum heat rejection of the ISRU facility can be calculated.

The total radiator heat rejection is computed by adding the ECLSS and ISRU facility cooling requirements, including an oversizing factor of 1.25. Once the total heat

rejection is known, the radiator mass can be estimated using the material properties discussed in Chapter 5 and the thermal simulations performed in Chapter 7.

The materials can be grouped into low-strength brittle, high-strength brittle, low-strength ductile, and high-strength ductile materials. Carbonyl iron and the ferrosilicon alloys belong to the group of high-strength ductile materials, whereas melt-refined iron belongs to the group of high-strength brittle materials. Distilled aluminum is a low-strength ductile material, and the highlands metallic mixture a low-strength brittle material.

In Chapter 7, two radiator positions were discussed. The radiator designs that lay on the lunar surface reject a lower amount of heat than the concepts placed above it. However, for these last concepts, the mechanical stresses are higher. Therefore, it is considered that the material concepts classified as low-strength must lay on the lunar surface, whereas the high-strength material concepts can be placed above it. These assumptions return a minimum mass factor from Table 7–1 for each in-situ material production concept.

If, for the annual O_2 production of 15 t, the ISRU process chain coproduces more metallic byproduct than the amount required to manufacture the radiator, the mass, volume, power, and cooling requirements of the metal processing techniques discussed in Section 4.5 are linearly scaled down to match the manufacturing requirements.

$$M_{ESM} = \sum_{i}^{n} M_i + \gamma_V \cdot \sum_{i}^{n} V_i + \gamma_P \cdot \sum_{i}^{n} P_i + \gamma_Q \cdot \sum_{i}^{n} \dot{Q}_i \tag{8–2}$$

Equation 8–2 is used to calculate the equivalent system mass (M_{ESM}) for each in-situ material production concept. M_i, V_i, P_i, and Q_i represent the mass, volume, power, and cooling requirements of each ISRU process chain component. This values are reported in Appendix C. The ESM factors are obtained from [76]. The volume ESM factor (γ_V) is assumed 9.16 kg/m^3 for unshielded inflatable modules. The low equivalency factor shall mainly account for lightweight packaging. The power ESM factor (γ_P) is assumed 54 kg/kW for solar voltaic power generation. A duty cycle of 0.75 has been considered throughout the thesis. Therefore, the actual power ESM factor does not consider energy storage. The cooling ESM factor (γ_Q) is assumed 221 kg/kW for horizontal flow-through radiators. It must be noted that Anderson et al. [76] power and cooling factors are calculated for the lunar equator.

The on-site manufactured radiator would theoretically remove the necessity of bringing a radiator from Earth. Therefore, γ_Q might be considered null in the ESM analysis. However, in order to produce the necessary metals, heat must be rejected by the ISRU facility before the radiator is manufactured. An optimal approach would be to steadily scale up the oxygen and metal production rate, coordinating the use of Earth-brought and on-site manufactured radiator modules. However, the desired O_2 production rate of 15 t/y would not be reached during the first year of operation with this approach.

8.1.2 ISRU Process Chain Versatility

The versatility criteria aim to evaluate the advantages and disadvantages of the in-situ material production concepts that cannot be quantitatively included in an ESM analysis. Several versatility categories are defined for the oxygen extraction, metal processing, and manufacturing stages of the ISRU process chain. For each category, the processes are scored, normalized between 0 and 100, and weighted. Since the manufacturing stage is not included in the ESM analysis, its weight factor (γ_{manuf}) is 0.50. The oxygen extraction and metal processing stages have weight factors (γ_{O_2} and γ_{metal}) of 0.25. If a concept does not require a metal processing stage, its weight factor is evenly distributed between the oxygen extraction and manufacturing stages.

$$\Gamma_{vers,norm} = \gamma_{O_2} \cdot \Gamma_{O_2,norm} + \gamma_{metal} \cdot \Gamma_{metal,norm} + \gamma_{manuf} \cdot \Gamma_{manuf,norm} \tag{8–3}$$

Equation 8–3 is used to calculate the versatility score ($\Gamma_{vers,norm}$) based on the normalized scores of the ISRU process chain stages ($\Gamma_{O_2,norm}$, $\Gamma_{metal,norm}$ and $\Gamma_{manuf,norm}$). These normalized scores are discussed in the following sections.

8.1.2.1 Oxygen Extraction Versatility Criteria

The two versatility criteria considered in this analysis are: 1) the ability of an oxygen extraction process to yield byproducts other than O_2 and the principal metals discussed in Chapter 5, and 2) the amount of principal metals that would remain after the production of 15 t/y of O_2 and the on-site manufacturing of the TCS radiator. Both criteria are evenly weighted with respect to the O_2 extraction versatility score ($\Gamma_{O_2,norm}$).

For the ability to yield byproducts other than O_2 and principal metals, the three oxygen extraction processes discussed in Section 4.4 are first ranked between 1 and 3. The score is subsequently normalized between 0 and 100.

MRE and MSE share the first position. MSE can reduce all the oxides and recover most of the metals and metalloids present in lunar regolith. However, these metals and metalloids cannot be easily separated from each other without previous beneficiation of subsequent metal refining. Although MRE might recover a narrower variety of metals and metalloids, specific alloys can be directly extracted from the MRE reactor without further processing. Hydrogen can only reduce ilmenite, which additionally yields TiO_2. For this reason, it ranks last.

The amount of principal metals that would remain after the production of 15 t/y of O_2 and the on-site manufacturing of the TCS radiator is calculated after the ESM analysis. This criterion accounts for the possibility of manufacturing additional components other than a radiator. The remaining metal mass is normalized between 0 and 100.

8.1.2.2 Metal Processing Versatility Criteria

A single versatility criterion is considered for the metal processing stage. This criterion is: 1) the ability of the metal processing technique to refine a wide variety of ISRU materials.

The three metal processing techniques discussed in Section 4.4 are first ranked between 1 and 3. The score ($\Gamma_{metal,norm}$) is subsequently normalized between 0 and 100.

Vacuum distillation ranks first as it can directly separate calcium, aluminum, and silicon. If the operating point of the distillation chamber is controlled, almost any ISRU material can be refined. Melting and refining ranks second. Not only iron could be separated from slag but also several other ISRU metals could be refined through metal-oxide phase separation. As the carbonylation reaction can only process iron and nickel, it ranks last.

8.1.2.3 Manufacturing Versatility Criteria

Two versatility criteria are considered for the manufacturing stage. These versatility criteria are: 1) the energy consumption of the manufacturing techniques, and 2) the flexibility to produce a wide variety of end products. Four combinations of manufacturing techniques exist for the in-situ material production concepts: 1) additive manufacturing, 2) additive manufacturing and chemical vapor deposition or chemical decomposition, 3) additive manufacturing and extrusion, and 4) casting and extrusion. Therefore, the manufacturing techniques are ranked between 1 and 4, and subsequently normalized between 0 and 100. Both criteria are evenly weighted with respect to the manufacturing versatility score ($\Gamma_{manuf,norm}$).

Additive manufacturing is the technique that consumes the least energy [183, 165]. The energy consumption increases when supplementary processes are required to prepare the feedstock. Consequently, additive manufacturing is followed by AM and CVD, and AM and extrusion. Casting is the manufacturing technique that requires the highest energy input as it needs to melt the materials before pouring them into a mold. Therefore, it ranks last.

Complex geometries and repetitive parts could be manufactured when extrusion and additive manufacturing are combined. Therefore, this combination of processes ranks first, followed by AM and CVD. In this case, not only complex geometries but also thin shapes and coatings could be produced. Casting ranks last due to the existing limitations with respect to the mold geometries and the manufacturing of fine structures and.

8.2 Evaluation Results

Once the criteria have been defined, the MCA can be performed to evaluate the in-situ material production concepts presented in Chapter 6. An ESM sensitivity analysis is preliminarily carried out in Section 8.2.1 to investigate the influence of the MSE electrolyte loss rate and estimate from what mission duration is beneficial to consider ISRU techniques instead of bringing all material resources from Earth. After the sensitivity analysis, the final ESM results are presented in Section 8.2.2. The ISRU process chain versatility results are discussed in Section 8.2.3. After the evaluation of both MCA components, the final results return an optimal ISRU process chain architecture that produces 15 t/y of O_2 and manufactures, within a year, a TCS radiator capable

of rejecting the heat generated by the ECLSS and ISRU facility. These results can be found in Section 8.2.4.

To facilitate the understanding of the analysis, the principal assumptions made in this work are summarized in the following paragraphs. However, the reader is directed to the specific sections, in which the assumptions were made, for a more comprehensive explanation and justification. Detailed descriptions of the ISRU system models can be found in Chapter 4. The mass, volume, power, and cooling requirements of each in-situ material production concept are reported in Appendix C.

According to Chapter 2, the surface reference mission is located on a high plane close to the crater Kocher in the lunar South Pole. This location has near access to middle-size PSRs where the TCS radiator can be placed. The maximum seasonal temperature at the PSRs is 120 K. The Moonbase is composed of a six-CM ECLSS and an ISRU facility. The ISRU facility produces 15 t/y of O_2 and enough metallic byproducts to manufacture a radiator that rejects the heat generated by the Moonbase with an oversizing factor of 1.25. The maximum heat rejection of the ECLSS is 26 kW.

In Chapter 7, combinations of two radiator geometries, two radiator positions, and five ISRU materials are simulated to quantify the mass required per unit of rejected heat. In these simulations, radiative heat transfer between the radiator, the lunar surface, and the environment is considered. Convective heat transfer between the working fluid (NH_3) and the radiator structure is also modeled. When applicable, conductive heat transfer between the radiator and the lunar surface is simulated. Even if the radiator is located in a PSR, which never receives direct solar radiation, it would receive radiation reflected by the lunar surface features. However, the reflected radiation has been neglected in the thermal simulations.

A solar power plant is located in the vicinity of a POL region, where solar energy is accessible for more than 75% of the year. Therefore, the estimated duty cycle of the ISRU facility is 0.75. The duty cycle is the amount of time per year that the facility is in operation.

According to Chapter 3, highlands regolith is likely to be available in the vicinity of the Moonbase. An initial concentration of 1 wt.% of $FeTiO_3$, 6 wt.% FeO-rich minerals, and 50 wt.% of $CaAl_2Si_2O_8$ can be expected.

From Chapter 4, a single RASSOR can excavate over 1000 t/y of regolith. The beneficiation stage raises the ilmenite concentration to 80 wt.% for concepts S1, T1, and T4; and the FeO concentration to 20 wt.% for concepts S2 and T2. It also raises the anorthite concentration to 90 wt.% for concepts S3 and T3. The handling stage has been neglected in this analysis.

Concepts S1, T1, and T4 include a H_2 reduction assembly to extract O_2 from lunar regolith (see Section 4.4.1 for a description of the H_2 reduction model). Concepts S2 and T2 include an MRE assembly to extract O_2 from lunar regolith (see Section 4.4.2 for a description of the MRE model). Concepts S3, T3, and S4 include an MSE assembly to extract O_2 from lunar regolith (see Section 4.4.3 for a description of the MSE model).

Concepts S1 and T1 include a carbonylation assembly to extract Fe from reduced ilmenite (see Section 4.5.1 for a description of the carbonylation model). Concepts S3 and T3 include a vacuum distillation assembly to extract Al from Ca-Al-Si alloys (see Section 4.5.3 for a description of the vacuum distillation model). Concept T4 includes a melting and refining assembly to extract Fe from reduced ilmenite (see Section 4.5.2 for a description of the melting and refining model).

8.2.1 ESM Sensitivity Analysis

A preliminary analysis of the equivalent system mass is carried out before the final evaluation of the concepts. As mentioned in Section 4.4.3, the sensitivity of the MSE electrolyte loss rate is studied. Three different loss rates are evaluated. A conservative assumption defines an electrolyte loss rate of 0.84 kg of $CaCl_2$ per kg of O_2 produced. This loss rate is equivalent to removing 0.7 wt.% of the electrolyte per batch when the cathode is extracted after the electrolysis. This assumption would require a total replenishment of the initial $CaCl_2$ mass within a year, which agrees with Lomax et al. [130], who report that for terrestrial applications, the Metalysis production units run throughout a year before replacing the molten salt. A more optimistic assumption would define an electrolyte loss rate of 0.42 kg of $CaCl_2$ per kg of O_2 produced. This loss rate agrees with the estimations provided by Monchieri et al. [19], who assumed the use of pressed and sintered regolith tiles with a porosity of 20%, and an electrolyte loss rate of 0.5 kg of $CaCl_2$ per kg of O_2. However, the values provided “are a really rough estimations and direct information (...) are needed to estimate this very delicate figure of the process” [19]. It would be equivalent to removing 0.35 wt.% of the electrolyte per batch when the cathode is extracted after the electrolysis, requiring replenishment of half of the initial $CaCl_2$ mass per year. If MSE is specifically optimized for ISRU applications, a loss rate lower than 0.21 kg of $CaCl_2$ per kg of O_2 might be reachable. This loss rate is equivalent to removing 0.17 wt.% of the electrolyte per batch when the cathode is extracted after the electrolysis, requiring replenishment of a quarter of the initial $CaCl_2$ mass per year.

Figure 8–1 displays the ESM break-even points for the excavation, beneficiation, and oxygen extraction stages of the in-situ material production concepts. Only the production of 15 t/y of O_2 is considered. The processing of metallic byproducts is preliminarily neglected. The open-loop case brings 15 t/y of oxygen from Earth. The ilmenite reduction with H_2 case includes concepts S1, T1, and T4. The molten regolith electrolysis case includes concepts S2 and T2. The molten salt electrolysis cases include concepts S3, T3, and S4.

The earliest break-even point reached is MRE after a mission duration of 110 days, followed by the ilmenite reduction with hydrogen (500 days) and MSE with an electrolyte loss rate of 0.21 kg of $CaCl_2$ per kg of O_2 (685 days). The MSE electrolyte loss rates of 0.42 and 0.84 kg of $CaCl_2$ per kg of O_2 require 2.6 and more than 9 years, respectively, to reach their break-even points.

Appendix C summarizes the ESM input data of each in-situ material production concept. It must be noted that, since the handling stage has been neglected in this analy-

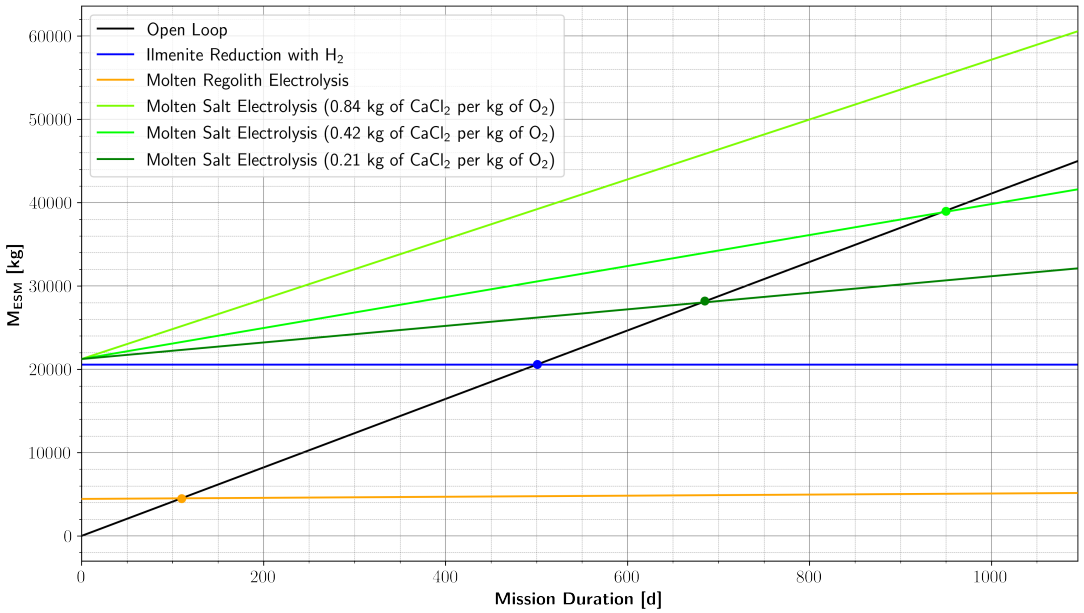

Fig. 8–1: ESM break-even points for ISRU O_2 production with respect to mission duration.

sis, the break-even points of an actual ISRU facility would be delayed compared to the points displayed in Figure 8–1.

A similar study to Figure 8–1 is carried out in Figure 8–2, including the metal processing stage. In this case, the analysis considers the production of 15 t/y of O_2 and enough metals to manufacture, within a year, a radiator capable of rejecting the heat generated by the ECLSS and ISRU facility. The open-loop cases bring from Earth not only 15 t/y of oxygen but also the same amount of metals that would be produced on-site. When the metal processing stage is included, the break-even points are reached earlier. For the concepts S2 and T2, the break-even points are reached after 75 mission days instead of 110 days. For the concepts S1, T1, and T4, the break-even points are reached after 325 days instead of 500 days. In concepts S3 and T3, the MSE electrolyte loss rates of 0.21, 0.42, and 0.84 kg of $CaCl_2$ per kg of O_2 require 1.9, 2.2, and 4.8 years, respectively, to reach their break-even points. In concept S4, the MSE electrolyte loss rates of 0.21, 0.42, and 0.84 kg of $CaCl_2$ per kg of O_2 require 1.4, 1.9, and 4 years, respectively, to reach their break-even points.

It can be observed in Figures 8–1 and 8–2 that, independently from the electrolyte loss rate, the concepts that include an MSE assembly reach their break-even points at the latest. For the final evaluation of the in-situ material production concepts, an electrolyte loss rate of 0.42 kg of $CaCl_2$ per kg of O_2 is considered. The ESM analysis evaluates the mass that would have to be brought from Earth for a three-year mission. All concepts would have reached their break-even points before the end of the mission for this duration.

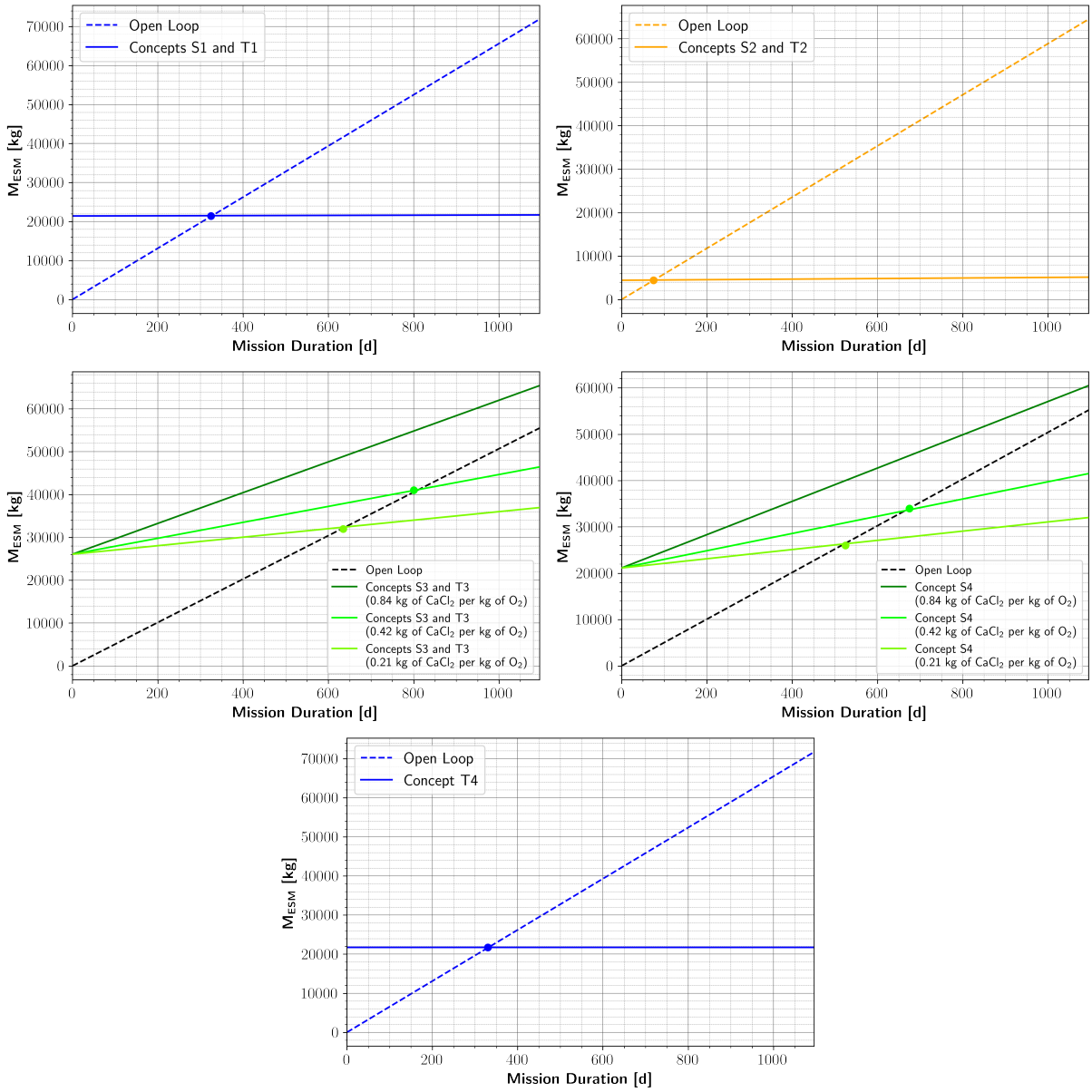

Fig. 8–2: ESM break-even points for ISRU O_2 and metal production with respect to mission duration.

8.2.2 ESM Results

Table 8–1 summarizes the final ESM results for each in-situ material production concept. Concepts S2 and T2, which include a molten regolith electrolysis assembly, return the lowest M_{ESM}.

Figure 8–3 displays the distribution of the equivalent system mass per ISRU process chain stage. It can be observed that concepts S1, T1, and T4, which include a hydrogen reduction assembly, are significantly penalized by the excavation and beneficiation stages. Highlands regolith contains a low concentration of $FeTiO_3$ and other FeO-rich minerals, which dramatically increases the amount of regolith that must be processed.

Tab. 8–1: ESM results.

Concept	Mass (kg)	Volume (m^3)	Power (kW)	Cooling (kW)	M_{ESM} (kg)
S1	13937	93.48	80.30	10.88	21536
T1	13957	93.53	80.40	10.91	21566
S2	1570	2.86	60.85	1.36	5183
T2	1571	2.86	60.85	1.36	5184
S3	38412	28.71	121.46	5.68	46489
T3	38198	28.26	115.58	5.10	45825
S4	36812	25.44	77.04	1.38	41511
T4	13531	92.51	94.25	10.07	21693

However, hydrogen reduction might be a competitive alternative to MRE when mare regolith is available. Ilmenite can be found in high-Ti mare soils in concentrations $>$16 wt.%. These concentrations would reduce the amount of regolith that must be processed, decreasing the M_{ESM} of the excavation and beneficiation stages.

The concepts S3, T3, and S4, which include an MSE assembly, are dramatically penalized by the electrolyte mass and its loss rate. If MSE is to be considered a competitive oxygen extraction candidate, the initial $CaCl_2$ mass and losses must be significantly reduced compared to current terrestrial standards. The electrolyte ratio of 53.34 kg of $CaCl_2$ per kg of regolith must be at least quartered, and the estimated loss rate of 0.42 kg of $CaCl_2$ per kg of O_2 must be reduced no less than an order of magnitude.

It can also be observed that distilling aluminum (concepts S3 and T3) is notably more costly than producing iron (concepts S1, T1, and T4) or ferrosilicon alloys (concepts S2 and T2). For the vacuum distillation process, the limiting factor is the removal rate of the vapor phase, which depends on the operating pressure and pumping speed. Although ultra-high vacuum conditions could be achieved due to the tenuous lunar atmosphere, high operating pressures are required to maintain the processing time within a reasonable range. Higher operating pressures imply higher boiling points and more power input.

Figure 8–4 represents the contribution of the total mass, volume, power, and cooling requirements to the equivalent system mass. The ESM factors considered are $\gamma_V = 9.16$ kg/m^3, $\gamma_P = 54$ kg/kW, $\gamma_Q = 221$ kg/kW.

The mass contribution of the concepts that include an MRE assembly is significantly lower than for the H_2 reduction and MSE cases. H_2 reduction reactors have to process higher amounts of regolith to obtain the same amount of O_2 due to the lower oxygen yield of the extraction process. Therefore, larger and heavier reactors are required. In the MSE case, the necessity of a molten salt bath is a significant disadvantage in terms of mass requirements.

The power contribution of the MRE assembly is higher than its mass contribution due

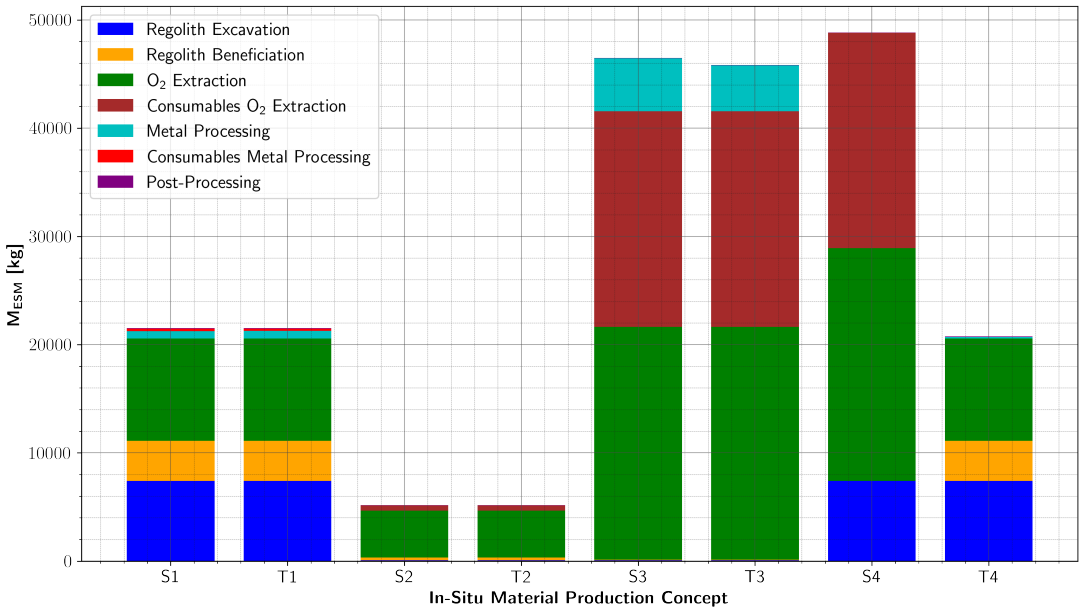

Fig. 8–3: Equivalent system mass contribution per ISRU process chain stage.

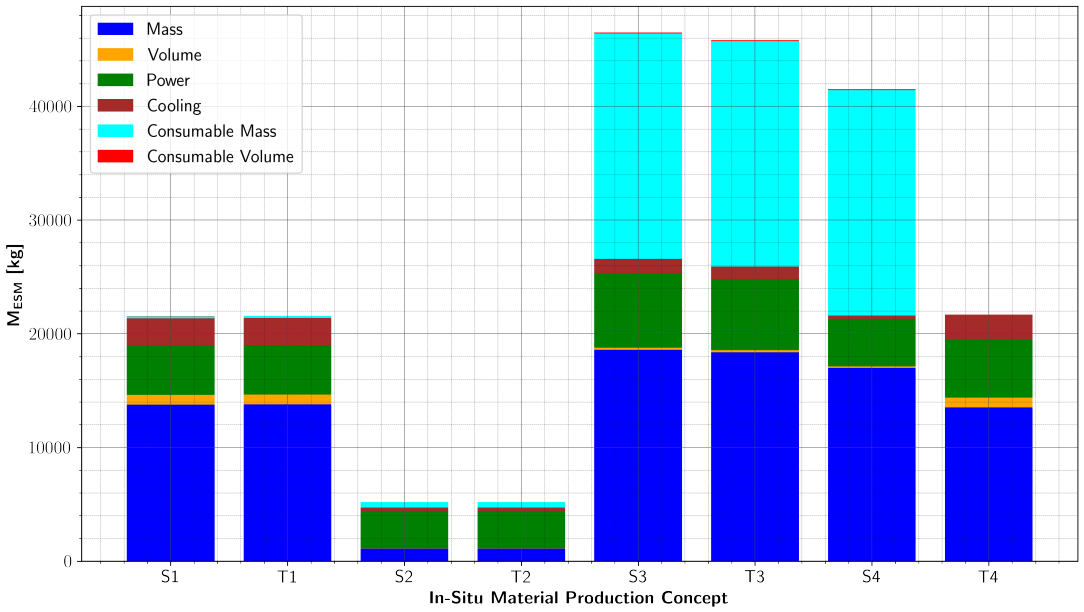

Fig. 8–4: Equivalent system mass contribution per ESM component. The ESM factors considered are $\gamma_V = 9.16$ kg/m^3, $\gamma_P = 54$ kg/kW, $\gamma_Q = 221$ kg/kW.

to the elevated temperatures ($>$ 2200 K) at which the reactor has to operate. However, although the operating temperature of MRE is significantly higher than for H_2 reduction (1000 K) and MSE (1200 K), the power contribution across concepts is reasonably similar. Concepts that contain a H_2 reduction assembly require more power in the excavation stage. Concepts that include an MSE assembly require more power to distill Al in the metal processing stage. Moreover, the low current efficiency of the FFC-Cambridge process also plays a significant role in the power contribution of the MSE

assemblies.

The cooling contribution of the H_2 reduction assembly is higher than for MRE and MSE since produced water vapor has to condensate before entering the electrolyzer.

8.2.3 ISRU Process Chain Versatility Results

Table 8–2 summarizes the ISRU process chain versatility results for each in-situ material production concept. Concept S4 returns the highest score. Its MSE assembly can reduce all the oxides and recover most of the metals and metalloids present in lunar regolith. Moreover, its manufacturing stage includes powder-based additive manufacturing, which has the lowest energy consumption and is capable of manufacturing a wide variety of geometries.

Concept S4 is followed by concepts S3 and T1. In concept S3, a lower amount of refined metals remain. Furthermore, the energy consumption required to prepare the AM wire feedstock through extrusion slightly penalizes the manufacturing stage. Concept T1 scores better in the versatility of the manufacturing stage. However, it is significantly penalized by the H_2 reduction and Carbonyl process, which can only extract iron and nickel.

Tab. 8–2: ISRU process chain versatility results.

Concept	Oxygen Extraction			Metal Processing		Manufacturing			
	Byproduct Variety	Remaining Metals (t)	$\Gamma_{O_2,norm}$	Byproduct Variety	$\Gamma_{metal,norm}$	Energy Consumption	Manufacturing Flexibility	$\Gamma_{manuf,norm}$	$\Gamma_{vers,norm}$
S1	1	38.1	50	1	0	3	2	60	42.50
T1	1	38.0	50	1	0	3	4	100	62.50
S2	3	0.0	50	-	-	2	3	60	56.25
T2	3	0.0	50	-	-	1	1	0	18.75
S3	3	1.7	52	3	100	2	3	60	68.00
T3	3	2.2	53	3	100	1	1	0	38.25
S4	3	15.6	70	-	-	4	2	80	76.25
T4	1	38.1	50	2	50	1	1	0	25.00

8.2.4 Optimal ISRU Process Chain Architecture

Table 8–3 combines the ESM results with the ISRU process chain versatility scores, returning an optimal ISRU process chain architecture that produces 15 t/y of O_2 and manufactures a TCS radiator on-site.

Three main groups can be distinguished in Table 8–3 based on their oxygen extraction process and their equivalent system mass. Concepts S1, T1, and T4 produce O_2 through H_2 reduction and require an M_{ESM} of $\sim$21 t. Concepts S2 and T2 produce O_2 through molten regolith electrolysis and require an M_{ESM} of $\sim$5 t. Concepts S3, T3, and S4 produce O_2 through molten salt electrolysis and require an M_{ESM} of over 40 t.

The ISRU process chain versatility score helps to identify which concept stands out within its group. From the MRE group, which requires the lowest M_{ESM}, concept S2 stands out as the optimal architecture to reach the mission goals defined in this work.

A detailed breakdown of the mass, volume, power, and cooling requirements of this concept can be found in Table C–3. A RASSOR excavates 800 t/y of highlands regolith. The regolith is enriched in a beneficiation stage to obtain 41.7 t/y of FeO-rich minerals (20 wt.% FeO). To build the beneficiation stage on the lunar surface, 236 kg must be brought from Earth. The FeO-rich regolith is introduced in an MRE assembly that weighs 533 kg and occupies 1.6 m^3, consuming 61 kW of electric power and rejecting 1.4 kW of heat. 237 kg must be brought from Earth every year to account for the electrode replacement rate. The MRE assembly is capable of producing 15 t/y of O_2 and 6.7 t/y of Fe-Si alloys. The ferrosilicon alloys are extruded to produce wire feedstock. AM techniques use this wire feedstock to manufacture a state-of-the-art radiator that rejects 34.2 kW of heat. To accomplish it, the radiator, which is placed above the lunar surface, occupies 86.5 m^2, has a radiating surface of 173 m^2, and requires 33 kg of Z-93 coating. This radiator would have a mass factor of 197 kg/kW of rejected heat. Therefore, it would require an entire year to produce the 6.7 t of Fe-Si alloys for its manufacturing.

Tab. 8–3: Evaluation results.

Concept	M_{ESM} (kg)	$M_{ESM,norm}$	Weighted $M_{ESM,norm}$	$\Gamma_{vers,norm}$	Weighted $\Gamma_{vers,norm}$	$\Gamma_{concept}$
S1	21536	39.59	42.29	42.50	12.75	55.04
T1	21566	39.66	42.24	62.50	18.75	60.99
S2	**5183**	**0.00**	**70.00**	**56.25**	**16.88**	**86.88**
T2	5184	0.00	70.00	18.75	5.63	75.63
S3	46489	100.00	0.00	68.00	20.40	20.40
T3	45825	98.39	1.13	38.25	11.46	12.59
S4	41511	87.95	8.44	76.25	22.88	31.24
T4	21693	39.97	42.02	25.00	7.50	49.52

9 Conclusions

In this Master's thesis, an MCA, comprised of an ESM analysis and a qualitative evaluation of the ISRU process chain versatility, has been carried out to identify the most suitable in-situ material production concept that produces 15 t/y of O_2 and enough metallic byproducts to manufacture a radiator that rejects the heat generated by the ECLSS and ISRU facility.

Analytical sizing models were developed for the entire ISRU process chain, including the individual production stages: excavation, beneficiation, oxygen extraction, and metal processing. Focus was given to the oxygen extraction and metal processing stages. The oxygen extraction stage analyzed $FeTiO_3$ reduction with H_2, MRE, and MSE. The metal processing stage investigated carbonylation, melt-refining, and vacuum distillation. The models returned their mass, volume, power, and cooling requirements based on previously published works, analytical calculations, data extrapolated from experimental research, and analogies drawn between terrestrial and space components.

The most suitable concept consisted of an MRE reactor that produces 15 tons of oxygen and 6.7 tons of ferrosilicon alloys per year. 800 t/y of highlands regolith are excavated and beneficiated to reach a concentration of 20 wt.% of FeO-rich minerals. Fe-Si alloys are extruded to produce wire feedstock. Wire-based additive manufacturing techniques manufacture a radiator that rejects 34.2 kW of heat. The entire ISRU process chain requires 1100 kg and 2.8 m^3, consuming 61 kW of electric power and rejecting 1.4 kW of heat. The MRE electrodes (237 kg/y) must be regularly brought from Earth. For lunar surface missions longer than six months, the concept proposed in this thesis would already be more economical than transporting all material resources from Earth.

The concepts that included a H_2 reduction reactor, were significantly penalized by the excavation and beneficiation stages. The assumed $FeTiO_3$ concentration was 1 wt.% for highlands regolith, which dramatically raised the amount of regolith that must have been processed. However, H_2 reduction has been proven as a competitive alternative to MRE when high-Ti mare regolith ($\sim$ 20 wt.% of $FeTiO_3$) is available. From reduced ilmenite, two material concepts could be extracted: carbonyl and melt-refined iron.

The concepts that included an MSE cell were dramatically penalized by the required electrolyte mass. The electrolyte losses and the anode degradation also required that large amounts of consumables were regularly brought from Earth. MSE must be further developed for space environments before it can be considered a competitive ISRU oxygen extraction candidate. Besides oxygen, MSE can produce mixtures of metallic alloys. These mixtures might be processed in a vacuum distillation chamber to separate individual metals, such as aluminum.

9.1 Outlook

ISRU System Modeling

There are a number of items that can be addressed in future work with respect to the ISRU models presented in Chapter4. The RASSOR excavator model could be improved with the design proposed by Schluer et al. [73]. The payload capacity, power consumption, and volume could be updated.

The development of a more accurate beneficiation model is crucial for the correct assessment of the concepts that include a H_2 reduction reactor. This development must come alongside an increase in the TRL of dry beneficiation processes. The magnetic separator model could be improved including the relationship between the magnetic field strength, initial regolith composition, enrichment grade, and recovery efficiency. An electrostatic separator model could also be developed to allow comparisons between subsystems. A preliminary analysis showed that if regolith had to be preheated before the electrostatic separation the required thermal power input would be unreasonably high. The model could include the relation between the thermal power input, initial regolith composition, electrical conductivity of the regolith minerals, enrichment grade, and recovery efficiency to evaluate in which scenarios electrostatic beneficiation is more beneficial than magnetic separation.

The handling stage must also be included in the future. Schreiner [17] reported models for a hopper and feed system. The oxygen liquefaction unit and storage tank were also considered. Additional handling systems that shall be modeled in the future include several gas and liquid storage tanks or the transportation and management of molten metals.

LiSTOT's library [113] might be expanded to include not only ECLSS but also ISRU components. A strict bottom-up approach could provide values for piping systems, filters, and individual components of a water or oxygen purification unit. A parametric model of a heat exchanger or cold traps could be developed since it is a common element in ISRU architectures.

Additional oxygen extraction models could be integrated, such as those for carbothermal reduction or vapor pyrolysis. The H_2 reduction model could include a more precise fluidized bed reactor, which considers effect of the operating pressure, or the height-to-diameter ratio [184]. Schreiner [17] discusses the future work related to the improvement of the MRE reactor. The MSE model must be further developed to link the oxygen yield with the electrolysis time and the current efficiency. This development could be based on the work already developed by Schreiner [17] for MRE. The influence of the electrolyte ratio on the electrolysis performance must be included. The consumable replacement rate must be experimentally quantified.

For the metal processing techniques, a high amount of experimental testing is required before the further development of more complex analytical models. The kinetics of the reduced ilmenite carbonylation and the behavior of the metal-slag phase separation must be profoundly understood through large-scale laboratory experiments. MIVMs

could be developed to predict the behavior of multi-component alloys during vacuum distillation. Additional metal processing techniques might be modeled to further refine ISRU byproducts.

Integrated ISRU Optimization Framework

An integrated ISRU framework could be developed in the future to enable the analysis and optimization of ISRU architectures. Chepko et al. [185, 186, 187] developed an architecture framework for the discrete optimization of ISRU Systems. Their work demonstrated some of the first optimizations of lunar ISRU systems, using genetic algorithms to locate the continuous design variables and discrete ISRU processes that returned the lowest system mass. This approach was also followed by Schreiner [17] to develop the integrated MRE model used in this work. The models developed in this thesis, in particular the ones corresponding to the metal processing stage, could be incorporated in such a framework to analyze the overall system performance. To the best of the author's knowledge, ISRU metal production has never been investigated by this means.

A more ambitious approach could dynamically simulate the statically optimized ISRU architectures to identify possible bottlenecks, scaling the systems accordingly. These dynamic calculations could be coupled with matter- and energy-flow simulators such as V-HAB [182] to incorporate the interactions between the ECLSS and ISRU processes, allowing the modeling of common water infrastructure or in-situ propellant production. This approach has already been proposed by Kaschubek et al. [24] for ilmenite reduction with hydrogen.

Bibliography

[1] National Aeronautics and Space Administration, “Artemis plan: Nasa’s lunar exploration program overview,” 2020. [Online]. Available: https://www.nasa.gov/sites/default/files/atoms/files/artemis_plan-20200921.pdf [Last accessed: 09-06-2021]

[2] G. Petrov, D. Inocente, C. Koop, J. Hoffman, V. Sumini, A. Makaya, M. Arnhof, H. Lakk, B. Lamaze, A. Cowley, D. Binns, M. Landgraf, P. Messina, and C. Haignere, “Moon village reference masterplan and habitat design,” in *49th International Conference on Environmental Systems (ICES)*, 2019.

[3] D. Inocente, C. Koop, G. Petrov, J. Hoffman, V. Sumini, A. Makaya, M. Arnhof, H. Lakk, B. Lamaze, A. Cowley, D. Binns, M. Landgraf, P. Messina, and C. Haignere, “Master planning and space architecture for a moon village,” in *70th International Astronautical Congress (IAC)*, 2019.

[4] A. Ellery, “Sustainable in-situ resource utilization on the moon,” *Planetary and Space Science*, vol. 184, p. 104870, 2020.

[5] K. Sacksteder and G. Sanders, “In-situ resource utilization for lunar and mars exploration,” in *45th AIAA Aerospace Sciences Meeting and Exhibit*. Reston, Virigina: American Institute of Aeronautics and Astronautics, 2007.

[6] L. A. Taylor and Carrier, W. D., III, “Oxygen production on the moon: An overview and evaluation,” in *Resources of near-earth space*, J. S. Lewis, M. S. Matthews, and M. L. Guerrieri, Eds., 1993, p. 69.

[7] C. A. Jones, J. Klovstad, E. Judd, and D. Komar, “Cost breakeven analysis of cis-lunar isru for propellant,” in *AIAA Scitech 2019 Forum*. Reston, Virginia: American Institute of Aeronautics and Astronautics, 2019.

[8] I. A. Crawford, “Lunar resources: A review,” *Progress in Physical Geography: Earth and Environment*, vol. 39, no. 2, pp. 137–167, 2015.

[9] M. C. Simon, “A parametric analysis of lunar oxygen production,” in *Lunar Bases and Space Activities of the 21st Century*, W. W. Mendell, Ed., 1985.

[10] G. R. Woodcock, “Robotic lunar surface operations: Engineering analysis for the design, emplacement, checkout and performance of robotic lunar surface systems,” *D 615–11 901*, vol. 1, no. 1, 1990.

[11] E. Christiansen, C. Simonds, and K. Fairchild, “Conceptual design of a lunar oxygen pilot plant,” *EEI Report*, vol. 88–182, no. 1, pp. 58, 67, 175–179, 187–188, 192–193, 196–197, 200, 1988.

[12] H. W. Jones, “Should oxygen, hydrogen, and water on the moon be provided by earth supply, life support recycling, or regolith mining?” in *50th International Conference on Environmental Systems (ICES)*, 2021.

[13] M. B. Duke, “Architecture studies for commercial production of propellants from the lunar poles,” in *AIP Conference Proceedings*. AIP, 2003, pp. 1219–1226.

[14] C. J. Steffen, J. E. Freeh, D. L. Linne, E. W. Faykus, C. A. Gallo, and R. D. Green, "System modeling of lunar oxygen production: Mass and power requirements," in *Space Nuclear Conference*, 2007.

[15] C. J. Steffen, J. E. Freeh, D. L. Linne, E. W. Faykus, C. A. Gallo, and R. D. Green, "System modeling of lunar oxygen production using fission surface power: Mass and power requirements," *Nuclear Technology*, vol. 166, no. 3, pp. 240–251, 2009.

[16] D. Linne, S. Gokoglu, U. Hegde, R. Balasubramaniam, and E. Santiago-Maldonado, "Component and system sensitivity considerations for design of a lunar isru oxygen production plant," in *47th AIAA Aerospace Sciences Meeting including The New Horizons Forum and Aerospace Exposition*. Reston, Virigina: American Institute of Aeronautics and Astronautics, 2009.

[17] S. S. Schreiner, "Molten regolith electrolysis reactor modeling and optimization of in-situ resource utilization systems," M.Sc. Thesis, Massachusetts Institute of Technology, 2015. [Online]. Available: https://dspace.mit.edu/handle/1721.1/98589 [Last accessed: 2021-06-28]

[18] S. S. Schreiner, L. Sibille, J. A. Dominguez, and J. A. Hoffman, "A parametric sizing model for molten regolith electrolysis reactors to produce oxygen on the moon," *Advances in Space Research*, vol. 57, no. 7, pp. 1585–1603, 2016.

[19] E. Monchieri, F. Venditti, M. Vitta, C. Cinquepalmi, and I. Vukman, "Isru architecture and technology study," *ISRU-TN-CGS-002*, vol. 1, no. 1, pp. 36–37, 2010.

[20] S. Fereres, M. Morales, T. Denk, K. Osen, R. J. McGlen, A. Seidel, H. Madakashira, D. Urbina, and D. Binns, "Payload concept evaluation for water/oxygen production on the moon based on thermo- or electro-chemical reduction of lunar regolith," in *50th International Conference on Environmental Systems (ICES)*, 2021.

[21] A. F. Hepp, D. L. Linne, G. A. Landis, M. F. Wadel, and J. E. Colvin, "Production and use of metals and oxygen for lunar propulsion," *Journal of Propulsion and Power*, vol. 10, no. 6, pp. 834–840, 1994.

[22] International Space Exploration Coordination Group, "The global exploration roadmap," 2018. [Online]. Available: https://www.globalspaceexploration.org/wordpress/wp-content/isecg/GER_2018_small_mobile.pdf [Last accessed: 09-06-2021]

[23] International Space Exploration Coordination Group, "In-situ resource utilization gap assessment report," pp. 15, 27, 32, 99, 2021. [Online]. Available: https://www.globalspaceexploration.org/wordpress/wp-content/uploads/2021/04/ISECG-ISRU-Technology-Gap-Assessment-Report-Apr-2021.pdf [Last accessed: 21-04-2021]

[24] D. Kaschubek, M. Killian, and L. Grill, "System analysis of a moon base at the south pole: Considering landing sites, eclss and isru," *Acta Astronautica*, 2021.

[25] A. Zuniga, H. Modi, A. Kaluthantrige, and H. Vertadier, “Building an economical and sustainable lunar infrastructure to enable human lunar missions,” in *70th International Astronautical Congress (IAC)*, 2019.

[26] J. Flahaut, J. Carpenter, J.-P. Williams, M. Anand, I. A. Crawford, W. van Westrenen, E. Füri, L. Xiao, and S. Zhao, “Regions of interest (roi) for future exploration missions to the lunar south pole,” *Planetary and Space Science*, vol. 180, p. 104750, 2020.

[27] S. Li, P. G. Lucey, R. E. Milliken, P. O. Hayne, E. Fisher, J.-P. Williams, D. M. Hurley, and R. C. Elphic, “Direct evidence of surface exposed water ice in the lunar polar regions,” *Proceedings of the National Academy of Sciences of the United States of America*, vol. 115, no. 36, pp. 8907–8912, 2018.

[28] G. Sanders, “In-situ resource utilization (isru) capabilities,” 2016. [Online]. Available: https://www.nasa.gov/sites/default/files/atoms/files/scp07-sanders_isru.pdf [Last accessed: 2021-05-06]

[29] T. T. Lam, G. C. Birur, and P. Bhandari, “Pumped fluid loops,” in *Spacecraft Thermal Control Handbook. Volume I: Fundamental Technologies*, D. G. Gilmore, Ed. El Segundo Calif.: Aerospace Press, 2002–2003.

[30] D. G. Gilmore, “Radiators,” in *Spacecraft Thermal Control Handbook. Volume I: Fundamental Technologies*, D. G. Gilmore, Ed. El Segundo Calif.: Aerospace Press, 2002–2003.

[31] Boeing, “Active thermal control system (atcs) overview,” 2021-08-08. [Online]. Available: https://www.nasa.gov/pdf/473486main_iss_atcs_overview.pdf [Last accessed: 2021-08-08]

[32] J. A. Oren and H. R. Howell, “Space station heat rejection subsystem radiator assembly design and development,” in *SAE Technical Paper Series*, ser. SAE Technical Paper Series. SAE International400 Commonwealth Drive, Warrendale, PA, United States, 1995.

[33] R. L. Broeren and R. J. Duschatko, “International space station design-to-freeze radiators,” in *SAE Technical Paper Series*, ser. SAE Technical Paper Series. SAE International400 Commonwealth Drive, Warrendale, PA, United States, 1997.

[34] C. Pollerberg, A. Sengespeick, M. Gralher, and J. Persson, “Enhanced coolant for low temperature,” in *50th International Conference on Environmental Systems (ICES)*, 2021.

[35] M. K. Ewert, P. A. Petete, and J. Dzenitis, “Active thermal control systems for lunar and martian exploration,” in *SAE Technical Paper Series*, ser. SAE Technical Paper Series. SAE International400 Commonwealth Drive, Warrendale, PA, United States, 1990.

[36] L. Simonsen, M. J. DeBarro, and J. Farmer, “Conceptual design of a lunar base thermal control system,” *N93-14003*, vol. 1, no. 1, 1992.

[37] University of California, Los Angeles, “Diviner data,” 2021-08-05. [Online]. Available: https://luna1.diviner.ucla.edu/ [Last accessed: 2021-08-05]

[38] J.-P. Williams, B. T. Greenhagen, D. A. Paige, N. Schorghofer, E. Sefton-Nash, P. O. Hayne, P. G. Lucey, M. A. Siegler, and K. M. Aye, “Seasonal polar temperatures on the moon,” *Journal of Geophysical Research: Planets*, vol. 124, no. 10, pp. 2505–2521, 2019.

[39] G. C. Tuan, D. T. Westheimer, G. C. Birur, D. E. Beach, D. A. Jaworske, W. C. Peters, and J. J. Triolo, “Evaluation of coatings and materials for future radiators,” in *SAE Technical Paper Series*, ser. SAE Technical Paper Series. SAE International400 Commonwealth Drive, Warrendale, PA, United States, 2006.

[40] J. A. Fernández Benítez and C. Corrochano Sánchez, *Cuadernos de Transmision de Calor*. Madrid: Universidad Politécnica De Madrid, pp. 4–13, 2012.

[41] D. G. Gilmore, W. K. Stuckey, and M. Fong, “Thermal surface finishes,” in *Spacecraft Thermal Control Handbook. Volume I: Fundamental Technologies*, D. G. Gilmore, Ed. El Segundo Calif.: Aerospace Press, 2002–2003.

[42] S. A. Wagner, “The apollo experience lessons learned for constellation lunar dust management,” *NASA/TP-2006-213726*, vol. 1, no. 1, 2006.

[43] M. Hasegawa and H. Babel, “Estimation of the end-of-life optical properties of z-93 thermal control coating for the space station freedom,” in *Materials Specialist Conference - Coating Technology for Aerospace Systems*. Reston, Virigina: American Institute of Aeronautics and Astronautics, 1992.

[44] M. Finckenor and J. I. Kleiman, “Misse thermal control materials with comparison to previous flight experiments,” in *AIP Conference Proceedings*. AIP, 2009, pp. 241–248.

[45] I. A. Crawford and K. H. Joy, “Lunar exploration: opening a window into the history and evolution of the inner solar system,” *Philosophical transactions. Series A, Mathematical, physical, and engineering sciences*, vol. 372, no. 2024, p. 20130315, 2014.

[46] J. L. Carter, “Lunar material resources: An overview,” in *Space resources. Volume 3: Materials*, M. F. Mckay, D. Mckay, and M. Duke, Eds., 1992.

[47] D. S. McKay, G. Heiken, A. Basu, G. Blanford, S. Simon, R. Reedy, B. M. French, and J. Papike, “The lunar regolith,” in *Lunar sourcebook: A user’s guide to the moon*, G. Heiken, D. Vaniman, and B. M. French, Eds. Cambridge England and New York: Cambridge University Press, 1991, p. 285.

[48] C. Schwandt, J. A. Hamilton, D. J. Fray, and I. A. Crawford, “The production of oxygen and metal from lunar regolith,” *Planetary and Space Science*, vol. 74, no. 1, pp. 49–56, 2012.

[49] G. Heiken, D. Vaniman, and B. M. French, Eds., *Lunar sourcebook: A user's guide to the moon*. Cambridge England and New York: Cambridge University Press, 1991.

[50] B. L. Jolliff, M. A. Wieczorek, C. K. Shearer, and C. R. Neal, *New Views of the Moon*. De Gruyter, 2006.

[51] V. Badescu, *Moon: Prospective Energy and Material Resources*. Springer Berlin Heidelberg, 2012.

[52] R. Jaumann, H. Hiesinger, M. Anand, I. A. Crawford, R. Wagner, F. Sohl, B. L. Jolliff, F. Scholten, M. Knapmeyer, H. Hoffmann, H. Hussmann, M. Grott, S. Hempel, U. Köhler, K. Krohn, N. Schmitz, J. Carpenter, M. Wieczorek, T. Spohn, M. S. Robinson, and J. Oberst, "Geology, geochemistry, and geophysics of the moon: Status of current understanding," *Planetary and Space Science*, vol. 74, no. 1, pp. 15–41, 2012.

[53] W. D. Carrier, G. R. Olhoeft, and W. W. Mendell, "Physical properties of the lunar surface," in *Lunar sourcebook: A user's guide to the moon*, G. Heiken, D. Vaniman, and B. M. French, Eds. Cambridge England and New York: Cambridge University Press, 1991, pp. 475–594.

[54] G. H. Just, K. Smith, K. H. Joy, and M. J. Roy, "Parametric review of existing regolith excavation techniques for lunar in situ resource utilisation (isru) and recommendations for future excavation experiments," *Planetary and Space Science*, vol. 180, p. 104746, 2020.

[55] D. Stoeser, D. Rickman, and S. Wilson, "Design and specifications for the highland regolith prototype simulants nu-lht-1m and -2m."

[56] D. Vaniman, R. Reedy, G. Heiken, G. R. Olhoeft, and W. W. Mendell, "The lunar environment," in *Lunar sourcebook: A user's guide to the moon*, G. Heiken, D. Vaniman, and B. M. French, Eds. Cambridge England and New York: Cambridge University Press, 1991, pp. 27–60.

[57] L. A. Taylor, C. M. Pieters, and D. Britt, "Evaluations of lunar regolith simulants," *Planetary and Space Science*, vol. 126, pp. 1–7, 2016.

[58] National Aeronautics and Space Administration, "Lola gdr information in polar stereographic projection for the south pole," 2021-07-02. [Online]. Available: http://imbrium.mit.edu/BROWSE/LOLA_GDR/POLAR/SOUTH_POLE/ [Last accessed: 2021-07-02]

[59] S. S. Schreiner, J. A. Dominguez, L. Sibille, and J. A. Hoffman, "Thermophysical property models for lunar regolith," *Advances in Space Research*, vol. 57, no. 5, pp. 1209–1222, 2016.

[60] P. O. Hayne, J. L. Bandfield, M. A. Siegler, A. R. Vasavada, R. R. Ghent, J.-P. Williams, B. T. Greenhagen, O. Aharonson, C. M. Elder, P. G. Lucey, and D. A. Paige, "Global regolith thermophysical properties of the moon from the diviner

lunar radiometer experiment," *Journal of Geophysical Research: Planets*, vol. 122, no. 12, pp. 2371–2400, 2017.

[61] R. Morris, "Origins and size distribution of metallic iron particles in the lunar regolith," in *Proceedings of the Lunar and Planetary Science Conference 11*, 1980.

[62] K. M. Cannon and D. T. Britt, "A geologic model for lunar ice deposits at mining scales," *Icarus*, vol. 347, p. 113778, 2020.

[63] D. Schrunk, B. L. Sharpe, Cooper Bonnie L., and M. Thangavelu, *The Moon: Resources, Future Development, and Settlement*, ser. Springer Praxis Books. New York: Praxies Publishing Ltd, Chichester, UK, p. 53, 2007.

[64] F. S. Johnson, J. M. Carroll, and D. E. Evans, "Vacuum measurements on the lunar surface," *Journal of Vacuum Science and Technology*, vol. 9, no. 1, pp. 450–456, 1972.

[65] R. Honig, "Vapor pressure data for the more common elements," *RCA Review*, vol. RB–104, no. 1, 1957.

[66] D. Kornuta, A. Abbud-Madrid, J. Atkinson, J. Barr, G. Barnhard, D. Bienhoff, B. Blair, V. Clark, J. Cyrus, B. DeWitt, C. Dreyer, B. Finger, J. Goff, K. Ho, L. Kelsey, J. Keravala, B. Kutter, P. Metzger, L. Montgomery, P. Morrison, C. Neal, E. Otto, G. Roesler, J. Schier, B. Seifert, G. Sowers, P. Spudis, M. Sundahl, K. Zacny, and G. Zhu, "Commercial lunar propellant architecture: A collaborative study of lunar propellant production," *REACH*, vol. 13, p. 100026, 2019.

[67] A. Ghosh and J.-j. Favier, "Solar sintering on lunar regolith simulant (jsc-1) for 3d printing," in *67th International Astronautical Congress (IAC)*, 2016.

[68] A. Meurisse, A. Makaya, C. Willsch, and M. Sperl, "Solar 3d printing of lunar regolith," *Acta Astronautica*, vol. 152, pp. 800–810, 2018.

[69] K. Skonieczny, D. S. Wettergreen, and W. R. Whittaker, "Advantages of continuous excavation in lightweight planetary robotic operations," *The International Journal of Robotics Research*, vol. 35, no. 9, pp. 1121–1139, 2016.

[70] R. P. Mueller, R. E. Cox, T. Ebert, J. D. Smith, J. M. Schuler, and A. J. Nick, "Regolith advanced surface systems operations robot (rassor)," in *2013 IEEE Aerospace Conference*. IEEE, 2013, pp. 1–12.

[71] R. P. Mueller, J. D. Smith, J. M. Schuler, A. J. Nick, N. J. Gelino, K. W. Leucht, I. I. Townsend, and A. G. Dokos, "Design of an excavation robot: Regolith advanced surface systems operations robot (rassor) 2.0," in *Earth and Space 2016*, R. B. Malla, J. H. Agui, and P. J. van Susante, Eds. Reston, VA: American Society of Civil Engineers, 2016, pp. 163–174.

[72] I. Townsend, A. C. Muscatello, D. Dickson, L. Sibille, A. Nick, K. Leucht, and G. Tamasy, "Mars isru pathfinder regolith autonomous operations - modeling and

systems integration," in *AIAA SPACE and Astronautics Forum and Exposition*. Reston, Virginia: American Institute of Aeronautics and Astronautics, 2017.

[73] J. M. Schuler, J. D. Smith, R. P. Mueller, and A. J. Nick, "Rassor, the reduced gravity excavator," in *LUNAR ISRU 2019: Developing a New Space Economy*, 2019. [Online]. Available: https://www.hou.usra.edu/meetings/lunarisru2019/pdf/5061.pdf [Last accessed: 2021-08-23]

[74] National Aeronautics and Space Administration, "Regolith advanced surface systems operations robot (rassor) excavator," 11-06-2021. [Online]. Available: https://technology.nasa.gov/patent/KSC-TOPS-7 [Last accessed: 11-06-2021]

[75] S. Weißenböck and E. Fimbinger, "Our contribution to the nasa rassor bucket drum design challenge," *BHM Berg- und Hüttenmännische Monatshefte*, vol. 166, no. 2, pp. 104–111, 2021.

[76] M. S. Anderson, M. Ewert, and J. Keener, "Life support baseline values and assumptions document," *NASA/TP–2015–218570*, vol. 1, no. 1, pp. 25, 36, 39, 68, 2018.

[77] R. J. Williams, D. S. McKay, D. Giles, and T. E. Bunch, "Mining and beneficiation of lunar ores," in *Space Resources and Space Settlements*, G. K. O'Neill, J. Billigham, W. Gilbreath, and B. O'Leary, Eds. Washington, D.C.: NASA SP-428, 1979, pp. 219–229.

[78] J. N. Rasera, J. J. Cilliers, J. A. Lamamy, and K. Hadler, "The beneficiation of lunar regolith for space resource utilisation: A review," *Planetary and Space Science*, vol. 186, p. 104879, 2020.

[79] K. Zacny, B. Betts, M. Hedlund, P. Long, M. Gramlich, K. Tura, P. Chu, A. Jacob, and A. Garcia, "Planetvac: Pneumatic regolith sampling system," in *2014 IEEE Aerospace Conference*. IEEE, 2014, pp. 1–8.

[80] M. G. Shaw, G. A. Brooks, M. A. Rhamdhani, A. R. Duffy, and M. I. Pownceby, "Thermodynamic modelling of ultra-high vacuum thermal decomposition for lunar resource processing," *Planetary and Space Science*, vol. 204, p. 105272, 2021.

[81] M. A. Gibson and C. W. Knudsen, "Apparatus for manufacture of oxygen from lunar ilmenite," Patent US5 536 378, 1996. [Online]. Available: https://patents.google.com/patent/US5536378A/en [Last accessed: 2021-07-09]

[82] M. Berggren, R. Zubrin, P. Jonscher, and J. Kilgore, "Lunar soil particle separator," in *49th AIAA Aerospace Sciences Meeting including the New Horizons Forum and Aerospace Exposition*. Reston, Virigina: American Institute of Aeronautics and Astronautics, 2011.

[83] M. Adachi, H. Moroka, H. Kawamoto, S. Wakabayashi, and T. Hoshino, "Particle-size sorting system of lunar regolith using electrostatic traveling wave," *Journal of Electrostatics*, vol. 89, pp. 69–76, 2017.

[84] A. Wilkinson, “Size beneficiation of regolith for simplicity and efficiency,” in *Space Resources Roundtable and Planetary & Terrestrial Mining Sciences Symposium*, 2011.

[85] M. Berggren and R. Zubrin, “Moon to mars oxygen and steel technology,” in *Space Resources Roundtable and Planetary & Terrestrial Mining Sciences Symposium*, 2021.

[86] J. J. Cilliers, J. N. Rasera, and K. Hadler, “Estimating the scale of space resource utilisation (sru) operations to satisfy lunar oxygen demand,” *Planetary and Space Science*, vol. 180, p. 104749, 2020.

[87] K. Hadler, J. N. Rasera, R. Cruise, Y. Yu, J. Witchalls, S. Starr, and J. J. Cilliers, “Beneficiation of lunar regolith: Progress and challenges.” in *Space Resources Roundtable and Planetary & Terrestrial Mining Sciences Symposium*, 2021.

[88] L. A. Haskin and P. Warren, “Lunar chemistry,” in *Lunar sourcebook: A user’s guide to the moon*, G. Heiken, D. Vaniman, and B. M. French, Eds. Cambridge England and New York: Cambridge University Press, 1991, pp. 357–475.

[89] D. S. McKay and R. J. Williams, “A geologic assessment of potential lunar ores,” in *Space Resources and Space Settlements*, G. K. O’Neill, J. Billigham, W. Gilbreath, and B. O’Leary, Eds. Washington, D.C.: NASA SP-428, 1979.

[90] E. Monchieri, S. Hovland, M. Masi, A. Sliepcevich, M. Lavagna, T. Hoppenbrouwers, and F. Venditti, “Esa lunar in-situ resource utilisation (isru) breadboarding activities and conceptual design for a lunar demonstrator,” in *61st International Astronautical Congress (IAC)*, 2010.

[91] H. N. Friedlander, “An analysis of alternate hydrogen sources for lunar manufacture,” in *Lunar Bases and Space Activities of the 21st Century*, W. W. Mendell, Ed., 1985, p. 611.

[92] R. Balasubramaniam, U. Hegde, S. Gokoglu, and M. S. El-Genk, “Carbothermal processing of lunar regolith using methane,” in *AIP Conference Proceedings*. AIP, 2008, pp. 157–161.

[93] W. Steurer, “Vapor phase pyrolysis,” in *Space resources. Volume 3: Materials*, M. F. Mckay, D. Mckay, and M. Duke, Eds., 1992.

[94] C. Senior, “Lunar oxygen production by pyrolysis,” in *Resources of near-earth space*, J. S. Lewis, M. S. Matthews, and M. L. Guerrieri, Eds., 1993.

[95] B. B. Carr, “Recovery of water or oxygen by rduction of lunar rock,” *AIAA Journal*, vol. 1, no. 4, pp. 921–924, 1963.

[96] M. A. Gibson, C. W. Knudsen, D. J. Brueneman, C. C. Allen, H. Kanamori, and D. S. McKay, “Reduction of lunar basalt 70035: Oxygen yield and reaction product analysis,” *Journal of Geophysical Research*, vol. 99, no. E5, p. 10887, 1994.

[97] C. C. Allen, R. V. Morris, and D. S. McKay, “Oxygen extraction from lunar soils and pyroclastic glass,” *Journal of Geophysical Research*, vol. 101, no. E11, pp. 26 085–26 095, 1996.

[98] H. Yoshida, T. Watanabe, H. Kanamori, T. Yoshida, Ogiwara S., and Eguchi K., “Experimental study on water production by hydrogen reduction of lunar soil simulant in a fixed bed reactor,” in *Second Space Resources Roundtable*, 2000.

[99] U. Hegde, R. Balasubramaniam, and S. Gokoglu, “Development and validation of a model for hydrogen reduction of jsc-1a,” in *47th AIAA Aerospace Sciences Meeting including The New Horizons Forum and Aerospace Exposition*. Reston, Virigina: American Institute of Aeronautics and Astronautics, 2009.

[100] G. B. Sanders and W. E. Larson, “Progress made in lunar in situ resource utilization under nasa’s exploration technology and development program,” *Journal of Aerospace Engineering*, vol. 26, no. 1, pp. 5–17, 2013.

[101] T. Denk, “Full-scale terrestrial demonstrator for lunar ilmenite reduction with concentrated solar power,” in *69th International Astronautical Congress (IAC)*, 2018.

[102] H. M. Sargeant, “Water from lunar regolith: Reduction by hydrogen for a small-scale demonstration of in situ resource utilisation for the moon,” Ph.D. dissertation, The Open University, pp. 30–31, 2020. [Online]. Available: http://oro.open.ac.uk/73654/ [Last accessed: 2021-07-09]

[103] L. Schlüter and A. Cowley, “Review of techniques for in-situ oxygen extraction on the moon,” *Planetary and Space Science*, vol. 181, p. 104753, 2020.

[104] I. Mellor and G. Doughty, “Novel and emerging routes for titanium powder production - an overview,” *Key Engineering Materials*, vol. 704, pp. 271–281, 2016.

[105] H. Kanematsu, N. Wada, and T. Oki, “Emissivity of titanium oxide powder coating & its structure,” *Plating and Surface Finishing*, vol. 90, pp. 61–65, 2003.

[106] L. Schlüter, A. Cowley, Y. Pennec, and M. Roux, “Gas purification for oxygen extraction from lunar regolith,” *Acta Astronautica*, vol. 179, pp. 371–381, 2021.

[107] A. C. de Paula, J. R. Henríquez, and F. A. Figueiredo, “Dimensioning a cyclone separator for circulating fluidized bed gasifier: Validation of a procedure,” *Heat Transfer Engineering*, vol. 41, no. 15-16, pp. 1305–1314, 2020.

[108] J. G. Mantovani and I. I. Townsend, “Planetary regolith delivery systems for isru,” *Journal of Aerospace Engineering*, vol. 26, no. 1, pp. 169–175, 2013.

[109] L. Carter, D. Tabb, J. D. Tatara, and R. K. Mason, “Performance qualification test of the iss water processor assembly (wpa) expendables,” in *SAE Technical Paper Series*, ser. SAE Technical Paper Series. SAE International400 Commonwealth Drive, Warrendale, PA, United States, 2005.

[110] J. B. Holquist, P. Pasadilla, C. Bower, T. Cognata, P. Tewes, and L. Kelsey, “Analysis of a cold trap as a purification step for lunar water processing,” in *49th International Conference on Environmental Systems (ICES)*, 2020.

[111] S. M. Anthony, S. T. Jolley, and J. G. Captain, “Advanced water purification system for in situ resource utilization,” in *AIAA SPACE 2013 Conference and Exposition*. Reston, Virginia: American Institute of Aeronautics and Astronautics, 2013.

[112] J. B. Holquist, S. Gellenbeck, C. Bower, and P. Tewes, “Demonstration of paragon’s ionomer-membrane water processing (iwp) technology as a purification step for lunar water processing,” in *50th International Conference on Environmental Systems (ICES)*, 2021.

[113] B. Schreck, A. Feigel, and D. Pütz, “The life support trade off tool - listot,” 2021-07-09. [Online]. Available: https://wiki.tum.de/display/listot [Last accessed: 2021-07-09]

[114] B. Schreck, “Feasibility analysis of a life support architecture for an interplanetary transport ship,” M.Sc. Thesis, Technical University of Munich, 2017. [Online]. Available: https://mediatum.ub.tum.de/doc/1388335/1388335.pdf [Last accessed: 2021-07-09]

[115] A. Feigel, “Advancement of a trade-off tool for life support technologies and its application in proposing a life support architecture for the gateway,” M.Sc. Thesis, Technical University of Munich, 2019. [Online]. Available: https://mediatum.ub.tum.de/doc/1503234/1503234.pdf [Last accessed: 2021-07-09]

[116] W. F. Carroll, “Research on the use of space resources,” *JPL Publication*, vol. 83–36, no. 1, pp. 3.1–3.22, 1983.

[117] L. A. Haskin, R. O. Colson, D. J. Lindstrom, R. H. Lewis, and K. W. Semkow, “Electrolytic smelting of lunar rock for oxygen, iron, and silicon,” in *Lunar Bases and Space Activities of the 21st Century*, W. W. Mendell, J. W. Alred, L. S. Bell, M. J. Cintala, T. M. Crabb, R. H. Durrett, B. R. Finney, H. A. Franklin, J. R. French, and J. S. Greenberg, Eds., 1992, p. 411.

[118] P. Curreri, E. Ethridge, S. Hudson, T. Miller, R. Grugel, S. Sen, and D. Sadoway, “Process demonstration for lunar in situ resource utilization-molten oxide electrolysis,” *NASA/TM–2006–214600*, vol. 1, no. 1, 2006.

[119] E. Standish, “Design of a molten materials handling device for support of molten regolith electrolysis,” Ph.D. dissertation, The Ohio State University, 2010. [Online]. Available: https://etd.ohiolink.edu/apexprod/rws_etd/send_file/send?accession=osu1268975211&disposition=attachment [Last accessed: 2021-06-28]

[120] L. Sibille, D. Sadoway, A. Sirk, P. Tripathy, O. Melendez, E. Standish, J. Dominguez, D. Stefanescu, P. Curreri, and S. Poizeau, “Recent advances in scale-up development of molten regolith electrolysis for oxygen production in support of a lunar base,” in *47th AIAA Aerospace Sciences Meeting including The New Horizons Forum and Aerospace Exposition*. Reston, Virigina: American Institute of Aeronautics and Astronautics, 2009.

[121] L. Sibille, D. Sadoway, P. Tripathy, and E. Standish, “Performance testing of molten regolith electrolysis and transfer of molten material for oxygen and metals production on the moon,” in *48th AIAA Aerospace Sciences Meeting Including the New Horizons Forum and Aerospace Exposition*. Reston, Virigina: American Institute of Aeronautics and Astronautics, 2010.

[122] L. Sibille and J. Dominguez, “Joule-heated molten regolith electrolysis reactor concepts for oxygen and metals production on the moon and mars,” in *50th AIAA Aerospace Sciences Meeting including the New Horizons Forum and Aerospace Exposition*. Reston, Virigina: American Institute of Aeronautics and Astronautics, 2012.

[123] A. H. Sirk, D. R. Sadoway, and L. Sibille, “Direct electrolysis of molten lunar regolith for the production of oxygen and metals on the moon,” *ECS Transactions*, vol. 28, no. 6, pp. 367–373, 2010.

[124] A. Vai, J. Yurko, D. H. Wang, and D. Sadoway, “Molten oxide electrolysis for lunar oxygen generation using in-situ resources,” 2010.

[125] D. Wang, A. J. Gmitter, and D. R. Sadoway, “Production of oxygen gas and liquid metal by electrochemical decomposition of molten iron oxide,” *Journal of The Electrochemical Society*, vol. 158, no. 6, p. E51, 2011.

[126] A. J. Gmitter, “The influence of inert anode material and electrolyte composition on the electrochemical production of oxygen from molten oxides,” M.Sc. Thesis, Massachusetts Institute of Technology, 2008. [Online]. Available: https://dspace.mit.edu/handle/1721.1/44211 [Last accessed: 2021-06-29]

[127] J. D. Paramore, “Candidate anode materials for iron production by molten oxide electrolysis,” M.Sc. Thesis, Massachusetts Institute of Technology, 2010. [Online]. Available: https://core.ac.uk/download/pdf/4427277.pdf [Last accessed: 2021-06-29]

[128] A. Shchetkovskiy, T. McKechnie, D. R. Sadoway, J. Paramore, O. Melendez, and P. A. Curreri, “Development and testing of high surface area iridium anodes for molten oxide electrolysis,” in *Earth and Space 2010*, G. Song and R. B. Malla, Eds. Reston, VA: American Society of Civil Engineers, 2010, pp. 1039–1045.

[129] A. Allanore, L. Yin, and D. R. Sadoway, “A new anode material for oxygen evolution in molten oxide electrolysis,” *Nature*, vol. 497, no. 7449, pp. 353–356, 2013.

[130] B. A. Lomax, M. Conti, N. Khan, N. S. Bennett, A. Y. Ganin, and M. D. Symes, “Proving the viability of an electrochemical process for the simultaneous extraction of oxygen and production of metal alloys from lunar regolith,” *Planetary and Space Science*, vol. 180, p. 104748, 2020.

[131] D. J. Fray, Farthing T. W., and G. Z. Chen, “Removal of oxygen from metal oxides and solid solutions by electrolysis in a fused salt,” Patent WO1 999 064 638A1, 1999. [Online]. Available: https://patents.google.com/patent/WO1999064638A1/en [Last accessed: 2021-07-11]

[132] G. Z. Chen, D. J. Fray, and Farthing T. W., “Direct electrochemical reduction of titanium dioxide to titanium in molten calcium chloride,” *Nature*, vol. 407, no. 6802, pp. 361–364, 2000.

[133] D. G. Kesterke, “Electrowinning oxygen from silicate rocks,” *Bureau of Mines Report of Investigations*, vol. 7587, no. 1, 1970.

[134] A. Liu, Z. Shi, X. Hu, B. Gao, and Z. Wang, “Lunar soil simulant electrolysis using inert anode for al-si alloy and oxygen production,” *Journal of The Electrochemical Society*, vol. 164, no. 2, pp. H126–H133, 2017.

[135] C. Schwandt, G. R. Doughty, and D. J. Fray, “The ffc-cambridge process for titanium metal winning,” *Key Engineering Materials*, vol. 436, pp. 13–25, 2010.

[136] M. Bertolini, L. Shaw, L. England, K. Rao, J. Deane, and J. Collins, “The ffc cambridge process for production of low cost titanium and titanium powders,” *Key Engineering Materials*, vol. 436, pp. 75–83, 2010.

[137] C. S. Ray, S. T. Reis, S. Sen, and J. S. O’Dell, “Jsc-1a lunar soil simulant: Characterization, glass formation, and selected glass properties,” *Journal of Non-Crystalline Solids*, vol. 356, no. 44-49, pp. 2369–2374, 2010.

[138] K. T. Kilby, S. Jiao, and D. J. Fray, “Current efficiency studies for graphite and sno2-based anodes for the electro-deoxidation of metal oxides,” *Electrochimica Acta*, vol. 55, no. 23, pp. 7126–7133, 2010.

[139] S. Jiao and D. J. Fray, “Development of an inert anode for electrowinning in calcium chloride–calcium oxide melts,” *Metallurgical and Materials Transactions B*, vol. 41, no. 1, pp. 74–79, 2010.

[140] L. Hu, Y. Song, J. Ge, S. Jiao, and J. Cheng, “Electrochemical metallurgy in cacl 2 -cao melts on the basis of tio 2 ·ruo 2 inert anode,” *Journal of The Electrochemical Society*, vol. 163, no. 3, pp. E33–E38, 2016.

[141] Di Hu, A. Dolganov, M. Ma, B. Bhattacharya, M. T. Bishop, and G. Z. Chen, “Development of the fray-farthing-chen cambridge process: Towards the sustainable production of titanium and its alloys,” *JOM*, vol. 70, no. 2, pp. 129–137, 2018.

[142] D. Vaughan and M. Conti, “Manufacturing apparatus and method,” Patent US20 190 275 589A1, 2019. [Online]. Available: https://patents.google.com/patent/us20190275589a1/en [Last accessed: 2021-07-20]

[143] J. Baasch, L. Windisch, F. Koch, S. Linke, E. Stoll, and C. Schilde, “Regolith as substitute mold material for aluminum casting on the moon,” *Acta Astronautica*, vol. 182, pp. 1–12, 2021.

[144] A. Ellery, P. Lowing, P. Wanjara, M. Kirby, I. Mellor, and G. Doughty, “Ffc cambridge process and metallic 3d printing for deep in-situ resource utilization - a match made on the moon,” in *68th International Astronautical Congress (IAC)*, 2017.

[145] J. S. Lewis, T. D. Jones, and W. H. Farrand, “Carbonyl extraction of lunar and asteroidal metals,” in *Engineering, Construction, and Operations in Space*, 1988, pp. 111–122.

[146] J. S. Lewis, “Extraction of volatiles and metals from extraterrestrial materials,” in *NASA Space Engineering Research Center for Utilization of Local Planetary Resources*, K. Ramohalli and J. S. Lewis, Eds., 1992.

[147] S. Sastri, M. B. Duke, and L. A. Haskin, “Manufacturing and fabrication,” in *Space resources. Volume 3: Materials*, M. F. Mckay, D. Mckay, and M. Duke, Eds., 1992.

[148] D. F. Bowersox, “Processes for metal extraction,” in *Space resources. Volume 3: Materials*, M. F. Mckay, D. Mckay, and M. Duke, Eds., 1992.

[149] A. Visnapuu, B. C. Marek, and J. W. Jensen, *Conversion of ilmenite to rutile by a carbonyl process*. Washington D.C.: U.S. Dept. of Interior, Bureau of Mines, 1973.

[150] W. C. Jekin, “Production of steels products in space using isru iron sources and carbonyl metallurgy,” in *Space Resources Roundtable VII*, 2005.

[151] M. McKellar, C. Stoots, M. Sohal, L. Mulloth, B. Luna, and M. Abney, “The concept and analytical investigation of co2 and steam co-electrolysis for resource utilization in space exploration,” in *40th International Conference on Environmental Systems (ICES)*. Reston, Virigina: American Institute of Aeronautics and Astronautics, 2010.

[152] *BPVC Section VIII - Rules for Construction of Pressure Vessels Division 1*. ASME, 2021.

[153] J. E. Japka, “Microstructure and properties of carbonyl iron powder,” *JOM*, vol. 40, no. 8, pp. 18–21, 1988.

[154] A. Colaprete, P. Schultz, J. Heldmann, D. Wooden, M. Shirley, K. Ennico, B. Hermalyn, W. Marshall, A. Ricco, R. C. Elphic, D. Goldstein, D. Summy, G. D. Bart, E. Asphaug, D. Korycansky, D. Landis, and L. Sollitt, “Detection of water in the lcross ejecta plume,” *Science (New York, N.Y.)*, vol. 330, no. 6003, pp. 463–468, 2010.

[155] M. Berggren, (personal communication, June 24th, 2021).

[156] J. Matchett, “Production of lunar oxygen through vacuum pyrolysis,” M.Sc. Thesis, The George Washington University School of Engineering and Applied Science, 2006. [Online]. Available: https://citeseerx.ist.psu.edu/viewdoc/download?doi=10.1.1.1000.3201&rep=rep1&type=pdf [Last accessed: 2021-08-21]

[157] K. Liu, J. J. Wu, W. H. Ma, B. Yang, X. Yang, L. X. Kong, X. F. Zeng, and Y. N. Dai, “Calculation of ternary si-fe-al phase equilibrium in vacuum distillation by molecular interaction volume model,” *Journal of Mining and Metallurgy, Section B: Metallurgy*, vol. 50, no. 2, pp. 171–176, 2014.

[158] K. Liu, J. Wu, K. Wei, W. Ma, K. Xie, S. Li, B. Yang, and Y. Dai, “Application of molecular interaction volume model on removing impurity aluminum from metallurgical grade silicon by vacuum volatilization,” *Vacuum*, vol. 114, pp. 6–12, 2015.

[159] D. R. Criswell, “Extraterrestrial materials processing and construction,” *NSR 09-051-001*, vol. 1, no. 24, pp. 27–33, 1980.

[160] F. Zaera, “A kinetic study of the chemical vapor deposition of iron films using iron pentacarbonyl,” *Langmuir*, vol. 7, no. 6, pp. 1188–1191, 1991.

[161] P. Zhang, E. Mohimi, T. K. Talukdar, J. R. Abelson, and G. S. Girolami, “Iron cvd from iron pentacarbonyl: Growth inhibition by co dissociation and use of ammonia to restore constant growth,” *Journal of Vacuum Science & Technology A: Vacuum, Surfaces, and Films*, vol. 34, no. 5, p. 051518, 2016.

[162] F. Klocke, *Manufacturing Processes 4*. Berlin, Heidelberg: Springer Berlin Heidelberg, p. 175, 2013.

[163] K. D. Grossman, T. S. Sakthivel, L. Sibille, J. G. Mantovani, and S. Seal, “Regolith-derived ferrosilicon as a potential feedstock material for wire-based additive manufacturing,” *Advances in Space Research*, vol. 63, no. 7, pp. 2212–2219, 2019.

[164] A. Goulas and R. J. Friel, “3d printing with moondust,” *Rapid Prototyping Journal*, vol. 22, no. 6, pp. 864–870, 2016.

[165] M. Isachenkov, S. Chugunov, I. Akhatov, and I. Shishkovsky, “Regolith-based additive manufacturing for sustainable development of lunar infrastructure – an overview,” *Acta Astronautica*, vol. 180, pp. 650–678, 2021.

[166] T. D. Ngo, A. Kashani, G. Imbalzano, K. T. Nguyen, and D. Hui, “Additive manufacturing (3d printing): A review of materials, methods, applications and challenges,” *Composites Part B: Engineering*, vol. 143, pp. 172–196, 2018.

[167] E. Sacco and S. K. Moon, “Additive manufacturing for space: status and promises,” *The International Journal of Advanced Manufacturing Technology*, vol. 105, no. 10, pp. 4123–4146, 2019.

[168] H. Williams and E. Butler-Jones, “Additive manufacturing standards for space resource utilization,” *Additive Manufacturing*, vol. 28, pp. 676–681, 2019.

[169] E. Lucon, K. Abiko, M. Lambrecht, and B. Rehmer, “Tensile properties of commercially pure, high purity and ultra high purity iron: Results of an international round-robin.”

[170] J. Helsing and G. Grimvall, “Thermal conductivity of cast iron: Models and analysis of experiments,” *Journal of Applied Physics*, vol. 70, no. 3, pp. 1198–1206, 1991.

[171] G. Wang and Y. Li, “Effects of alloying elements and temperature on thermal conductivity of ferrite,” *Journal of Applied Physics*, vol. 126, no. 12, p. 125118, 2019.

[172] W. Schatt, K.-P. Wieters, and B. Kieback, *Pulvermetallurgie: Technologien und Werkstoffe*. Springer Berlin Heidelberg, pp. 41–43, 2007.

[173] G. Walther, T. Büttner, B. Kieback, T. Weissgärber, and M. Hoffmann, “New processing route for production of fine spherical iron powder,” in *EuroPM 2015*, 2015.

[174] S. T. Lin and R. M. German, “Mechanical properties of fully densified injection-molded carbonyl iron powder,” *Metallurgical Transactions A*, vol. 21, no. 9, pp. 2531–2538, 1990.

[175] V. M. Blázquez Martínez, V. Lorenzo Esteban, and B. Del Río López, *Ingeniería y ciencia de los materiales metálicos*. Madrid: Dextra Editorial S.L, pp. 191–192, 333–359, 2014.

[176] T. Mohri, Y. Chen, M. Kohyama, S. Ogata, A. Saengdeejing, S. K. Bhattacharya, M. Wakeda, S. Shinzato, and H. Kimizuka, “Mechanical properties of fe-rich si alloy from hamiltonian,” *npj Computational Materials*, vol. 3, no. 1, 2017.

[177] R. P. Mueller, L. Sibille, J. Dunn, S. Seal, and K. D. Grossman, “Advanced feedstock for additive manufacturing from molten regolith electrolysis (mre),” 2018.

[178] K. Wei, D. Zheng, W. Ma, B. Yang, and Y. Dai, “Study on al removal from mg-si by vacuum refining,” *Silicon*, vol. 7, no. 3, pp. 269–274, 2015.

[179] M. G. Kalhapure and P. M. Dighe, “Impact of silicon content on mechanical properties of aluminum alloys,” *International Journal of Science and Research (IJSR)*, vol. 4, no. 6, pp. 38–40, 2015.

[180] A. S. Zhilin, L. Jianguo, V. R. Yalunina, V. V. Tokarev, V. A. Bykov, and V. P. Shveikin, “Influence of silicon on temperature dependence of thermal conductivity of al–si–fe alloys,” *KnE Engineering*, vol. 3, no. 5, p. 298, 2018.

[181] M. Killian, “Thermal moon simulator - thermos,” 2021-08-20. [Online]. Available: https://www.asg.ed.tum.de/lrt/forschung/exploration-technologies/thermos [Last accessed: 2021-08-20]

[182] D. Pütz, C. Olthoff, J. Schnaitmann, and U. Walter, “Development status of the virtual habitat (v-hab) simulation system,” in *49th International Conference on Environmental Systems (ICES)*, 2019.

[183] Z. Y. Liu, C. Li, X. Y. Fang, and Y. B. Guo, “Energy consumption in additive manufacturing of metal parts,” *Procedia Manufacturing*, vol. 26, pp. 834–845, 2018.

[184] D. Linne, “Employing isru models to improve hardware designs,” in *48th AIAA Aerospace Sciences Meeting Including the New Horizons Forum and Aerospace*

Exposition. Reston, Virigina: American Institute of Aeronautics and Astronautics, 2010.

[185] A. Chepko, O. de Weck, W. Crossley, E. Santiago-Maldonado, and D. Linne, "A modeling framework for applying discrete optimization to system architecture selection and application to in-situ resource utilization," in *12th AIAA/ISSMO Multidisciplinary Analysis and Optimization Conference*. Reston, Virigina: American Institute of Aeronautics and Astronautics, 2008.

[186] A. Chepko, O. de Weck, D. Linne, E. Santiago-Maldonado, and W. Crossley, "Architecture modeling of in-situ oxygen production and its impacts on lunar campaigns," in *AIAA SPACE 2008 Conference & Exposition*. Reston, Virigina: American Institute of Aeronautics and Astronautics, 2008.

[187] A. Chepko, "Technology selection and architecture optimization of in-situ resource utilization systems," M.Sc. Thesis, Massachusetts Institute of Technology, 2009. [Online]. Available: https://dspace.mit.edu/handle/1721.1/50605 [Last accessed: 2021-09-17]

[188] G. J. Janz, *Thermodynamic and transport properties for molten salts: correlation equations for critically evaluated density, surface tension, electrical conductance, and viscosity data*. New York: American Chemical Society and the American Institute of Physics for the National Bureau of Standards, p. 23, 1988.

[189] A. S. Agazhanov, D. A. Samoshkin, and Y. M. Kozlovskii, "Thermophysical properties of inconel 718 alloy," *Journal of Physics: Conference Series*, vol. 1382, p. 012175, 2019.

[190] D. G. Donabedian, D. G. Gilmore, J. W. Stultz, G. T. Tsuyuki, and E. I. Lin, "Insulation," in *Spacecraft Thermal Control Handbook. Volume I: Fundamental Technologies*, D. G. Gilmore, Ed. El Segundo Calif.: Aerospace Press, 2002–2003.

A Molten Salt Electrolysis Model Parameters

This appendix presents the model parameters used in Section 4.4.3 to calculate the mass, volume, power, and cooling requirements of the MSE assembly. Table A–1 shows the parameter descriptions, their values, and the reference from which they were obtained, if applicable.

Tab. A–1: Molten salt electrolysis model parameters.

Parameter	Value	Unit	Reference
Annual O_2 production (N)	15	t/y	-
$CaCl_2$ density (ρ_{CaCl_2})	2009	kg/m^3	[188]
Downtime ($t_{downtime}$)	30	min	-
Duty cycle (τ)	0.75	-	-
Electrolysis cell voltage (U_{cell})	3	V	[20]
Electrolysis current efficiency (η_I)	0.35	-	[135, 141, 130]
Electrolysis time ($t_{electrolysis}$)	45	h	[130]
Electrolyte ratio (λ_{CaCl_2})	53.34	kg/kg	[130]
Environment temperature (T_{env})	293	K	-
Enthalpy of formation for regolith oxides ($\Delta H_{f,oxide}$)	-	J/mol	[59]
Faraday constant (F)	96485	(A·s)/mol	-
Gibbs free energy for regolith oxides (ΔG_{oxide})	-	J/mol	[59]
Inconel thermal conductivity ($k_{Inconel}$)	20.5	W/(m·K)	[189]
Inconel thickness ($d_{Inconel}$)	0.02	m	-
MLI effective emittance ($\varepsilon_{eff_{MLI,preheater}}$)	0.005	-	[190]
MLI effective emittance ($\varepsilon_{eff_{MLI,reactor}}$)	0.0175	-	[190]
MLI emittance (ε_{MLI})	0.5	-	[190] for Kapton
O_2 yield (λ_{O_2})	0.44	kg/kg	Table 3–3
Oxide weight fraction (w_{oxide})	-	kg/kg	Table 3–2
Outer space temperature (T_∞)	3	K	-
Reactor temperature ($T_{reactor}$)	1223	K	[130]
Regolith density ($\rho_{Regolith}$)	1500	kg/m^3	[59]
Regolith specific heat dependency with temperature ($C_{p,Regolith}(T)$)	-	J/(kg·K)	[59]
Stefan-Boltzmann constant (σ)	$5.67 \cdot 10^{-8}$	kg/(s^3·K^4)	-

B Thermal Simulations Parameters

This appendix presents the model parameters used in Chapter 7 to perform the coupled steady-state thermo-fluid dynamic simulations of the radiator concepts described in Section 2.3.1. Table B–1 shows the parameter descriptions, their values, and the reference from which they were obtained, if applicable.

Tab. B–1: Thermal simulations parameters.

Parameter	Value	Unit	Reference
Inlet mass flow ($\dot{m}_{inlet}$)	140	kg/h	[35]
Inlet temperature (T_{inlet})	276	K	[31]
NH_3 density (ρ_{NH_3})	610	kg/m^3	Ansys^{TM} Fluent
NH_3 themal conductivity (k_{NH_3})	0.493	W/(m·K)	Ansys^{TM} Fluent
Outer space temperature (T_∞)	3	K	-
Outlet backflow temperature (T_{outlet})	275.5	K	[35]
Thermal conductivity carbonyl Fe ($k_{Carbonyl}$)	73	W/(m·K)	Section 5.1
Thermal conductivity distilled Al (k_{Al})	190	W/(m·K)	Section 5.5
Thermal conductivity Fe-Si alloy ($k_{Fe\text{-}Si}$)	23	W/(m·K)	Section 5.3
Thermal conductivity highlands metallic mixture (k_{Mix})	15	W/(m·K)	Section 5.4
Thermal conductivity melt-refined Fe ($k_{Melt\text{-}refined\ Fe}$)	34	W/(m·K)	Section 5.2
Regolith infrared emittance ($\varepsilon_{Regolith}$)	0.95	-	[60]
Regolith thermal conductivity ($k_{Regolith}$)	0.001	W/(m·K)	[59]
Regolith temperature ($T_{Regolith}$)	120	K	Figure 2–5
Z-93 emittance ($\varepsilon_{Z\text{-}93}$)	0.92	-	Section 2.3.2

C ESM Input Data

This appendix presents the mass, volume, power, and cooling requirements of the in-situ material production concepts defined in Chapter 6. The requirements are used in Chapter 8 to calculate the equivalent system mass. The values reported for each component of the ISRU process chain are based on the summary tables provided in Chapter 4.

In the excavation stage, a single RASSOR can excavate more than 1000 t/y of regolith. Although a lower excavation rate would suffice for most of the in-situ material production concepts, a single RASSOR is considered to be the minimum unit that can be transported from Earth.

The thermal powers presented in the summary tables of Chapter 4 have been converted to electric powers assuming a heater efficiency of 30%. This conversion allows a direct ESM transformation between kW consumed and kg of solar voltaic cells required.

If the radiator is placed above the lunar surface, the entire area must be coated with Z-93 white paint. However, if the radiator lays on the lunar surface, only half of the radiator area must be coated with Z-93 white paint.

Tab. C–1: ESM input data for concept S1. The ISRU process chain produces 15 t/y of O_2 and 8.9 t/y of carbonyl Fe to manufacture, within a year, a state-of-the-art radiator placed above the lunar surface. The state-of-the-art radiator rejects 46.1 kW of heat.

	RASSOR (60900 t/y of highlands regolith)			
	Mass (kg)	**Volume (m^3)**	**Power (kW)**	**Cooling (kW)**
Excavation Total	5280	80	25.60	0
	Ilmenite Enrichment (197.5 t/y of $FeTiO_3$-rich regolith)			
	Mass (kg)	**Volume (m^3)**	**Power (kW)**	**Cooling (kW)**
Particle Size Separator	1390	1.39	0	0
Weak-Field Magnetic Separator	65	0.10	0.65	0
Strong-field Magnetic Separator	2086	2.06	1.90	0
Beneficiation Total	3541	3.55	2.55	0
	Ilmenite Reduction with H_2 (15 t/y of O_2)			
	Mass (kg)	**Volume (m^3)**	**Power (kW)**	**Cooling (kW)**
H_2 Reduction Reactor	2896	1.83	37.17	0
Cyclone Unit	34	0.01	0	0
Water Purification Unit	705	5.57	0	9.67
SFPW	875	1.22	11.75	0.40
O_2 Extraction Total	4510	8.63	48.92	10.07
	Carbonylation (8.9 t/y of Fe)			
	Mass (kg)	**Volume (m^3)**	**Power (kW)**	**Cooling (kW)**
Carbonyl Reactor	240	0.28	2.59	0
CHX	49	0.38	0	0.67
NH_3	22[1]	0.08[2]	0	0
H_2S	60[1]	0.11[2]	0	0
CSOEC	28	0.04	0.64	0.14
Metal Processing Total	399	0.89	3.23	0.81
	Radiator Surface Finish (225 m^2 of radiating area)			
	Mass (kg)	**Volume (m^3)**	**Power (kW)**	**Cooling (kW)**
Z-93 Coating	43	0.03	0	0
Post-Processing Total	43	0.03	0	0
	Mass (kg)	**Volume (m^3)**	**Power (kW)**	**Cooling (kW)**
ISRU Process Chain Total	**13773**	**93.10**	**80.30**	**10.88**

[1] NH_3 and H_2S are consumables. The units of the represented values are (kg/y).
[2] NH_3 and H_2S are consumables. The units of the represented values are (m^3/y).

Tab. C–2: ESM input data for concept T1. The ISRU process chain produces 15 t/y of O_2 and 9 t/y of carbonyl Fe to manufacture, within a year, a tubular radiator placed above the lunar surface. The tubular radiator rejects 46.2 kW of heat.

	RASSOR (60900 t/y of highlands regolith)			
	Mass (kg)	**Volume (m^3)**	**Power (kW)**	**Cooling (kW)**
Excavation Total	5280	80	25.60	0
	Ilmenite Enrichment (197.5 t/y of $FeTiO_3$-rich regolith)			
	Mass (kg)	**Volume (m^3)**	**Power (kW)**	**Cooling (kW)**
Particle Size Separator	1390	1.39	0	0
Weak-Field Magnetic Separator	65	0.10	0.65	0
Strong-field Magnetic Separator	2086	2.06	1.90	0
Beneficiation Total	3541	3.55	2.55	0
	Ilmenite Reduction with H_2 (15 t/y of O_2)			
	Mass (kg)	**Volume (m^3)**	**Power (kW)**	**Cooling (kW)**
H_2 Reduction Reactor	2896	1.83	37.17	0
Cyclone Unit	34	0.01	0	0
Water Purification Unit	705	5.57	0	9.67
SFPW	875	1.22	11.75	0.40
O_2 Extraction Total	4510	8.63	48.92	10.07
	Carbonylation (9 t/y of Fe)			
	Mass (kg)	**Volume (m^3)**	**Power (kW)**	**Cooling (kW)**
Carbonyl Reactor	246	0.28	2.67	0
CHX	50	0.39	0	0.69
NH_3	23[1]	0.09[2]	0	0
H_2S	62[1]	0.11[2]	0	0
CSOEC	29	0.04	0.66	0.15
Metal Processing Total	410	0.91	3.33	0.84
	Radiator Surface Finish (239 m^2 of radiating area)			
	Mass (kg)	**Volume (m^3)**	**Power (kW)**	**Cooling (kW)**
Z-93 Coating	46	0.04	0	0
Post-Processing Total	46	0.04	0	0
	Mass (kg)	**Volume (m^3)**	**Power (kW)**	**Cooling (kW)**
ISRU Process Chain Total	**13787**	**93.13**	**80.40**	**10.91**

[1] NH_3 and H_2S are consumables. The units of the represented values are (kg/y).
[2] NH_3 and H_2S are consumables. The units of the represented values are (m^3/y).

Tab. C–3: ESM input data for concept S2. The ISRU process chain produces 15 t/y of O_2 and 6.7 t/y of Fe-Si alloys to manufacture, within a year, a state-of-the-art radiator placed above the lunar surface. The state-of-the-art radiator rejects 34.2 kW of heat.

	RASSOR (800 t/y of highlands regolith)			
	Mass (kg)	**Volume (m^3)**	**Power (kW)**	**Cooling (kW)**
Excavation Total	66	1.00	0.32	0
	FeO Enrichment (41.7 t/y of FeO-rich regolith)			
	Mass (kg)	**Volume (m^3)**	**Power (kW)**	**Cooling (kW)**
Particle Size Separator	170	0.17	0	0
Weak-Field Magnetic Separator	3	0.01	0.03	0
Strong-field Magnetic Separator	56	0.06	0.05	0
Beneficiation Total	229	0.24	0.08	0
	Molten Regolith Electrolysis (15 t/y of O_2 and 6.7 t/y of Fe-Si alloys)			
	Mass (kg)	**Volume (m^3)**	**Power (kW)**	**Cooling (kW)**
MRE Reactor	403	0.69	59.63	0
Anode	137.5[1]	0.006[2]	0	0
Cathode	99[1]	0.010[2]	0	0
Oxygen Purification Unit	30	0.005	0.82	0
Heat Exchanger	100	0.79	0	1.36
O_2 Extraction Total	769.5	1.555	60.45	1.36
	Radiator Surface Finish (173 m^2 of radiating area)			
	Mass (kg)	**Volume (m^3)**	**Power (kW)**	**Cooling (kW)**
Z-93 Coating	33	0.03	0	0
Post-Processing Total	33	0.03	0	0
	Mass (kg)	**Volume (m^3)**	**Power (kW)**	**Cooling (kW)**
ISRU Process Chain Total	**1098**	**2.83**	**60.85**	**1.36**

[1] The anode and cathode are consumables. The units of the represented values are (kg/y).
[2] The anode and cathode are consumables. The units of the represented values are (m^3/y).

Tab. C–4: ESM input data for concept T2. The ISRU process chain produces 15 t/y of O_2 and 6.7 t/y of Fe-Si alloys to manufacture, within a year, a tubular radiator placed above the lunar surface. The tubular radiator rejects 34.2 kW of heat.

	RASSOR (800 t/y of highlands regolith)			
	Mass (kg)	**Volume (m^3)**	**Power (kW)**	**Cooling (kW)**
Excavation Total	66	1.00	0.32	0
	FeO Enrichment (41.7 t/y of FeO-rich regolith)			
	Mass (kg)	**Volume (m^3)**	**Power (kW)**	**Cooling (kW)**
Particle Size Separator	170	0.17	0	0
Weak-Field Magnetic Separator	3	0.01	0.03	0
Strong-field Magnetic Separator	56	0.06	0.05	0
Beneficiation Total	229	0.24	0.08	0
	Molten Regolith Electrolysis (15 t/y of O_2 and 6.7 t/y of Fe-Si alloys)			
	Mass (kg)	**Volume (m^3)**	**Power (kW)**	**Cooling (kW)**
MRE Reactor	403	0.69	59.63	0
Anode	137.5[1]	0.006[2]	0	0
Cathode	99[1]	0.010[2]	0	0
Oxygen Purification Unit	30	0.005	0.82	0
Heat Exchanger	100	0.79	0	1.36
O_2 Extraction Total	769.5	1.555	60.45	1.36
	Radiator Surface Finish (177 m^2 of radiating area)			
	Mass (kg)	**Volume (m^3)**	**Power (kW)**	**Cooling (kW)**
Z-93 Coating	34	0.03	0	0
Post-Processing Total	34	0.03	0	0
	Mass (kg)	**Volume (m^3)**	**Power (kW)**	**Cooling (kW)**
ISRU Process Chain Total	**1098**	**2.83**	**60.85**	**1.36**

[1] The anode and cathode are consumables. The units of the represented values are (kg/y).
[2] The anode and cathode are consumables. The units of the represented values are (m^3/y).

Tab. C–5: ESM input data for concept S3. The ISRU process chain produces 15 t/y of O_2 and 3.7 t/y of distilled Al to manufacture, within a year, a state-of-the-art radiator placed on the lunar surface. The state-of-the-art radiator rejects 39.6 kW of heat.

	RASSOR (185 t/y of highlands regolith)			
	Mass (kg)	**Volume (m^3)**	**Power (kW)**	**Cooling (kW)**
Excavation Total	66	1.00	0.04	0
	Anorthite Enrichment (33.3 t/y of $CaAl_2Si_2O_8$-rich regolith)			
	Mass (kg)	**Volume (m^3)**	**Power (kW)**	**Cooling (kW)**
Particle Size Separator	4	0.01	0	0
Magnetic Separator	29	0.03	0.72	0
Beneficiation Total	33	0.04	0.72	0
	Molten Salt Electrolysis (15 t/y of O_2)			
	Mass (kg)	**Volume (m^3)**	**Power (kW)**	**Cooling (kW)**
Preheater	298	0.22	8.67	0
MSE Reactor	3417	7.48	66.29	0
Electrolyte	12593[1]	6.27[1]	0	0
Anode	464[2]	0.08[3]	0	0
Oxygen Purification Unit	132	0.80	2.07	1.38
O_2 Extraction Total	16904	14.85	77.03	1.38
	Vacuum Distillation (3.7 t/y of Al)			
	Mass (kg)	**Volume (m^3)**	**Power (kW)**	**Cooling (kW)**
Heater	68	0.02	40.01	0
Distillation Container	121	0.14	0	0
Vacuum Pumps	955	0.53	3.66	0
CHX	316	2.49	0	4.30
Condensation Container	104	0.05	0	0
Metal Processing Total	1564	3.23	43.67	4.30
	Radiator Surface Finish (141 m^2 of radiating area)			
	Mass (kg)	**Volume (m^3)**	**Power (kW)**	**Cooling (kW)**
Z-93 Coating	27	0.02	0	0
Post-Processing Total	27	0.02	0	0
	Mass (kg)	**Volume (m^3)**	**Power (kW)**	**Cooling (kW)**
ISRU Process Chain Total	**18594**	**19.14**	**121.46**	**5.68**

[1] Multiple electrolyte loss rates are evaluated in Chapter 8.
[2] The anode is a consumable. The units of the represented value are (kg/y).
[3] The anode is a consumable. The units of the represented value are (m^3/y).

Tab. C–6: ESM input data for concept T3. The ISRU process chain produces 15 t/y of O_2 and 3.2 t/y of distilled Al to manufacture, within a year, a tubular radiator placed on the lunar surface. The tubular radiator rejects 38.9 kW of heat.

	RASSOR (185 t/y of highlands regolith)			
	Mass (kg)	**Volume (m^3)**	**Power (kW)**	**Cooling (kW)**
Excavation Total	66	1.00	0.04	0
	Anorthite Enrichment (33.3 t/y of $CaAl_2Si_2O_8$-rich regolith)			
	Mass (kg)	**Volume (m^3)**	**Power (kW)**	**Cooling (kW)**
Particle Size Separator	4	0.01	0	0
Magnetic Separator	29	0.03	0.72	0
Beneficiation Total	33	0.04	0.72	0
	Molten Salt Electrolysis (15 t/y of O_2)			
	Mass (kg)	**Volume (m^3)**	**Power (kW)**	**Cooling (kW)**
Preheater	298	0.22	8.67	0
MSE Reactor	3417	7.48	66.29	01
Electrolyte	12593[1]	6.27[1]	0	0
Anode	464[2]	0.08[3]	0	0
Oxygen Purification Unit	132	0.80	2.07	1.38
O_2 Extraction Total	16904	14.85	77.03	1.38
	Vacuum Distillation (3.2 t/y of Al)			
	Mass (kg)	**Volume (m^3)**	**Power (kW)**	**Cooling (kW)**
Heater	58	0.02	34.62	0
Distillation Container	105	0.12	0	0
Vacuum Pumps	826	0.45	3.17	0
CHX	274	2.15	0	3.72
Condensation Container	90	0.04	0	0
Metal Processing Total	1353	2.78	37.79	3.72
	Radiator Surface Finish (128 m^2 of radiating area)			
	Mass (kg)	**Volume (m^3)**	**Power (kW)**	**Cooling (kW)**
Z-93 Coating	24	0.02	0	0
Post-Processing Total	24	0.02	0	0
	Mass (kg)	**Volume (m^3)**	**Power (kW)**	**Cooling (kW)**
ISRU Process Chain Total	**18380**	**18.69**	**115.58**	**5.10**

[1] Multiple electrolyte loss rates are evaluated in Chapter 8.
[2] The anode is a consumable. The units of the represented value are (kg/y).
[3] The anode is a consumable. The units of the represented value are (m^3/y).

Tab. C–7: ESM input data for concept S4. The ISRU process chain produces 15 t/y of O_2 and 19 t/y of highlands metallic mixture to manufacture, within a year, a state-of-the-art radiator placed on the lunar surface. The state-of-the-art radiator rejects 34.2 kW of heat and weights 3.4 t.

	RASSOR (34 t/y of highlands regolith)			
	Mass (kg)	**Volume (m^3)**	**Power (kW)**	**Cooling (kW)**
Excavation Total	66	1.00	0.01	0
	Molten Salt Electrolysis (15 t/y of O_2 and 19 t/y of highlands metallic mixture)			
	Mass (kg)	**Volume (m^3)**	**Power (kW)**	**Cooling (kW)**
Preheater	298	0.22	8.67	0
MSE Reactor	3417	7.48	66.29	0
Electrolyte	12593[1]	6.27[1]	0	0
Anode	464[2]	0.08[3]	0	0
Oxygen Purification Unit	132	0.80	2.07	1.38
O_2 Extraction Total	16904	14.85	77.03	1.38
	Radiator Surface Finish (128 m^2 of radiating area)			
	Mass (kg)	**Volume (m^3)**	**Power (kW)**	**Cooling (kW)**
Z-93 Coating	24	0.02	0	0
Post-Processing Total	24	0.02	0	0
	Mass (kg)	**Volume (m^3)**	**Power (kW)**	**Cooling (kW)**
ISRU Process Chain Total	**16994**	**15.87**	**77.04**	**1.38**

[1] Multiple electrolyte loss rates are evaluated in Chapter 8.
[2] The anode is a consumable. The units of the represented value are (kg/y).
[3] The anode is a consumable. The units of the represented value are (m^3/y).

Tab. C–8: ESM input data for concept T4. The ISRU process chain produces 15 t/y of O_2 and 8.9 t/y of melt-refined Fe to manufacture, within a year, a tubular radiator placed above the lunar surface. The tubular radiator rejects 45 kW of heat.

	RASSOR (60900 t/y of highlands regolith)			
	Mass (kg)	**Volume (m^3)**	**Power (kW)**	**Cooling (kW)**
Excavation Total	5280	80	25.60	0
	Ilmenite Enrichment (197.5 t/y of $FeTiO_3$-rich regolith)			
	Mass (kg)	**Volume (m^3)**	**Power (kW)**	**Cooling (kW)**
Particle Size Separator	1390	1.39	0	0
Weak-Field Magnetic Separator	65	0.10	0.65	0
Strong-field Magnetic Separator	2086	2.06	1.90	0
Beneficiation Total	3541	3.55	2.55	0
	Ilmenite Reduction with H_2 (15 t/y of O_2)			
	Mass (kg)	**Volume (m^3)**	**Power (kW)**	**Cooling (kW)**
H_2 Reduction Reactor	2896	1.83	37.17	0
Cyclone Unit	34	0.01	0	0
Water Purification Unit	705	5.57	0	9.67
SFPW	875	1.22	11.75	0.40
O_2 Extraction Total	4510	8.63	48.92	10.07
	Melting and Refining (8.9 t/y of Fe)			
	Mass (kg)	**Volume (m^3)**	**Power (kW)**	**Cooling (kW)**
Heater	29	0.04	17.18	0
Container	127	0.26	0	0
Metal Processing Total	156	0.30	17.18	0
	Radiator Surface Finish (233 m^2 of radiating area)			
	Mass (kg)	**Volume (m^3)**	**Power (kW)**	**Cooling (kW)**
Z-93 Coating	44	0.03	0	0
Post-Processing Total	44	0.03	0	0
	Mass (kg)	**Volume (m^3)**	**Power (kW)**	**Cooling (kW)**
ISRU Process Chain Total	**13531**	**92.51**	**94.25**	**10.07**